Modeling Seismic Wave Propagation Using Paraxial Extrapolators

Thesis by

Robert Wilson Graves

In Partial Fulfillment of the Requirements
for the Degree of
Doctor of Philosophy

California Institute of Technology
Pasadena, California

1991
(submitted November 16, 1990)

Acknowledgments

I would like to express my appreciation to the students, faculty and staff of the Seismological Laboratory for their help, support and friendship during my stay at Caltech. In addition, I would like to thank the Institute for its financial support, as well as the Amoco Foundation for its generous fellowship.

I have benefited greatly from the interaction with other members in the lab. In particular, I am indebted to Professors Don Helmberger, Dave Harkrider and Rob Clayton for their advice, guidance and tutelage. My work with Don was an invaluable part of my graduate work. In addition, I will always be amazed at Rob's ability to grasp the most complex ideas and explain them in a concise and meaningful way. As a thesis advisor, Rob has always been a patient and enthusiastic supporter of my work.

Over the years, several students and staff members have had a tremendous influence on my work and have also been a source of support and friendship. I will always remember Steve Grand for taking me under his wing my first year at Caltech. Without his help, I would have been lost. Cindy Arvesen was one of the

first people I met when I came to the Seismolab. She was a true friend and I will always have special memories of her. Others who come to mind are Gladys Engen, John Vidale, John Louie, Luciana Astiz, Chris Sanders, Jia-jun Zhang, Hua-wei Zhou, Bruce Worden and Andrea Donnellan. I apologize to anyone I forgot to mention.

The constant support and love of my family has allowed me to pursue my goals and ambitions without losing sight of the fact that there are some things more important in life than work. My father-in-law, Jan Beijer, will forever be a source of inspiration. He accomplished more in his lifetime than most people can only dream about. His untimely passing just two months before the completion of this work was a heartfelt tragedy. My parents deserve a tremendous amount of thanks for always allowing me the freedom to do what I wanted (even when I'm sure they weren't all that pleased with my decisions) and for being supportive and caring, both when I was successful and when I failed. Finally, I would like to thank my wife, Jessica, for her never ending patience, support and love. Without her, I would have accomplished nothing. With her, I can do anything.

Abstract

The development of a paraxial extrapolation system to simulate seismic wave field propagation in complex three-dimensional (3-D) media results in a practical approach to address modeling problems that require large computer memory. The paraxial approach applies to wave propagation problems in which most of the energy is traveling within a restricted angular cone about a principle axis of the problem. To set up the paraxial system, the equations of motion are initially cast as a first-order extrapolation system. Approximating the exact one-way extrapolation operator for this system with a truncated series expansion yields a sequence of paraxial extrapolation operators. Using the second-order operator results in a paraxial system which is accurate for propagation angles out to 60° with respect to the extrapolation axis. The acoustic formulation of this system produces excellent results as compared to a full wave field calculation. Formulating an appropriate system for the elastic case is more difficult due to the coupling between P and S energy. Specifying media variations as small perturbations to a homogeneous reference medium leads to a useful formulation of the paraxial system for the 2-D elastic case.

Using the acoustic system to model path effects for local earthquakes recorded at two southern California stations indicates the strong influence that the 3-D crustal basins of this region have on the propagation of seismic energy. Although the simulation tracks only acoustic waves, the method is capable of modeling effects due to focusing, diffraction and the generation of multiple reflections and refractions. The modeling results show that the 3-D structure of the Los Angeles, San Fernando and San Gabriel basins create strong patterns of focusing and defocusing for propagation paths coming into the stations located at Pasadena (PAS) and the University of Southern California (USC). These simulations compare well with earthquake data recorded at both stations.

Table of Contents

Chapter 1: Modeling Acoustic Waves Using Paraxial Extrapolators

Chapter 2: Wide Angle Wave Field Extrapolation

Chapter 3: Elastic Wave Field Simulation Using Paraxial Extrapolators

Chapter 4: Modeling Path Effects in Three-Dimensional Basins Using a Reciprocal Source Experiment

General Introduction

As we continue to expand our understanding of seismological processes, the need for more complete and robust techniques to model wave propagation phenomena increases. Techniques to simulate fully elastic wave solutions in arbitrary media are presently available; however, the overwhelming computational and storage requirements of these methods for realistic three-dimensional (3-D) problems currently makes the implementation of these techniques impractical. This thesis discusses the development and application of an approximate numerical method to simulate seismic wave propagation in which the computer memory requirements needed to calculate the wave solutions are significantly reduced.

Chapter 1 describes this numerical wave propagation technique as applied to acoustic media. The mathematical formulation of the method is based on a system of one-way paraxial extrapolators. One-way wave field extrapolation techniques are based on the decomposition of the full wave equation into two separate systems, one which tracks energy with positive wavenumbers (forward-scattered energy) and another which tracks energy for negative wavenumbers (backscattered energy).

The paraxial approach is applicable to wave propagation problems in which most of the energy is traveling within a restricted angular cone about a principle axis of the problem. Using this technique, frequency-domain finite-difference solutions accurate for propagation angles out to 60° with respect to the extrapolation axis are readily generated for both two-dimensional (2-D) and 3-D models. Solutions for 3-D problems are computed by applying the 2-D paraxial operators twice, once along the x-axis and once along the y-axis, at each extrapolation step. The azimuthal anisotropy inherent to this splitting technique is essentially eliminated by adding a phase correction operator to the extrapolation system. For heterogeneous models, scattering effects are incorporated by determining transmission and reflection coefficients at structural boundaries within the media. The direct forward-scattered waves are modeled with a single pass of the extrapolation operator in the paraxial direction for each frequency. The first-order backscattered energy can then be modeled by extrapolation (in the opposite direction) of the reflected field determined on the first pass. Higher order scattering can be included by sweeping through the model with more passes.

The chief advantages of the paraxial approach are (1) active storage is reduced by one dimension as compared to solutions which must track both forward-scattered and backscattered waves simultaneously; thus, realistic 3-D problems can fit on today's computers, (2) the decomposition in frequency allows the technique to be implemented on highly parallel machines, (3) attenuation can be modeled as an arbitrary function of frequency, and (4) only a small number of frequencies are needed to produce movie-like time slices.

In Chapter 2, we present a framework for the implementation of more accurate paraxial systems. These higher-order approximate systems are all based on a truncated series expansion of the exact one-way or square-root propagation operator. Following this approach, we derive a fourth-order paraxial system accurate for propagation angles out to nearly 80°. Implementation of the higher-order operators is realized through the sequential application of a series of second-order operators which are derived by factoring the higher-order system. For example, the fourth-order system is solved using a cascade of two second-order systems. The derivation and implementation of this technique is outlined using the 2-D system, although extending the approach to the 3-D case is straightforward. The main drawback with using the high-order formulation is the increased cost of implementation.

The work presented in Chapter 3 deals with the extension of the paraxial formulation to model fully elastic wave propagation phenomena. The derivation of the elastic extrapolation system follows closely to that performed for the acoustic system in Chapter 1. In the formulation of the elastic system, the wave solutions are specified in terms of P-wave and S-wave potentials. The use of potentials is attractive because the propagation aspects of the elastic system are fully described by a set of decoupled scalar wave equations. In the presence of heterogeneous media, coupling between the potentials is accomplished through the use of a scattering matrix. Due to the complexity of the scattering terms, media variations can only be approximated and must be parameterized by using a primary homogeneous part plus a perturbation term to account for any heterogeneity. Following this approach leads to a useable paraxial formulation of the elastic extrapolation system for the 2-D case. Unfortunately, suitable expressions for the discrete implementation of the 3-D system are not currently available.

The final chapter in this thesis discusses the application of the numerical technique presented in Chapter 1 to model path effects for seismic wave propagation within the 3-D crustal basins of southern California. The approach we follow is to use a reciprocal source experiment to analyze data for local earthquakes recorded at two stations in this region. In this experiment, a numerical simulation is performed in which a point source is excited at the given station location and then the wave field is propagated and recorded throughout a 3-D grid of points. Although the numerical technique tracks only acoustic waves, the method is capable of handling arbitrary media variations; thus, effects due to focusing, diffraction and the generation of multiple reflections and refractions are modeled quite well. The principle of reciprocity is then used to reverse source and receiver locations. Using this concept, the wave field observed at a particular grid point is the same as would be observed at the station if the source were located at that grid point. This allows us to model all possible source locations within a given 3-D volume using only one simulation. A numerical check of the reciprocity concept verifies the validity of using this approach. For the numerical simulations, the station locations were chosen at Pasadena (PAS) and the University of Southern California (USC). These particular sites are well suited for this experiment because they both operate high dynamic range, broadband digital recording instruments and each station is situated in a different geologic setting. The modeling results show that the 3-D structure of the Los Angeles, San Fernando and San Gabriel basins create strong patterns of focusing and defocusing for paths coming into these stations. By comparing these calculations with earthquake data recorded at both stations, we can begin to investigate the nature in which these propagation effects contribute to observed patterns of strong ground motions.

Chapter 1

Modeling Acoustic Waves Using Paraxial Extrapolators

1.1 Introduction

Several numerical techniques have been developed for simulating wave motions in complex media. The most general of these are the finite-difference (FD) method (Kelly et al., 1976), the finite-element (FE) method (Marfurt, 1984), and the pseudo-spectral (PS) method (Koslof and Baysal, 1982). In their heterogeneous formulations, these techniques are capable of complete wave solutions in arbitrary models. The chief shortcoming of these numerical simulations is that for 3-D and large 2-D problems their computational requirements overwhelm the capabilities of most computer hardware currently available. The use of supercomputers (Reshef et al., 1988a, b) or massively parallel computers (Fricke, 1988) may provide a way around this problem; however, even with this technology, the implementation of these methods is still restricted by the availability of accessible computer memory.

To address this problem, we present an approximate numerical technique that is based on one-way paraxial extrapolators. The use of paraxial extrapolators as a means of seismic wave propagation was first introduced by Claerbout (1970). Since then this technique has been extensively developed for the migration of seismic reflection data (e.g., Claerbout, 1985a). Other applications of the extrapolators include their adaptation for use as absorbing boundary conditions in FD simulations (Clayton and Engquist, 1977). The paraxial operators correctly model waves traveling within an angular cone centered about a particular axis of the problem. For example, surface waves can be modeled with horizontal extrapolators, while precritical reflections can be modeled with vertical extrapolation. These operators are usually referred to by the extent of their angular accuracy. The most commonly known paraxial systems are the 15° and 45° approximations. However, an operator which is accurate to 60° can be obtained simply by modifying the coefficients in the 45° approximation.

To set up the paraxial system, we first arrange the equations of motion into a first-order extrapolation system. In doing this, we effectively reduce the computer memory requirements needed to calculate the solution by one spatial dimension compared to the complete methods. This enables us to generate solutions to 3-D problems simply by extrapolating the wave field through the model on a 2-D plane with the end result that storage requirements are rarely a limiting factor when using this technique on large 2-D or 3-D problems.

In the next section, we derive the general form of the extrapolation system for 3-D problems. This is followed by a discussion of the paraxial approximation and the implementation of the resulting numerical system, including the incorporation of sources and scattering effects, for both 2-D and 3-D models. The formulation is developed in the temporal frequency domain; some advantages of using this domain are also discussed. Finally, we present some examples of the application of this technique to various seismic problems.

1.2 The 3-D extrapolation system

1.2.1 Equations of motion

In this section the acoustic (scalar) extrapolators are derived for a general 3-D medium. The extrapolators are based on the coupled first-order equations

$$\begin{aligned} \rho\omega^2\mathbf{u} &= \nabla P + \mathbf{f}_{F} \\ K^{-1}P &= -\nabla\cdot\mathbf{u} + f_{V} \end{aligned} \qquad (1.1)$$

where $P(x,y,z,\omega)$ is the pressure, $\mathbf{u} = (u,v,w)^T$ is the displacement, $\rho(x,y,z)$ is the density, $K(x,y,z)$ is the bulk modulus (compressibility), and ω is the frequency. The terms $\mathbf{f}_{F} = (f_x, f_y, f_z)^T$ and f_{V} are the force and volume injection sources of the system respectively. These equations can be recast into the first-order extrapolation system

$$\partial_z \begin{pmatrix} P \\ w \end{pmatrix} = \mathbf{A}\begin{pmatrix} P \\ w \end{pmatrix} + \mathbf{f} \qquad (1.2)$$

where

$$\mathbf{f} = \left(-f_z, f_{V} - \frac{1}{\omega^2}\left(\partial_x\frac{1}{\rho}f_x + \partial_y\frac{1}{\rho}f_y\right)\right)^T \qquad (1.3)$$

is the source vector,and $\mathbf{A}$ is the matrix

$$\mathbf{A} = \begin{pmatrix} 0 & \rho\omega^2 \\ -\frac{1}{\rho\omega^2}\alpha^2 & 0 \end{pmatrix} \qquad (1.4)$$

with α given by the pseudodifferential operator

$$\alpha = \left(\frac{\omega^2}{v^2} + \rho\,\partial_x \frac{1}{\rho} \partial_x + \rho\,\partial_y \frac{1}{\rho} \partial_y \right)^{1/2} \tag{1.5}$$

where $v^2 = K/\rho$. The symbols ∂_x, ∂_y and ∂_z are used as shorthand representations of the differential operators $\partial/\partial x$, $\partial/\partial y$ and $\partial/\partial z$.

Using equation (1.2) to extrapolate wave fields through heterogeneous media presents a problem because this system is complete and propagates both forward and backscattered wave fields simultaneously. Thus, in order to start the extrapolation process, we need to specify the entire wave field (forward and backscattered energy) for all time along one boundary of the model. This is problematic in modeling exercises, since we generally have a priori information only about the source and not about energy which has propagated through the region to be modeled. For this reason, we need to find an alternative formulation of the extrapolation system.

Our approach is to start from equation (1.2) and form a new set of decoupled paraxial extrapolators. The advantage of this method is that the propagation aspects of the new system are well understood and all that remains is to incorporate the effects of scattering.

1.2.2 Decoupling the first-order system

To form a set of paraxial extrapolators for equation (1.2), the **A** matrix is decomposed into its eigenvalue and eigenvector representation. That is

$$\mathbf{A} = \mathbf{E}\boldsymbol{\Lambda}\mathbf{E}^{-1} \tag{1.6}$$

where

$$\boldsymbol{\Lambda} = \begin{pmatrix} i\alpha & 0 \\ 0 & -i\alpha \end{pmatrix}, \tag{1.7a}$$

$$\mathbf{E} = \begin{pmatrix} 1 & 1 \\ \dfrac{i}{\rho\omega^2}\alpha & \dfrac{-i}{\rho\omega^2}\alpha \end{pmatrix} \tag{1.7b}$$

and

$$\mathbf{E}^{-1} = \frac{1}{2}\begin{pmatrix} 1 & \dfrac{-i}{\alpha}\rho\omega^2 \\ 1 & \dfrac{i}{\alpha}\rho\omega^2 \end{pmatrix}. \tag{1.7c}$$

We now define a new solution vector

$$\begin{pmatrix} P_f \\ P_b \end{pmatrix} = \mathbf{E}^{-1}\begin{pmatrix} P \\ w \end{pmatrix} \tag{1.8}$$

where $P = P_f + P_b$. The subscripts f and b refer to the forward-scattered and backscattered portions of the pressure field respectively. By convention, we have chosen the forward-scattered pressure field P_f to represent energy which is propagating in the positive z direction. Using equations (1.6) and (1.8) in equation (1.2) transforms the extrapolation system into

$$\partial_z \mathbf{E}\begin{pmatrix} P_f \\ P_b \end{pmatrix} = \mathbf{E}\boldsymbol{\Lambda}\begin{pmatrix} P_f \\ P_b \end{pmatrix} + \mathbf{f}.$$

Differentiating through the left side, premultiplying by $\mathbf{E}^{-1}$, and defining

$$\mathbf{f}_E = \mathbf{E}^{-1}\mathbf{f} \quad \text{and} \quad \mathbf{S} = -\mathbf{E}^{-1}\mathbf{E}_z \tag{1.9}$$

where $\mathbf{E}_z = \partial\mathbf{E}/\partial z$, we have

$$\partial_z \begin{pmatrix} P_f \\ P_b \end{pmatrix} = \boldsymbol{\Lambda}\begin{pmatrix} P_f \\ P_b \end{pmatrix} + \mathbf{S}\begin{pmatrix} P_f \\ P_b \end{pmatrix} + \mathbf{f}_E. \tag{1.10}$$

The propagation aspects of the forward and backscattered waves of this system are now decoupled. They remained coupled through the scattering matrix **S**, which is only nonzero at points where the medium changes. We will treat the scattering as if it were a pseudo source. First, however, approximations for the **Λ** operator are presented.

1.3 The propagation matrix

If we neglect for a moment the real sources of (1.10) and allow the media to vary only as a function of x and y, but not of z ($\mathbf{S} = 0$), then the problem reduces to solving the decoupled system

$$\partial_z \begin{pmatrix} P_f \\ P_b \end{pmatrix} = \begin{pmatrix} i\alpha & 0 \\ 0 & -i\alpha \end{pmatrix} \begin{pmatrix} P_f \\ P_b \end{pmatrix} \tag{1.11}$$

where $v = v(x, y)$ and $\rho = \rho(x, y)$. The operator α, while symbolically represented by the pseudodifferential operator of equation (1.5), needs to be placed in a rational form for actual use. In order to accomplish this, let us consider only the forward-scattered portion of equation (1.11)

$$\partial_z P_f = i\alpha P_f. \tag{1.12}$$

Factoring out the wave field, P_f, we obtain the following relation:

$$\partial_z = i\alpha. \tag{1.13}$$

Substituting the expression for α from equation (1.5) and writing this equation symbolically, we have

$$D_z = i\big[1 + (D_x^2 + D_y^2)\big]^{1/2}, \tag{1.14}$$

where

$$D_x^2 = \frac{v^2}{\omega^2}\rho\,\partial_x\frac{1}{\rho}\partial_x,$$
$$D_y^2 = \frac{v^2}{\omega^2}\rho\,\partial_y\frac{1}{\rho}\partial_y$$

and

$$D_z = \frac{v}{\omega}\partial_z.$$

Equation (1.14) represents the exact one-way propagation operator.

Treating the symbols D_x^2 and D_y^2 as numerical representations of the corresponding differential operators, we expand equation (1.14) with a continued-fraction representation. and obtain the general second-order approximation

$$D_z \approx i\big[1 + B(D_x^2 + D_y^2)\big]^{-1}\big[1 + A(D_x^2 + D_y^2)\big] \tag{1.15}$$

(Claerbout, 1985a, p. 83). Here, A and B are constant coefficients which can be chosen so as to maximize the accuracy of equation (1.15) over a given range of propagation angles (e.g., A=1/2, B=0 is the 15° approximation, A=3/4, B=1/4 is the 45° approximation and A=0.82, B=0.32 is the 60° approximation) (Lee and Suh, 1985; Halpern and Trefethen, 1988).

Expressions like equation (1.15) are usually derived by assuming a homogeneous medium and performing the expansion in the wavenumber-frequency domain. For our purposes; however, we must take care to ensure that equation (1.15) provides a reasonable approximation to the exact operator for laterally varying media as well. Clearly, this expression does reduce to the proper formulation for the homogeneous case; furthermore, since it is a local operator, the expression is also appropriate within locally homogeneous regions of heterogeneous models. The main question remaining then is how well this operator matches the correct reflection and transmission coefficients as the wave field is propagated across a lateral boundary between different types of media. Answering this question directly is difficult because the exact operator does not have a simple analytic representation. However, we can obtain an idea as to the order of accuracy by comparing the square of the exact operator with the square of the approximate operator. Here, the square of an operator is defined as the operator applied to itself.

From equation (1.14), we have for the exact operator (recalling that v is not a function of z)

$$D_z^2 = \frac{v^2}{\omega^2}\partial_{zz} = -\left[1 + (D_x^2 + D_y^2)\right]. \tag{1.16}$$

Now using the expansion

$$\left[1 + B(D_x^2 + D_y^2)\right]^{-1} = \left[1 - B(D_x^2 + D_y^2) + B^2(D_x^2 + D_y^2)^2 - \cdots\right],$$

we obtain for the approximate operator

$$D_z^2 \approx -\left\{1 + 2(A - B)(D_x^2 + D_y^2) + O\left[(D_x^2 + D_y^2)^2\right]\right\}. \tag{1.17}$$

As long as $A - B = 1/2$, the approximation is accurate to $O\left[(D_x^2 + D_y^2)^2\right]$. In most cases, the squared term is quite small for propagation angles within the range of validity of the operator as determined by the coefficients A and B. This will be demonstrated later by example.

We now substitute relation (1.15) into equation (1.12) to obtain the paraxial wave equation

$$\frac{v}{\omega}\partial_z P_f = i\left[1 + B(D_x^2 + D_y^2)\right]^{-1}\left[1 + A(D_x^2 + D_y^2)\right]P_f. \tag{1.18}$$

The corresponding Crank-Nicolson difference equation is given by

$$\zeta^{-1}(P_f^{n+1} - P_f^n) = i\left[1 + B(D_x^2 + D_y^2)\right]^{-1}\left[1 + A(D_x^2 + D_y^2)\right](P_f^{n+1} + P_f^n) \tag{1.19}$$

where $\zeta = \omega\Delta z/(2v)$ and $P_f^n = P_f(x, y, z = z_n, \omega)$. We want to solve this equation for the wave field P_f^{n+1}; however, since the operators in equation (1.19) do not commute with one another, we must take care to preserve the correct operator ordering. Performing the appropriate algebra, we obtain

$$\begin{aligned}\left\{1 + \frac{1}{v}B(D_x^2 + D_y^2)v - i\zeta[1 + A(D_x^2 + D_y^2)]\right\}P_f^{n+1}&\\ = \left\{1 + \frac{1}{v}B(D_x^2 + D_y^2)v + i\zeta[1 + A(D_x^2 + D_y^2)]\right\}P_f^n&\end{aligned} \tag{1.20}$$

Unfortunately, using equation (1.20) directly to solve for P_f^{n+1} will present a problem because of the $(D_x^2 + D_y^2)$ term. Discretizing the x- and y-axes and approximating the differential operators with difference operators results in a system of N^2 simultaneous equations, where N is the number of grid points in either the x or y directions. Even with the most efficient solution algorithms, processing this system of equations requires a computational effort proportional to N^3. In addition, these operations must be performed for each frequency component at each depth step, a procedure which is far too costly for most practical applications.

The traditional method to circumvent this problem is to approximate equation (1.20) with a system in which the operators that depend on D_x^2 have been split from those which depend on D_y^2. We follow a similar approach which is outlined below.

First let us rewrite equation (1.20) as

$$(1-i\zeta)\big[1+\gamma_-(D_x^2+D_y^2)v+i\delta_-(D_x^2+D_y^2)\big]P_f^{n+1}$$
$$=(1+i\zeta)\big[1+\gamma_+(D_x^2+D_y^2)v+i\delta_+(D_x^2+D_y^2)\big]P_f^n \qquad (1.21)$$

where

$$\gamma_\pm=(1\pm i\zeta)^{-1}\frac{1}{v}B$$

and

$$\delta_\pm=\pm(1\pm i\zeta)^{-1}\zeta A.$$

Now we use the following approximation

$$\big[1+\gamma(D_x^2+D_y^2)v+i\delta(D_x^2+D_y^2)\big]$$
$$\approx\big[1+\gamma(D_x^2+D_y^2)v+i\delta(D_x^2+D_y^2)\big]$$
$$+(\gamma D_x^2v+i\delta D_x^2)(\gamma D_y^2v+i\delta D_y^2)$$
$$=[1+\gamma D_x^2v+i\delta D_x^2][1+\gamma D_y^2v+i\delta D_y^2]. \qquad (1.22)$$

Note that the error term, $(\gamma D_x^2v+i\delta D_x^2)(\gamma D_y^2v+i\delta D_y^2)$, is nearly zero (zero in the homogeneous case) for energy propagating along either the x or y axis and is a maximum for energy propagating along a 45° rotation of these axes. Putting relation (1.22) into equation (1.21), we have the following system

$$(1-i\zeta)[1+\gamma_- D_x^2 v + i\delta_- D_x^2][1+\gamma_- D_y^2 v + i\delta_- D_y^2]P_f^{n+1}$$
$$= (1+i\zeta)[1+\gamma_+ D_x^2 v + i\delta_+ D_x^2][1+\gamma_+ D_y^2 v + i\delta_+ D_y^2]P_f^n,$$

or, rewriting, we obtain

$$\begin{aligned}\Big[(1-i\zeta)+\frac{1}{v}BD_x^2 v - i\zeta A D_x^2\Big](1-i\zeta)^{-1}&\\ \times\Big[(1-i\zeta)+\frac{1}{v}BD_y^2 v - i\zeta A D_y^2\Big]P_f^{n+1}&\\ =\Big[(1+i\zeta)+\frac{1}{v}BD_x^2 v + i\zeta A D_x^2\Big](1+i\zeta)^{-1}&\\ \times\Big[(1+i\zeta)+\frac{1}{v}BD_y^2 v + i\zeta A D_y^2\Big]P_f^{n}&\qquad(1.23)\end{aligned}$$

In the remainder of this discussion, the system described by equation (1.20) is referred to as the unsplit operator system and that given by equation (1.23) as the split operator system.

The advantage of using the split operator system is that the computational effort needed to solve these equations is now proportional to N^2. The solution of this system is obtained by using the following recursion

$$A_0 b_1 = b_0, \qquad (1.24a)$$

$$b_2 = A_1 b_1 \qquad (1.24b)$$

and

$$A_2 P_f^{n+1} = b_2, \qquad (1.24c)$$

where

$$b_0 = \left[(1+i\zeta)+\frac{1}{v}BD_x^2v+i\zeta AD_x^2\right](1+i\zeta)^{-1}\left[(1+i\zeta)+\frac{1}{v}BD_y^2v+i\zeta AD_y^2\right]P_f^n,$$

$$A_0 = \left[(1-i\zeta)+\frac{1}{v}BD_x^2v-i\zeta AD_x^2\right],$$

$$A_1 = (1-i\zeta)$$

and

$$A_2 = \left[(1-i\zeta)+\frac{1}{v}BD_y^2v-i\zeta AD_y^2\right].$$

Discretizing the x- and y-axes and using second-order finite-difference approximations for D_x^2 and D_y^2 reduces equations (1.24a) and (1.24c) into tridiagonal matrix systems for which solutions are easily generated (e.g., Claerbout, 1985a, p. 98).

Using these equations, the computational sequence to extrapolate the wave field one step in z would proceed as follows: (1) calculation of b_0 for all points in the model plane $(x_i, y_j, z = z_n)$ $[i = 1, ..., nx; j = 1, ..., ny]$, (2) application of equation (1.24a) along strips of x for each point y_j, (3) application of equation (1.24b) for all points (x_i, y_j) and (4) application of equation (1.24c) along strips of y for each point x_i of the model plane.

It should also be noted that the implementation of the above steps is easily performed in a parallel or vector processing environment. This is trivial for steps (1) and (3). For step (2), note that the application of equation (1.24a) is independent of y in the sense that the solution along the x-strip at y_j does not depend on the solution at y_{j-1}, y_{j+1} or at any other value of y. Likewise, in step (4) the application of equation (1.24c) is independent of the variable x. Thus, equation (1.24a) can be solved for all points y_j in parallel and equation (1.24c) solved for all points x_i in parallel.

1.3.1 Accuracy of the split operator system

The problem with the split operator system [equation (1.23)], as mentioned earlier, is that its accuracy varies azimuthally. One way to analyze this variation is to examine the phase difference between the unsplit operator system and the split operator system as a function of azimuth. In order to perform this analysis, we must restrict ourselves to a homogeneous medium and then transform these equations into the wavenumber-frequency domain. This details of this process are presented in Appendix A. From equations (A.2) and (A.4) these two systems can now be written as

$$\hat{P}_f^{n+1} = \exp(i\phi)\exp(i\phi_0)\hat{P}_f^n \qquad \text{(unsplit system)} \tag{1.25a}$$

and

$$\hat{P}_f^{n+1} = \exp(i\phi)\exp(i\phi_x)\exp(i\phi_y)\hat{P}_f^n \qquad \text{(split system);} \tag{1.25b}$$

where

$$\begin{aligned}
\phi &= 2\tan^{-1}(\zeta), \\
\phi_0 &= 2\tan^{-1}(a_0), \qquad a_0 = \delta({K_x}^2 + {K_y}^2)/[1 + \gamma({K_x}^2 + {K_y}^2)], \\
\phi_x &= 2\tan^{-1}(a_1), \qquad a_1 = \delta {K_x}^2/(1 + \gamma {K_x}^2)
\end{aligned}$$

and

$$\phi_y = 2\tan^{-1}(a_2), \qquad a_2 = \delta {K_y}^2/(1+\gamma {K_y}^2).$$

with $\gamma + i\delta = -(B+i\zeta A)/(1+i\zeta)$, $\hat{P}_f^n = \hat{P}_f(k_x, k_y, z = z_n, \omega)$ and the wavenumbers are represented as $\frac{v^2}{\omega^2}k_x^2 = {K_x}^2$ and $\frac{v^2}{\omega^2}k_y^2 = {K_y}^2$.

Comparing equations (1.25), we write the phase difference between the two systems as

$$\phi_d = \phi_0 - \phi_x - \phi_y. \tag{1.26}$$

In Figure 1.1, curve A plots the phase difference between the unsplit operator [equation (1.25a)] and the split operator [equation (1.25b)] as a function of propagation angle for an azimuth of 45° ($K_x = K_y$). Note that there is a significant phase difference between the two for propagation angles beyond 30°. For this comparison we have chosen $A = 0.82$ and $B = 0.32$.

1.3.2 The phase correction filter

If we can derive a filter with a phase operator given by equation (1.26) and apply it to the system (1.23) at each extrapolation step, we can effectively remove the azimuthal anisotropy of the extrapolation system. In order to do this, let us define

$$\phi_d = tan^{-1}(a_3), \qquad a_3 = \frac{\mathrm{Im}(F)}{\mathrm{Re}(F)} \tag{1.27}$$

where F is the filter that we desire. Now approximating $\tan^{-1}(a_i) \approx a_i$ in equations (1.25) and (1.27) and then using these in equation (1.26), we can write

$$a_3 \approx -2\gamma\delta {K_x}^2 {K_y}^2 \left(\frac{[2+\gamma({K_x}^2+{K_y}^2)]}{(1+\gamma {K_x}^2)(1+\gamma {K_y}^2)[1+\gamma({K_x}^2+{K_y}^2)]} \right) \tag{1.28}$$

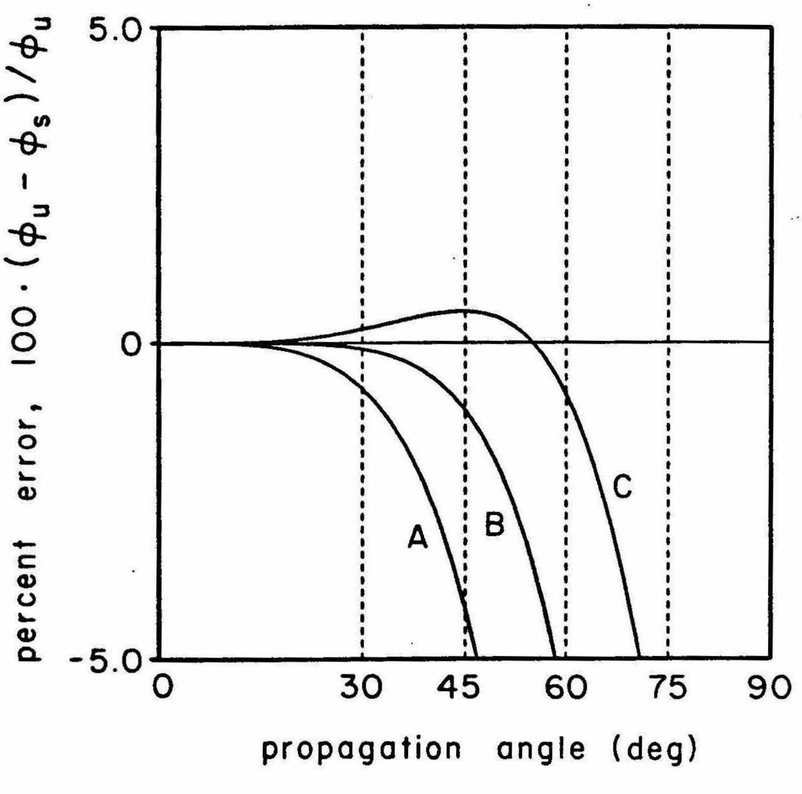

Figure 1.1. Phase difference between the unsplit (ϕ_u) and the split (ϕ_s) extrapolation systems at an azimuth of 45°. We have set $\zeta = 0.125$ for these calculations, although the results are fairly insensitive to variations in ω, Δz and v. Curve A shows the phase difference calculated with no correction term. Curve B shows the phase difference calculated with application of first-order correction term [equation (1.29)]. Curve C shows the phase difference calculated with correction term and $\epsilon_0 = 1.5$ [equation (1.30)].

This approximation is appropriate for $({K_x}^2 + {K_y}^2) < 1$ since a_0, a_1 and $a_2 \sim \zeta$ in this region and $\zeta << 1$. The first-order approximation to this gives us

$$F = 1 - i4\gamma\delta {K_x}^2 {K_y}^2. \tag{1.29}$$

Applying the phase correction filter of equation (1.29) to the split operator system does a good job in reducing the anisotropy of the extrapolation operator as demonstrated in Figure 1.1, curve B. This plot is the same as curve A, except that the phase of the split operator has been modified by the phase correction filter. Even with the first order approximation, the phase difference is less than one percent for propagation angles out to 45°.

Taking higher order terms in a_3 gives a better match to the phase of the original operator; however, taking higher order terms also increases the cost to implement the system. As it turns out, there is a much simpler way to achieve better accuracy. By redefining F as

$$F = 1 - i4\epsilon_0\gamma\delta {K_x}^2 {K_y}^2 \tag{1.30}$$

where ϵ_0 is an adjustable parameter, we can extend the accuracy of this filter to cover a wider range of propagation angles. This increased accuracy is shown in Figure 1.1, curve C. Here we have the same phase comparison as before except that we have used the filter given by equation (1.30) with $\epsilon_0 = 1.5$. In this case the phase difference is less than one percent for propagation angles out to and beyond 60°.

1.3.3 Stability considerations

Using the phase correction filter as defined by equation (1.30) will, in general, result in an unstable extrapolation system. The reason for this is that the magnitude of this filter is greater than unity for all nonzero values of ${K_x}^2$ and ${K_y}^2$. To compensate for this effect a damping function must be added to the filter. We have found that a filter of the form

$$F = D_1\left[1 - i4\epsilon_0 D_2 \gamma\delta {K_x}^2 {K_y}^2\right] \qquad \begin{aligned} D_1 &= (1+\epsilon_1 K_x^4)^{-1}(1+\epsilon_1 K_y^4)^{-1} \\ D_2 &= (1+\epsilon_2 K_x^4)^{-1}(1+\epsilon_2 K_y^4)^{-1} \end{aligned} \tag{1.31}$$

works very well. This filter is stable for

$$\epsilon_2 \geq \frac{1}{\epsilon_1}\epsilon_0^2\gamma^2\delta^2 - \frac{3}{8}\epsilon_1. \tag{1.32}$$

The use of two damping terms may seem like an unnecessary complication; however, it allows us to choose the values of ϵ_1 and ϵ_2 such that the magnitude of the operator is near unity for all $({K_x}^2 + {K_y}^2) \leq 1$. Using equation (1.31) with $\epsilon_1 \approx 0.001$ is most effective. Larger values of ϵ_1 provide too much damping and will deteriorate the signal in the region $({K_x}^2 + {K_y}^2) \leq 1$. Smaller values of ϵ_1 require too large a value of ϵ_2 to be used and thus significantly decrease the effectiveness of the filter. Finally, it should be noted that the addition of the damping terms have no effect on the phase of the filter.

As shown in Appendix B, we can implement equation (1.31) in the spatial domain as a cascade of tridiagonal matrix systems. We will symbolically represent this operation as

$$Q_f^{n+1} = \mathcal{F} P_f^{n+1} \tag{1.33}$$

where $\mathcal{F}$ is the spatial domain operator corresponding to equation (1.31), P_f^{n+1} is the extrapolated wave field calculated from equations (1.24) and Q_f^{n+1} is the phase corrected wave field.

For laterally varying media, we can simply let $v \to v(x, y)$ in the filter $\mathcal{F}$. Although this substitution neglects the issue of operator ordering, it is still appropriate since the phase correction filter is only a first-order correction to the extrapolation system. Further modifications to the filter itself will, in general, result in a much more complicated system to implement.

Unfortunately, it is difficult to analyze the stability of the filter when $v = v(x, y)$ because in this situation there is no straightforward analytic expression for $\mathcal{F}$ in the wavenumber-frequency domain. Our experience has shown us that if the lateral variations in the velocity field are large (i.e., greater than ten percent), then it may be necessary to smooth the velocity field prior to the application of the filter in order to ensure stable extrapolation. Smoothing the velocity field reduces the magnitude of the internal reflection coefficient within the filter $\mathcal{F}$ at points where the velocity field changes, particularly for the larger values of K_x and K_y where the filter is most prone to become unstable. The choice of an appropriate smoothing function is somewhat arbitrary; however, the function should be sufficiently sharp so as to not significantly alter the phase of the filter $\mathcal{F}$. We have found that simply averaging the velocity field over adjacent grid points works quite well even for regions with substantial velocity variations (e.g., velocity contrasts on the order of 3:1).

Applying the phase correction operator to the extrapolation process produces excellent results. Here, we compare calculations performed with and without the phase correction operator. In both cases, the output is viewed as a time-slice on an image plane located 40 grid points away from the source point (Figure 1.2). The geometry of the model is such that at this time the energy arriving in this plane is propagating at an angle of about 60° with respect to the extrapolation direction. The results are shown in Figure 1.3. The first calculation (Figure 1.3, left panel) was computed without the phase correction operator and exhibits a characteristic diamond shape indicative of the azimuthal variation in accuracy which is inherent to the split operator system. The second calculation (Figure 1.3, right panel) included the application of the phase correction operator to the wave field at each step in the extrapolation process. Note that the wave field in this panel is essentially circular and shows no apparent azimuthal variations.

1.3.4 Dipfiltering

The extrapolation operators derived from the continued fraction expansion are designed to match the exact dispersion relation best for $({K_x}^2+{K_y}^2) < 1$. However, in the evanescent region of k_z [i.e., $({K_x}^2+{K_y}^2) > 1$] these operators do a very poor job of matching the exact operator. In fact, for both 2-D and 3-D calculations, the operators can produce significant artifacts from energy propagating in this region. This is illustrated in Figure 1.4 which shows the numerical point response of the extrapolation system presented earlier. In this example the output is viewed as a

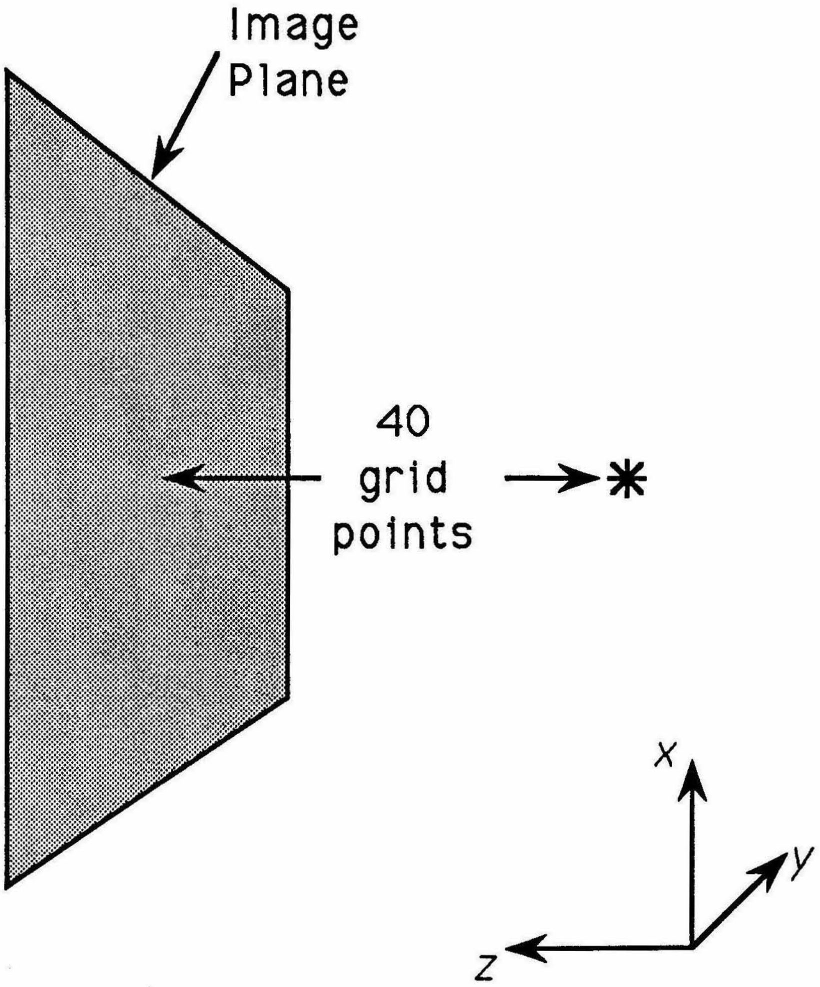

Figure 1.2. Model geometry for phase correction filter comparison.

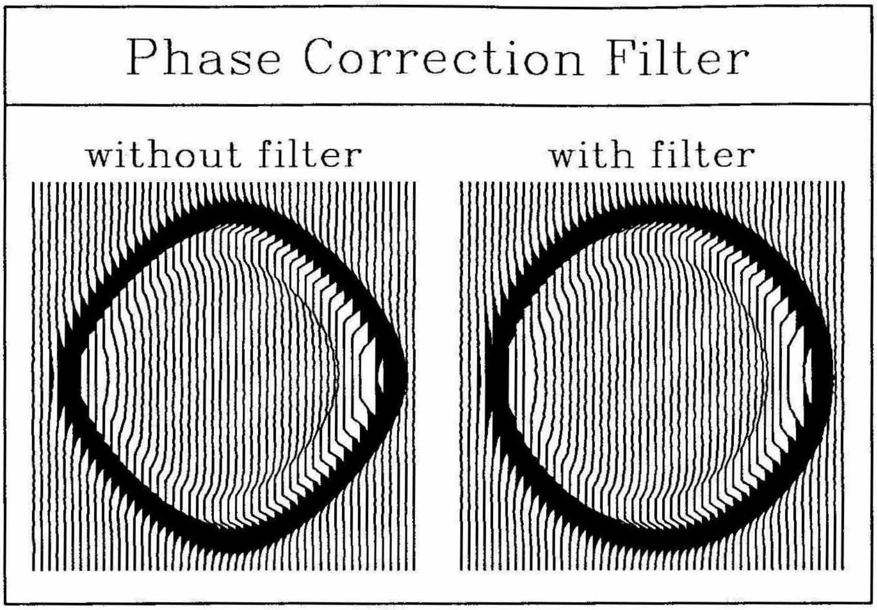

Figure 1.3. Phase correction filter comparison. The left panel shows the 3-D split-operator extrapolation result calculated without application of the phase correction filter. The azimuthal variation in accuracy is characteristic of the split-operator system. In the right panel, we have performed the same calculation as before except the phase correction operator has been applied to the propagation system at each extrapolation step. Notice the nearly circular wavefront resulting from the filtering process.

time-slice in the xz plane at $y = 0$ with the source located at the origin. No filtering has been applied to this calculation. The proper response for this projection is a quarter-circle and it is evident from Figure 1.4 that the paraxial solution does well for propagation angles out to about 60°. Beyond this point, the solution becomes less accurate with increasing dip and the wavefront actually curls back under itself producing a secondary arrival. This secondary cusp-like arrival is an artifact arising from energy propagating in the region $({K_x}^2 + {K_y}^2) > 1$. Although this secondary wavefront has a slower group velocity than the main wavefront, it can produce arrivals which interfere with energy of interest and result in a solution which is both confusing and difficult to interpret. In order to prevent this situation from occurring, the energy in this region needs to be suppressed.

Fortunately, this can be accomplished using the same filtering technique described in the previous section. Each of the damping terms in the phase correction filter [equation (1.31)] also acts as a dipfilter which strongly suppresses energy in the region $({K_x}^2 + {K_y}^2) > 1$. This can be seen by examining the general form of the damping terms given by

$$\hat{Q}_f = D\hat{P}_f \qquad D = (1 + \epsilon K_x^{2n})^{-1}(1 + \epsilon K_y^{2n})^{-1} \qquad n = 1, 2, \cdots \tag{1.34}$$

with $\epsilon << 1$. In the region $|K_x| << 1$ or $|K_y| << 1$, then $D \rightarrow 1$ (all pass) and in the region $|K_x| >> 1$ or $|K_y| >> 1$, then $D \rightarrow 0$ (reject). The parameter n controls the sharpness of the cutoff between the pass and reject zones.

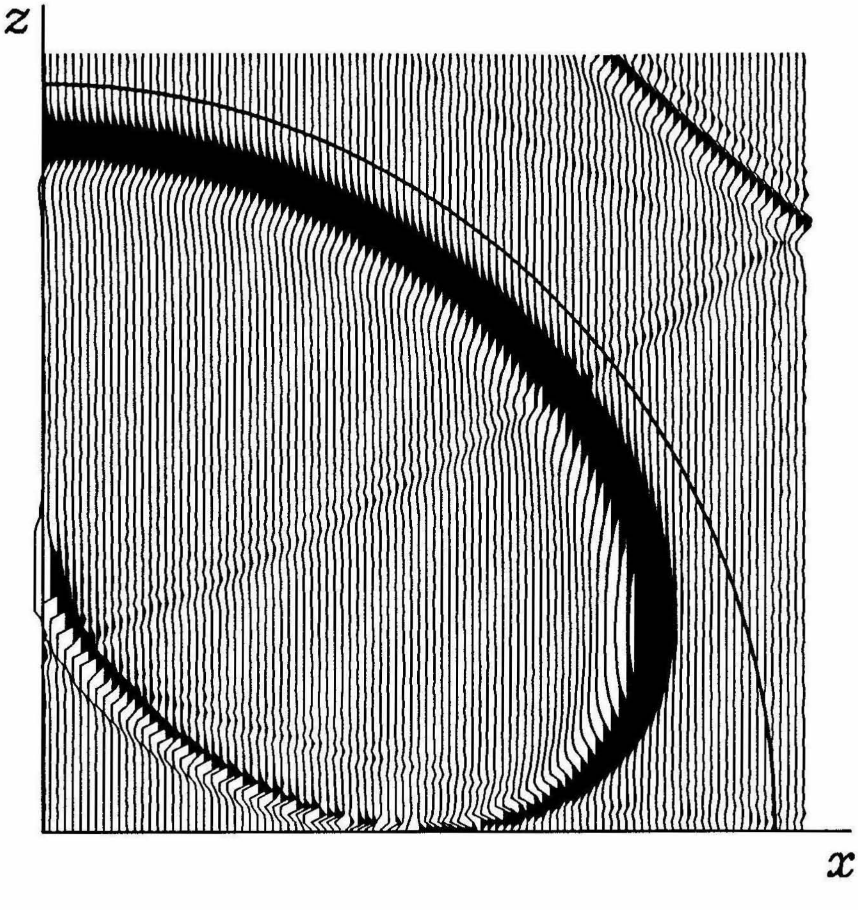

Figure 1.4. Time-slice in the xz plane showing the point response of the 60° paraxial system. Proper response for this projection is a quarter-circle as denoted by the heavy curve. The secondary cusp-like waveform near the origin is due to energy propagating in the region $({K_x}^2 + {K_y}^2) > 1$.

To demonstrate the effectiveness of the dipfilter, we have recalculated the point response applying equation (1.34) with $\epsilon_1 = 0.001$ and $n = 2$ at each depth step. The result is shown in Figure 1.5. Note that a large portion of the energy in the evanescent zone has been eliminated, while energy in the region $({K_x}^2 + {K_y}^2) < 1$ has not been visibly affected.

1.3.5 Boundary conditions

We consider three types of boundary conditions to be applied along the edges of the model grid. These conditions are (1) zero-value (to represent a free-surface), (2) zero-slope (to represent a plane of symmetry) and (3) absorbing (to represent an infinite medium). Since the paraxial system is first-order along the z-axis (extrapolation direction), any of the above conditions can be specified exactly for boundaries perpendicular to this axis. For the x and y dimensions, the boundary conditions must be applied when solving the tridiagonal matrix systems at each extrapolation step. In this case, exact representations of conditions (1) and (2) are readily prescribed and a very good approximate absorbing condition is given by the B3 formulation of Clayton and Engquist (1980).

1.4 The scattering matrix

The scattering matrix forms the coupling between the forward-scattered and backscattered waves in the presence of heterogeneous media. Incorporating these effects within the extrapolation system [equation (1.10)], we have the following

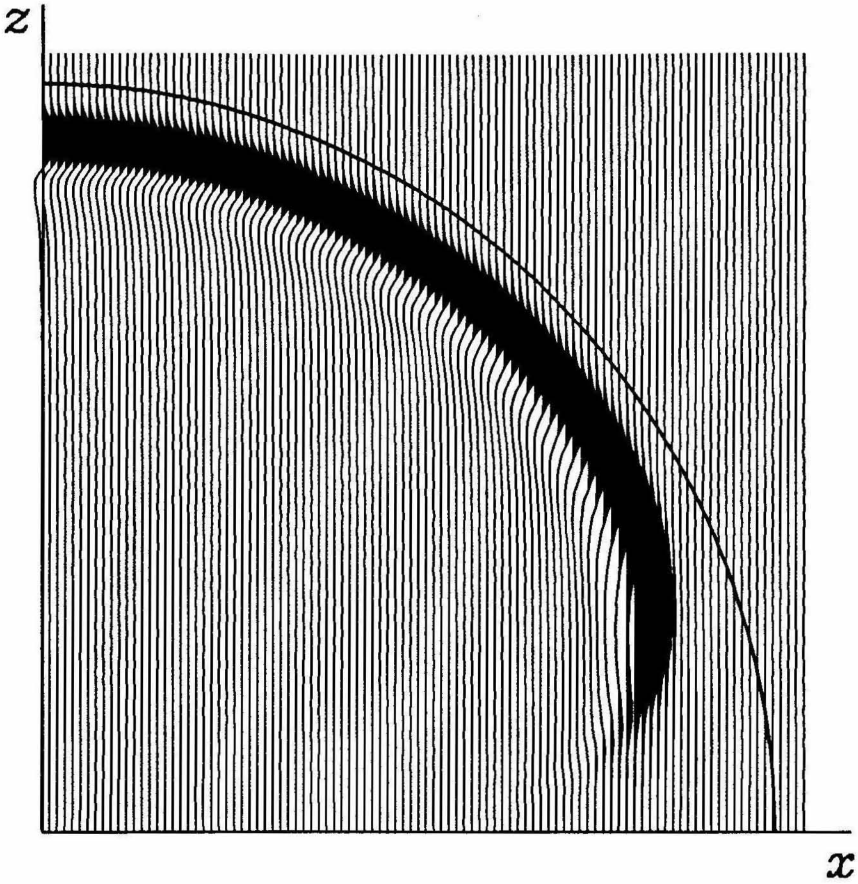

Figure 1.5. Same calculation as Figure 1.4 except dipfilter operator has been applied at each extrapolation step. Energy in the evanescent zone is significantly reduced in this calculation.

relation

$$\partial_z \begin{pmatrix} P_f \\ P_b \end{pmatrix} = \begin{pmatrix} i\alpha & 0 \\ 0 & -i\alpha \end{pmatrix} \begin{pmatrix} P_f \\ P_b \end{pmatrix} + \mathbf{S} \begin{pmatrix} P_f \\ P_b \end{pmatrix} \tag{1.35}$$

where

$$\mathbf{S} = \frac{s}{\Delta z} \begin{pmatrix} 1 & -1 \\ -1 & 1 \end{pmatrix} \quad \text{and} \quad s = \frac{-\Delta z}{2} \left[\frac{1}{\alpha}\rho\right] \left[\frac{1}{\rho}\alpha\right]_z \tag{1.36}$$

as determined from equations (1.7) and (1.9). The subscript z in the above equation refers to differentiation of that term with respect to the variable z. Writing the system (1.35) as a set of coupled difference equations, we get

$$P_f^{n+1} - P_f^n = i\phi(P_f^{n+1} + P_f^n) + \frac{s}{2}\left[(P_f^{n+1} + P_f^n) - (P_b^{n+1} + P_b^n)\right] \tag{1.37a}$$

$$P_b^{n+1} - P_b^n = -i\phi(P_b^{n+1} + P_b^n) - \frac{s}{2}\left[(P_f^{n+1} + P_f^n) - (P_b^{n+1} + P_b^n)\right] \tag{1.37b}$$

where $\phi = \alpha\Delta z/2$.

Using these equations to extrapolate an incident forward-scattered wave field,P_f^n, from depth step z_n to depth step z_{n+1}, we would expect to generate a transmitted (forward-scattered) wave field, P_f^{n+1}, at step z_{n+1} and a reflected (backscattered) wave field, P_b^n, at step z_n. In addition, since there is no incident backscattered field, we can set $P_b^{n+1} = 0$. Solving for the unknown fields P_b^n and P_f^{n+1}, we have

$$P_b^n = \left[\frac{s}{1+\phi^2}\right] P_f' \tag{1.38a}$$

$$P_f^{n+1} = \left[1 + \frac{s}{1+\phi^2}\right] P_f' \tag{1.38b}$$

where

$$P_f' = \frac{(1+i\phi)}{(1-i\phi)} P_f^n. \tag{1.39}$$

In deriving these relations, we have neglected terms arising from the operator α acting on s and the operator s acting on itself.

Examining equations (1.38), we see that the operator $\frac{s}{1+\phi^2}$ is analogous to a reflection coefficient. When $s = 0$ (homogeneous medium), these relations reduce to

$$P_b = 0 \tag{1.40a}$$

$$P_f^{n+1} = \frac{(1+i\phi)}{(1-i\phi)} P_f^n \tag{1.40b}$$

the second of which is simply the difference form of the propagation system given by equation (1.11). When s is nonzero, P_f' is first calculated from equation (1.39) using the techniques described in the previous section and then, P_b^n and P_f^{n+1} can be computed from equations (1.38a) and (1.38b).

In order to implement these equations, we must again use a suitable approximation for α. The zeroth order approximation ($\alpha_0 = \omega/v$) yields the following

$$\frac{s}{1+\phi^2} \approx \frac{1}{(1+\zeta^2)} \frac{\Delta z}{2} \left(\frac{\rho_z}{\rho} + \frac{v_z}{v} \right) \qquad \zeta = \frac{\omega \Delta z}{2v} \tag{1.41}$$

with $\rho_z = \partial\rho/\partial z$ and $v_z = \partial v/\partial z$. This expression is exact for normally incident plane waves in a layered medium. Higher order formulations can be developed by using more accurate representations for α. These expressions tend to be mathematically cumbersome and are not presented here. In the examples presented in this chapter, we have used the plane wave approximation for the scattering term. Since we are mainly interested in modeling problems in which most of the energy is traveling along the propagation axis, the zeroth order approximation is probably adequate for these cases.

1.5 Source excitation

To initialize the extrapolation process, we can either specify a force or volume injection source to be used directly in equation (1.10) or alternatively, we can specify an entire wave field along one x-y plane of the model space. Both of these approaches are outlined below.

1.5.1 The general form of the source term

Including a force or volume injection source directly in the extrapolation system is the most general way to initialize the extrapolation process. The derivation given below is similar to that presented by Wapenaar (1990) for application to pre-stack migration using a one-way extrapolation scheme.

The extrapolation equation for forward-scattered waves, including the source term, is given by [from equation (1.10)]

$$\partial_z P_f = i\alpha P_f + f_s, \tag{1.42}$$

where

$$f_s = \frac{1}{2}\left(\frac{1}{i\alpha}\omega^2 \rho f_V - f_z\right)$$

is the source containing the z-oriented body force, f_z, and the isotropic volume injection source, f_V. We have neglected the body force terms f_x and f_y since these radiate very little energy along the extrapolation direction. Following the same derivation as performed in section 1.3, we can approximate α with a second-order expression and use this in the difference form of equation (1.42) to obtain

$$\begin{aligned}&\zeta^{-1}(P_f^{n+1} - P_f^n)\\ &\quad = i\big[1 + B(D_x^2 + D_y^2)\big]^{-1}\big[1 + A(D_x^2 + D_y^2)\big](P_f^{n+1} + P_f^n) \quad + \quad \Delta z f_s,\end{aligned} \tag{1.43}$$

where the source f_s is centered at $z = z_{n+1/2}$. Solving for the unknown wave field P_f^{n+1}, we have

$$\{1 + \frac{1}{v}B(D_x^2 + D_y^2)v - i\zeta[1 + A(D_x^2 + D_y^2)]\}P_f^{n+1} = f, \tag{1.44}$$

where

$$f = \Delta z\big[1 + \frac{1}{v}B(D_x^2 + D_y^2)v\big] f_s \tag{1.45}$$

and we have set $P_f^n = 0$ since we are only concerned with the forward-scattered (positive z) portion of the source. Given f, equation (1.44) can be solved for P_f^{n+1} using equations (1.24).

Obtaining f from equation (1.45) is non-trivial due to the nature of the terms in f_s. This is readily seen by expanding equation (1.45) using the expression for f_s (note that for notational simplicity, we will now restrict our derivation to the case of a homogeneous medium),

$$f = \frac{\Delta z}{2}\big[1 + B(D_x^2 + D_y^2)\big]\big(\frac{1}{i\alpha}\omega^2 \rho f_V - f_z\big). \tag{1.46}$$

If we have only the body force term, f_z, the solution of equation (1.46) is straightforward. However, in the more general case where we have a volume injection source, f_V, we need to derive a rational expression for the term α^{-1} in order to calculate f.

The plane wave approximation $\alpha^{-1} \approx v/\omega$, gives us

$$f = -\frac{\Delta z}{2}\left[1 + B(D_x^2 + D_y^2)\right]\left(i\omega v\rho f_V + f_z\right). \tag{1.47}$$

Notice that the term, $i\omega v\rho f_V$, appears in this equation in the same manner as the body force term f_z. Thus, using equation (1.47), the volume injection source will not be isotropic, but will have a radiation pattern similar to that of the body force. To obtain a more accurate expression, we use a Taylor expansion for α^{-1}, i.e.,

$$\alpha^{-1} = \frac{v}{\omega}\left\{1 - \frac{1}{2}(D_x^2 + D_y^2) + O\left[(D_x^2 + D_y^2)^2\right]\right\}.$$

Using this in equation (1.46) and neglecting terms of $O\left[(D_x^2 + D_y^2)^2\right]$, we obtain

$$f = -\frac{\Delta z}{2}\left\{\left[1 + (B - \frac{1}{2})(D_x^2 + D_y^2)\right](i\omega v\rho f_V) + \left[1 + B(D_x^2 + D_y^2)\right]f_z\right\}. \tag{1.48}$$

This expression does a good job of approximating the isotropic nature of the volume injection source as will be demonstrated later by example.

1.5.2 Point source implementation

We now consider the specific case in which the sources of the system are point sources, i.e.,

$$f_z = S_z(\omega)\delta(x - x_s)\delta(y - y_s)\delta(z - z_s) \tag{1.49a}$$

and

$$f_V = S_V(\omega)\delta(x - x_s)\delta(y - y_s)\delta(z - z_s) \tag{1.49b}$$

where $S_z(\omega)$ and $S_V(\omega)$ are the temporal Fourier transforms of the respective source time functions, $\delta(u)$ is the Dirac delta function and the sources are located at (x_s, y_s, z_s). Using this formulation, distributed sources can also be simulated by the summation of individual point sources.

One concern with using point sources is that the delta function has equal power for all wavenumbers. Recall from section 1.3.5, that the accuracy of the paraxial system for large wavenumbers [i.e., $\frac{v^2}{\omega^2}(k_x^2 + k_y^2) > 1$] is very poor and energy propagating in this region can produce significant artifacts (see Figure 1.4). Suppression of this energy from the source can be accomplished using a dip filter of the form of equation (1.34) applied to the source term, f, calculated from equation (1.48). Using a filter with a sharp cutoff between the pass and reject zones works best and we have produced excellent results using the parameters $\epsilon = 0.1$ and $n = 8$. Implementation of this filter in the spatial domain is described in Appendix B.

1.5.3 Numerical example

To illustrate the response of the paraxial system to the source implementation discussed above, we consider the following example. For simplicity, we will restrict ourselves to the 2-D case. The model geometry for this experiment is shown in Figure 1.6. The medium containing the source and receivers is homogeneous and the distance r_0 is made long enough so that the receivers are in the far-field. For a body force oriented along the z-axis, the theoretical amplitude along the receiver array is given as

$$A(\theta) = \frac{(\cos\theta)^{3/2}}{\sqrt{r_0}} A_0 \tag{1.50}$$

(Aki and Richards, 1980, p. 75) and for an isotropic line source, the response is

$$A(\theta) = \sqrt{\frac{\cos\theta}{r_0}} A_0 \tag{1.51}$$

where A_0 is the normalized source amplitude. Figure 1.7 compares these theoretical curves with numeric values measured from seismograms calculated with the paraxial technique for both types of sources. In both cases, the numerical technique does a good job in matching the expected values. At propagation angles near 60° (the accuracy extent of the paraxial system), the error in amplitude is less than 5 percent for both sources and with decreasing propagation angle, the fit becomes much better.

It is interesting to note that for high propagation angles, the body force calculation overestimates the theoretical curve, while the isotropic line source calculation underestimates the theoretical curve. The reason for this behavior is due to the nature of the paraxial operators themselves and is independent of the type of source. For large propagation angles, i.e., large wavenumbers, the operators map the actual wavenumber to an "apparent" wavenumber which is slightly smaller in magnitude (Claerbout, 1985a, p. 247). The result is that the energy propagating at angles near the accuracy extent of the given paraxial system tends to be

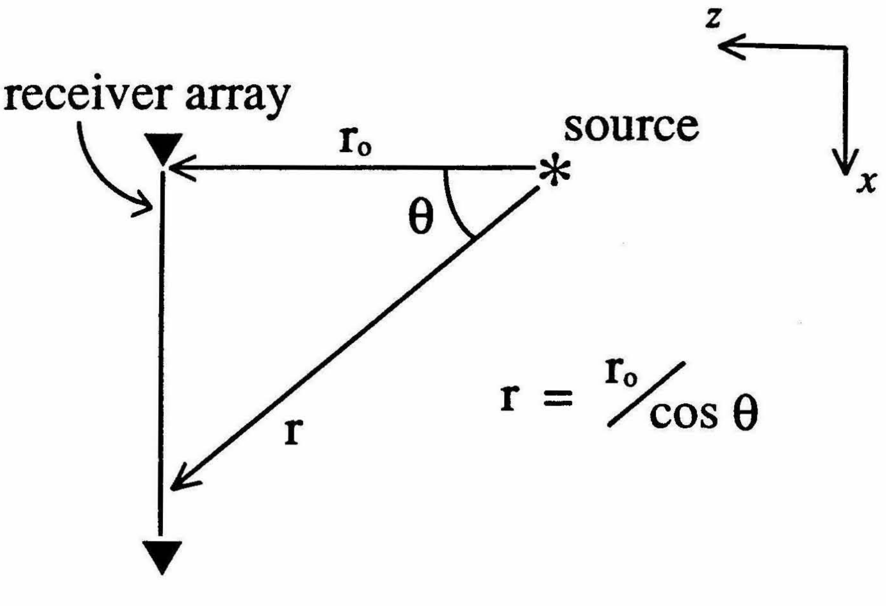

Figure 1.6. Model geometry for experiment comparing body force type source and isotropic line source.

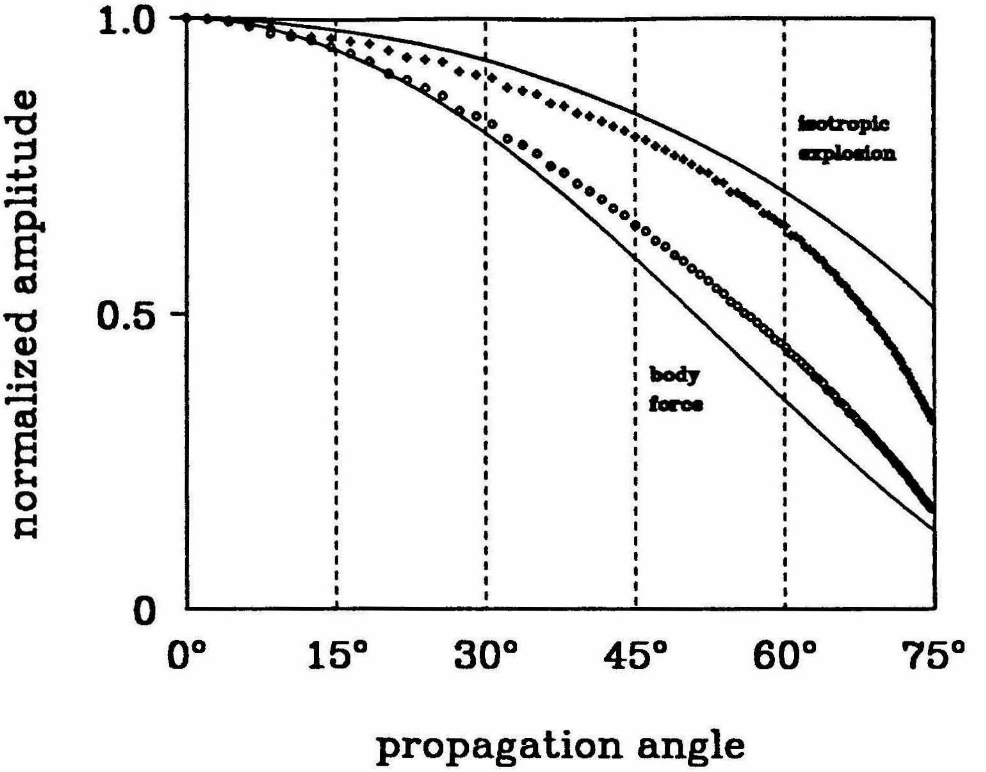

Figure 1.7. Plot of amplitude vs. propagation angle for the line of receivers shown in figure 1.6. Numeric values measured from seismograms calculated for this model are shown for the body force type source (open circles) and for an isotropic explosion (small crosses). Solid lines are for theoretical values computed from equations (1.50) and (1.51), respectively.

overestimated. Clearly, the mismatch is not bad for the 60° system, but for lower order operators such as the 15° system, the mismatch can be quite significant. In spite of this effect, the power of the isotropic source is still underestimated at high propagation angles. The reason is that this source only contains a body force term plus a second-order correction term [see equation (1.48)]. At high propagation angles, the second-order correction term provides a poor approximation to the proper response, thus offsetting the amplification of energy due to the extrapolation operators themselves.

1.5.4 Initial wave field specification

The second approach for initialization of the extrapolation process is to specify the wave field along one x-y plane of the model space. By convention, this plane is designated as $(x, y, z = z_0)$ with the initial wave field denoted as $P_f^0 = P_f(x, y, z = z_0, \omega)$. With knowledge of P_f^0, we can then use equations (1.24) to extrapolate the wave field throughout the entire model space.

In general, the wave field P_f^0 may be determined by numerical or analytical techniques or may also be specified by an observed wave field as is the case with migration. This flexibility allows the extrapolation method to be coupled with a wide variety of other wave propagation techniques.

In the 2-D and 3-D examples shown later in this chapter, we have used an analytic expression to represent the initial wave field P_f^0. The source location may by set inside or outside of the actual computational grid and the analytic response due to the source is then calculated for all grid points in the plane $(x, y, z = z_0)$.

For 3-D calculations, the initial pressure field is given by

$$P_f^0 = S(\omega) \cdot \frac{1}{r} \cdot \exp(i\omega r/v) \tag{1.52}$$

where $r = \left[(x - x_s)^2 + (y - y_s)^2 + (z_0 - z_s)^2\right]^{1/2}$. For 2-D calculations, the exact line source representation is given in the frequency domain by the Hankel function of order zero. Using the asymptotic or far-field approximation to this, we have

$$P_f^0 = S(\omega) \cdot \sqrt{i/(\omega r)} \cdot \exp(i\omega r/v) \tag{1.53}$$

where $r = \left[(x - x_s)^2 + (z - z_s)^2\right]^{1/2}$. In each of the above equations $S(\omega)$ is the temporal Fourier transform of the source time function and the source is located at (x_s, y_s, z_s).

For display purposes, we would like to make the 2-D calculations appear as if they were initiated with a point source and thus enable us to more accurately compare 2-D and 3-D computations. Examining equations (1.52) and (1.53), we see that they only differ by a factor of $\sqrt{-i\omega/r}$. This represents the difference in geometric spreading between the line source and point source. Although we cannot explicitly account for this spreading difference within the calculations, the 2-D solutions can be modified after the fact by multiplication with an additional factor of $\sqrt{-i\omega/r}$. This process will only be approximate though, since we will not know the exact length r of the travel path for a given arrival.

1.6 Implementation considerations

1.6.1 Computational attributes

A major advantage of using the first-order extrapolation system given by equation (1.10) is that the system only requires knowledge of the wave field at the previous depth step in order to calculate the solution at the present depth step. Computationally, this means that 2-D problems can be solved by stepping through the model with the solution being calculated only along a one-dimensional vector, and likewise, 3-D problems can be solved by extrapolation of the solution on a two-dimensional plane. This effectively reduces active storage requirements by one-dimension as compared to complete wave solution techniques. Thus, large 2-D and even realistic 3-D problems can be handled by existing computers.

By casting the extrapolation system in the frequency domain, we have the opportunity to apply weighting functions to the individual frequency components while the solution is being calculated. This allows for the implementation of various types of filters to the wave field and also allows us to model attenuation and viscoelastic effects as an arbitrary function of frequency.

Another advantage of formulating the extrapolation equations in the frequency domain is that solutions can be calculated for each frequency component independently. This makes the system highly suitable for implementation on parallel or vector processing computers. In this type of configuration, the solutions for a number of different frequencies can be generated simultaneously on separate processors or in sequence on a vector processor.

1.6.2 Time-slices and movies from a limited number of frequencies

The production of time slices and movies is quite efficient for the paraxial operators because they are cast in the frequency domain. The trick is to arrange for the source to periodically emit a source pulse. If for display purposes, a source wavelet that is a single cycle of a sinusoid is adequate, then this can be accomplished with a small number of frequencies.

To demonstrate this, consider a simple pulsating source function. The source emits a sinusoidal wavelet of width τ every $n\tau$ seconds. The initial pulse is shifted a seconds from $t = 0$. A mathematical description of this source is given by

$$s(t) = \begin{cases} \exp[i2\pi(t-a)/\tau + i\phi], & \text{if } t_0 - \tau/2 \le t \le t_0 + \tau/2; \\ 0, & \text{otherwise;} \end{cases} \tag{1.54}$$

where $t_0 = (ln\tau) + a$; $(l = -\infty, \cdots, -1, 0, 1, \cdots, \infty)$, and ϕ is the initial phase of the source. The periodicity of the source makes it a candidate for a Fourier series representation.

$$s(t) = \sum_{k=-\infty}^{\infty} c_k \exp\left[i2\pi \frac{kt}{n\tau}\right] \tag{1.55}$$

Solving for the c_k we have

$$c_k = \frac{1}{n} \exp\left[i\phi - i2\pi \frac{ak}{n\tau}\right] \mathrm{sinc}\big[\pi(1 - k/n)\big] \tag{1.56}$$

where sinc(x) is the usual $\sin(x)/x$ function. A reasonable representation of the source can be achieved with only the $2n - 1$ frequencies (Fourier coefficients $k =$

1, ⋯, 2n−1) that sample the central peak of the sinc function. This is demonstrated in Figure 1.8a, where we have set $n = 4$ and computed $s(t)$ for various numbers of frequencies. Note that a very good result is obtained for as few as seven frequencies. Increasing the value of n will make the time separation between successive pulses greater (Figure 1.8b).

To make time-slices then, the solution is summed with the weights given by equation (1.56). That is

$$slice(x, y, z) = \sum_{k=1}^{2n-1} c_k(a, \phi, n) P_f(x, y, z, \omega = \frac{2\pi k}{n\tau}) \tag{1.57}$$

The multiple time-slices for a movie are constructed by simply marching the shift factor a from 0 to $n\tau$, at which point the *film loop* will repeat. This process is demonstrated in Figure 1.8c.

1.7 Examples

1.7.1 2-D example: Fault block model

In this example, we compare results from the paraxial extrapolator (PE) technique with a conventional time-domain FD calculation for the simple fault block model shown in Figure 1.9. For this comparison, the source time function is given by the first derivative of a Gaussian pulse, i.e.,

$$s(t) = t \exp(-t^2/a^2) \tag{1.58}$$

where we have set $a = 0.015$s. The source amplitude spectrum peaks at about 15 Hz and has significant power out to 45 Hz. The grid spacing in the PE calculation

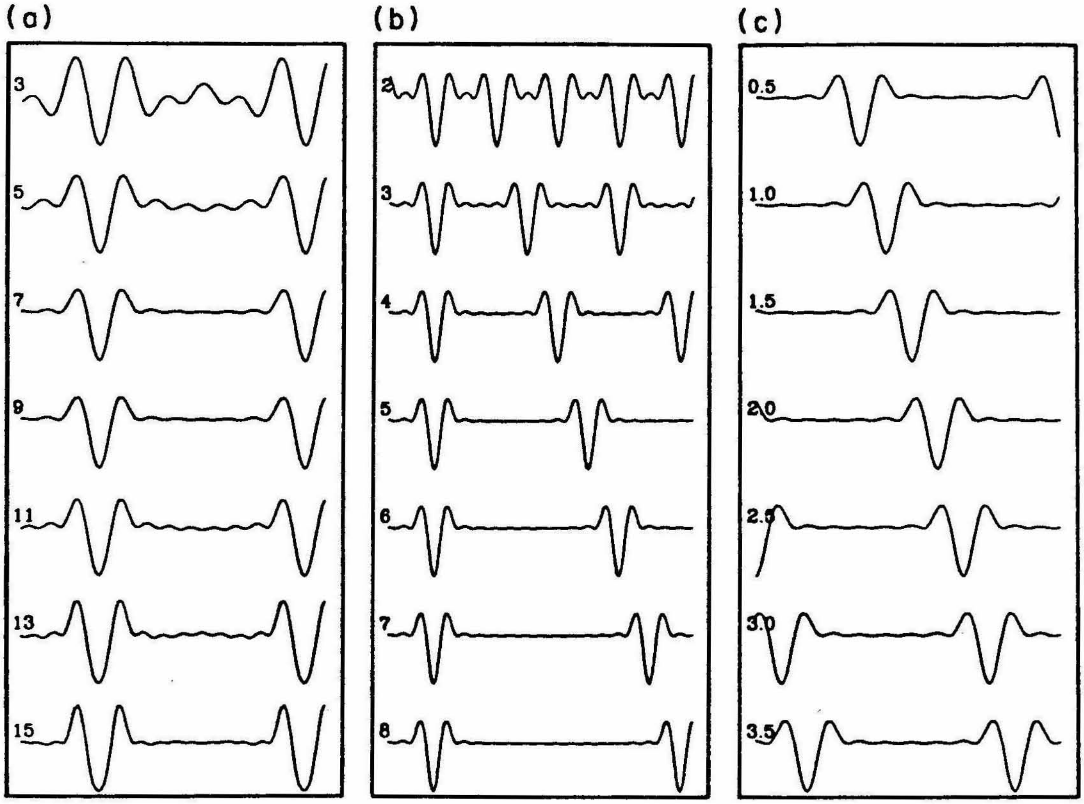

Figure 1.8. Representation of periodic source time function. (a) Source representation computed by summation for various numbers of frequencies (shown to the left of each trace) for $n = 4$. (b) Source representation for different values of n (shown to the left of each trace) with $nw = 7$. (c) Movie panels obtained by variation of the shift factor a from 0.5τ to 3.5τ $[n = 4, nw = 7]$.

is 5m laterally and 2.5m vertically and in the FD model, the grid spacing is 5m. The output is viewed as both time-slice snapshots (Figure 1.10) and seismograms recorded at the locations indicated in Figure 1.9 (Figure 1.11). First we will discuss the time-slice comparison.

Figure 1.10 shows wave field snapshots at four selected times for both the FD and PE results. Note that the PE result is split into two columns. The first shows the downgoing forward-scattered wave from the source, while the second shows the direct upgoing wave from the source as well as the first-order backscattered wave from the structural interface. Higher order scattering effects (i.e., multiples) are not included in the PE time-slice computation. In addition, it should be noted that the PE results have been corrected to mimic a point source calculation and the FD results have not been so modified. In general, the agreement between the two calculations is quite good. Some of the discrepancies are due to the omission of the higher order scattering effects in the PE results (e.g., the wavefront labeled A at $t = 0.72$s in the FD result is not present in the PE calculation). Other differences can be attributed to artifacts arising from the presence of evanescent energy in the PE calculation (e.g., the wavefront labeled B at $t = 0.52$s in the reverse sweep of the PE result). These artifacts are usually not significant and in most cases can be easily identified.

Comparing the seismograms in Figure 1.11, we again see a very good overall agreement between the two techniques. In particular the results from the two methods computed at receiver locations #1, #4, and #5 agree very well with one

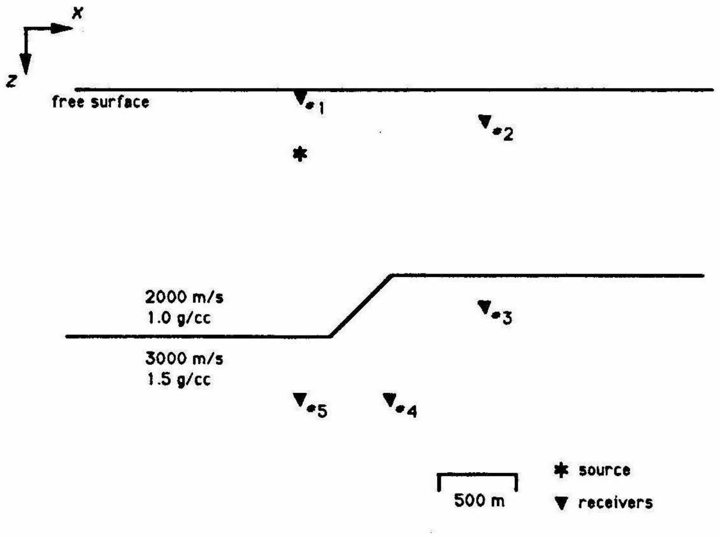

Figure 1.9. Fault block model showing media variations as well as source and receiver locations.

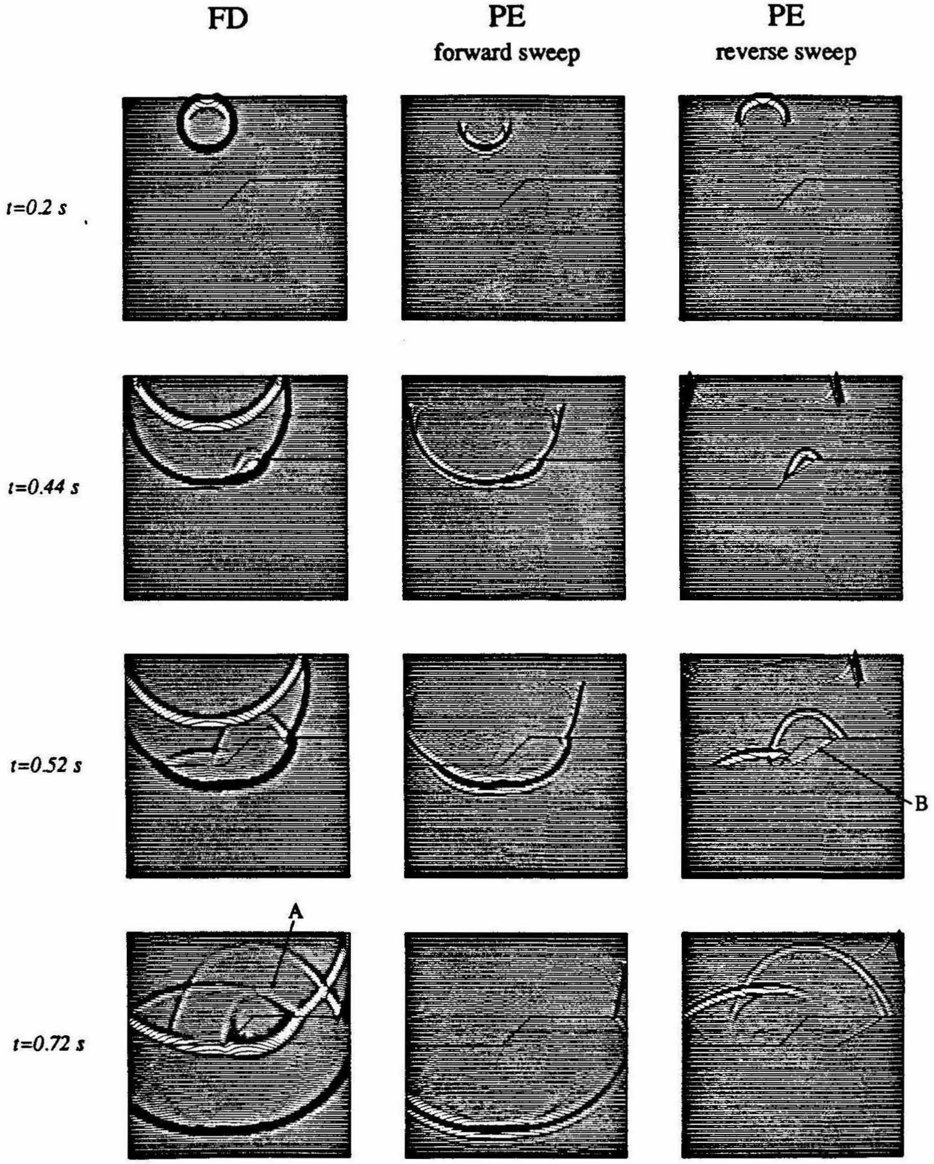

Figure 1.10. Time-slice comparison for fault block model. FD result (left panel), PE forward sweep result (middle panel) and PE reverse sweep result (right panel). Labeled wavefronts are discussed in text.

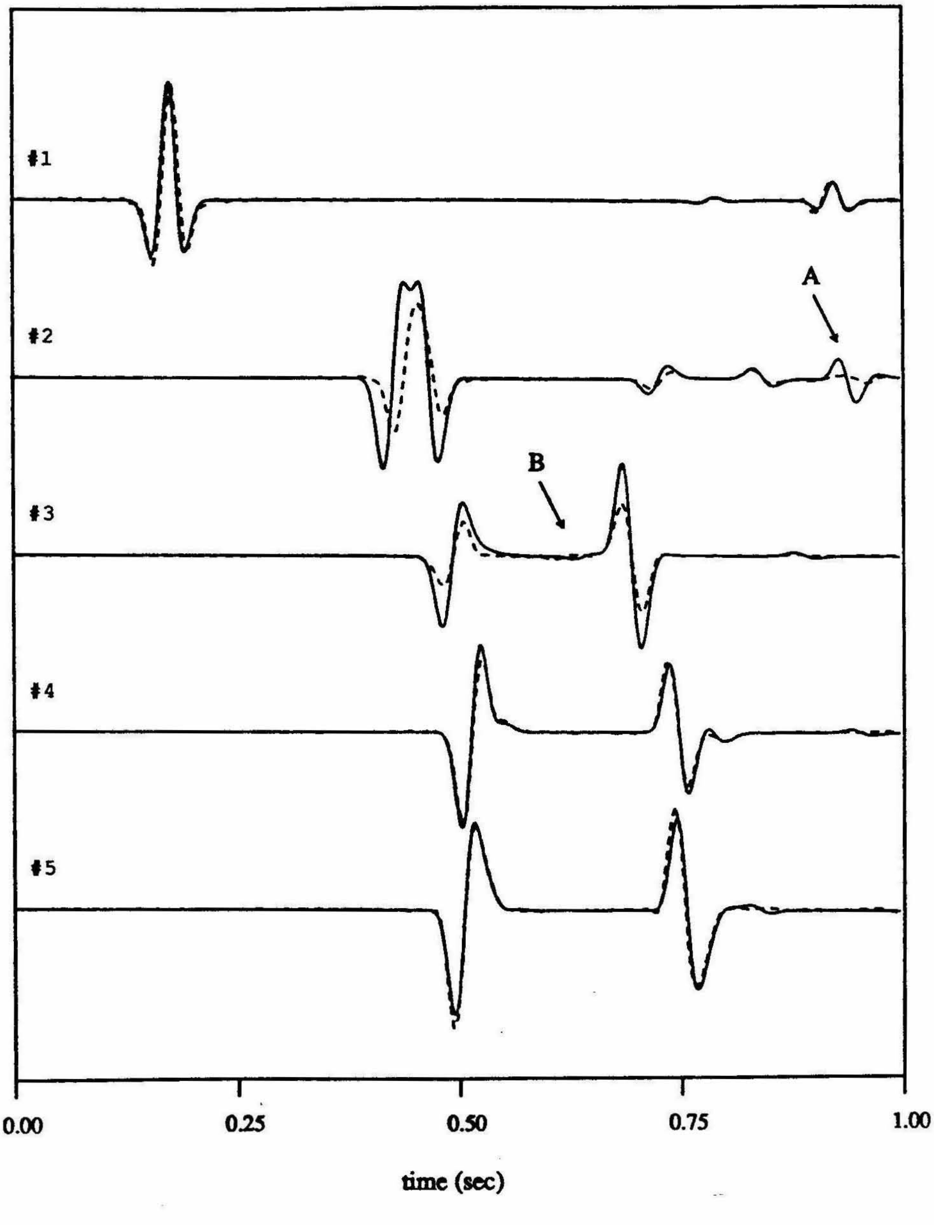

Figure 1.11. Seismogram comparison for fault block model. Solid line is FD result and dashed line is PE result. See figure 1.9 for receiver positions.

another in both timing, phase and amplitude. Note that for this comparison, both sets of results have been transformed to mimic point source calculations.

At receiver location #2 the PE result does not do so well in matching the arrivals predicted by the FD result. The reason for this is that most of the energy arriving at this location is propagating at about 85° with respect to the extrapolation direction. Since the paraxial approximation is only accurate out to 60° we would not expect to model this energy correctly. As indicated by this comparison, waves which are propagating at angles outside the range of validity of the paraxial approximation are still modeled, although they travel at a group velocity which is slower than the correct value. If we were interested in modeling this energy more accurately, we could rotate the PE grid by 90° and then extrapolate the solution horizontally. The arrival labeled A on this record corresponds to the wavefront A in Figure 1.10.

Moving on to the result at location #3, we see that the timing and phase of the two calculations agree quite well; however, the amplitude of the PE result is significantly less than that predicted by the FD calculation. Energy arriving at this station propagates across the overlying layer boundary with an incidence angle between 35° and 40°. Since the velocity and density increase at this interface, the transmission coefficient grows as the angle of incidence is increased. However, as discussed previously, we have approximated the transmission coefficient with its value at normal incidence and consequently, we have underestimated the strength of the transmitted energy as computed in the PE result. The arrival labeled B on this record corresponds to the artifact B in Figure 1.10. Note that this arrival has very little energy and does not interfere with the rest of the signal.

1.7.2 3-D example: Crustal basin

Due to a variety of constraints, 2-D models are often used as approximations for structures which are known to be 3-D. In many cases, this approximation is valid and worthwhile results can be obtained from this type of analysis. However, as we attempt to more fully understand the details of seismological processes, we must begin to address these problems in their full 3-D context.

This is illustrated in the following example, where we show a comparison between solutions generated for a 3-D model and a 2-D approximation to this model. The model consists of a simple low velocity basin situated in a higher velocity background medium (Figure 1.12). Along the top of the model we have imposed a free-surface boundary condition and all other model boundaries are absorbing. Note that the 2-D model is obtained by taking a vertical cross-section of the 3-D model along the strike of the survey line (xz plane, Figure 1.12). For the 2-D model, we have computed the result using both conventional finite-differences and the PE technique. The grid spacing for the PE calculations is 10m in the x and y directions and 5m in the z direction. In the FD model, the grid spacing is constant at 10m. The source time function is the same as in the previous example, except here we have $a = 0.02$s. The amplitude spectrum of this source peaks at about 12 Hz.

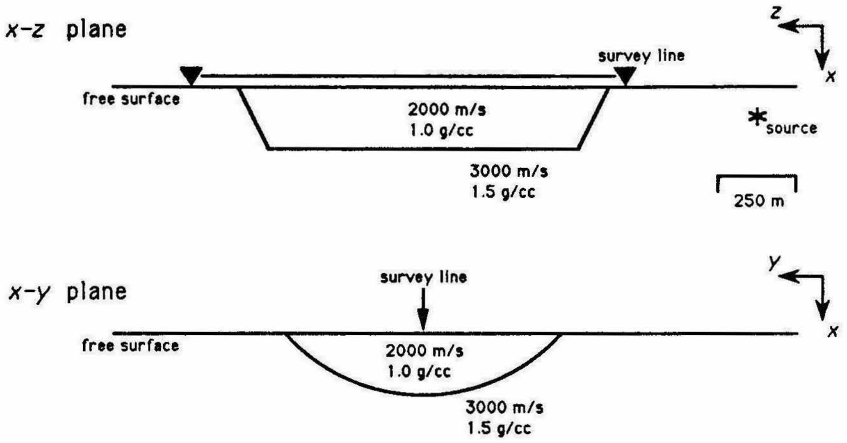

Figure 1.12. Model geometry and media parameters for 2-D vs. 3-D comparison. Top panel shows xz plane along strike of the survey line. Source location is within this plane. In addition, this slice represents the model used in the 2-D calculations. Bottom panel shows cross-line model structure for 3-D calculation.

The solutions for both models are displayed as time sections recorded at regular intervals along the survey line (Figure 1.13). In the PE calculations we have only included contributions from the direct forward-scattered energy for a single pass of the extrapolator through the model. Thus, the far-end backscattered basin reflections seen in the FD result are not present in either of the PE results. In addition, we have accounted for geometric spreading differences by multiplying the results of the 2-D calculation by a scale factor of $\sqrt{-i\omega/r}$ where r is the distance between the source and receiver. The amplitudes in each solution have been normalized to the nearest offset trace.

In this comparison, we will focus our attention on the modeling of the multiply reflected and refracted waves occurring within the basin structure. First, examining the 2-D model results, we see that aside from the omission of the backscattered energy, the PE solution agrees very well with the result obtained using the FD technique. Comparing the 2-D results with the 3-D result, we find that in many respects, the nature of the 2-D solutions are quite similar to the results of the 3-D calculation. The timing and phase for many of the arrivals within the basin agree well between the two models. For these considerations, the 2-D model may well be an appropriate substitute for the 3-D structure. However, the 2-D model clearly fails to correctly model the amplitudes of the arrivals within the basin. In fact, the 3-D solution shows arrivals which are more than two times stronger in amplitude than the corresponding arrivals in the 2-D sections. In addition, the coda of the 3-D records is much more complicated than that seen in the 2-D results, 2D basin model (FD)

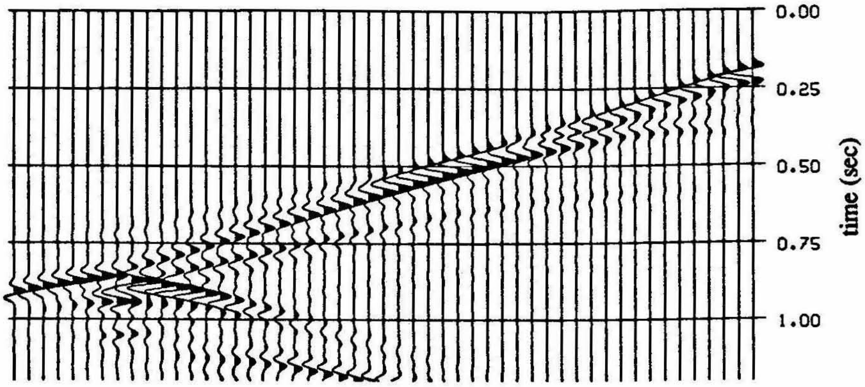

2D basin model (PE)

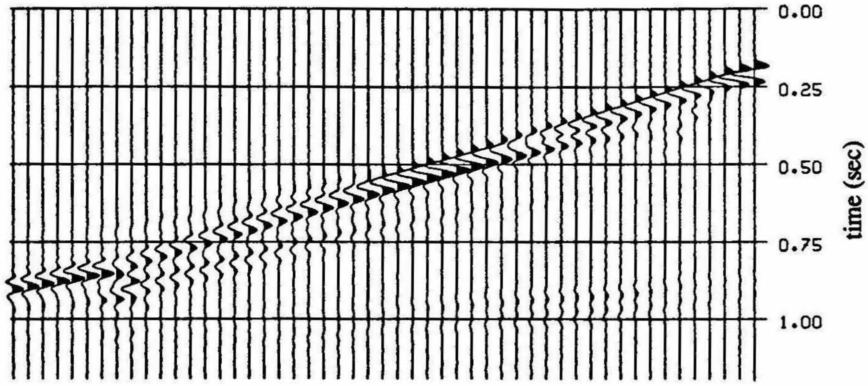

3D basin model (PE)

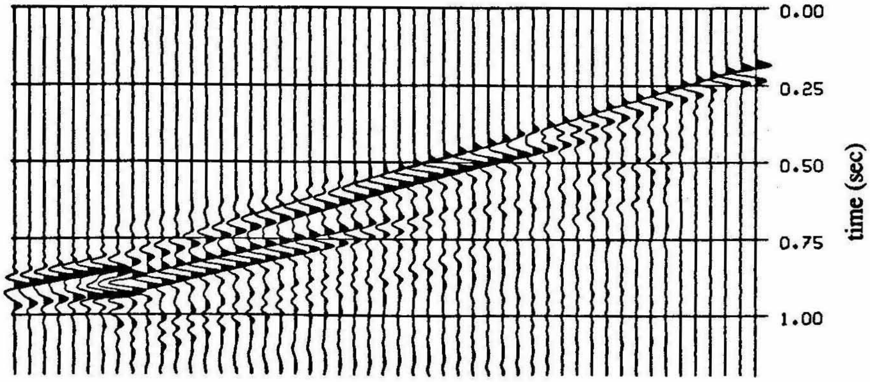

Figure 1.13. Time sections along survey line for basin model comparison. 2-D FD result (top panel), 2-D PE result (middle panel) and 3-D PE result (bottom panel).

indicating the presence of cross-line structure. This strong focusing of energy in the 3-D calculation is caused by the the sloping edges of the basin floor. Although the dip of these boundaries is not extreme, the results are quite significant.

Unfortunately there is no way to account for this scattering phenomena in the 2-D calculation. In order to produce similar results using a 2-D model, we would need to alter the media parameters and possibly change the geometry of the basin as well. Either of these choices would result in an incorrect interpretation of the structure for this experiment.

1.8 Conclusions

In this chapter we have presented an approximate numerical technique in which acoustic waves are modeled using a system of paraxial extrapolators. The technique is developed by casting the equations of motion in the frequency domain and then formulating them as a first-order spatial extrapolation system. This approach is attractive because it requires significantly less computer memory as compared to more complete methods such as conventional time-domain finite-difference calculations. In fact, when using the paraxial method for large 2-D and 3-D problems, the model size is primarily determined by the time required to perform the necessary computations rather than being restricted by memory availability and/or accessibility.

To obtain an estimate of the computational requirements of the paraxial method, we consider the following comparison. Performing an explicit fourth-order time-domain finite-difference calculation on a constant density 3-D model requires on the order of 50 floating point operations (*fpo*) per grid point per time step. For the same model, one pass of the paraxial method (including the phase correction operator) requires about 500 *fpo* per grid point per frequency. However, the number of time steps needed for the finite-difference calculation is typically an order of magnitude greater than the number of frequencies needed for the paraxial calculation. From this, we conclude that both methods generally require the same order of operations to compute a given solution.

Obviously, to model problems in which the effects of higher order scattering are important will require more than one pass with the paraxial technique; however, the cost to do this only increases linearly with the number of passes performed. Furthermore, the explicit separation of the wave field into its forward-scattered and backscattered components as provided by the paraxial method is desirable and, in fact, sometimes necessary in the study of many wave propagation problems.

Chapter 2

Wide Angle One-way Wave Field Extrapolation

2.1 Introduction

Since the introduction of the parabolic wave equation to the seismic community (Claerbout, 1970), much work has been done to improve the accuracy of the approximations used in the derivation of these types of one-way extrapolation systems. These approximate systems are all based on a truncated series expansion of the exact one-way or square-root propagation operator. The original parabolic system is a first-order approximation which accurately models energy propagating within 15° of the extrapolation direction. To obtain improved accuracy, higher-order terms must be included in the approximation. Following this idea, Berkhout (1979) was able to develop second- and third-order systems which he showed to be accurate for propagation angles out to beyond 50°. A framework for deriving succesively higher-order systems was developed by Francis Muir (Claerbout, 1985a) and is based on using a continued-fraction expansion of the square-root operator.

One drawback with using these high-order systems is that they require the implementation of high-order differential operators. Ma (1981) and Zhang et al. (1988) showed that this problem can be avoided by splitting the high-order equation into a series of low-order equations which can be solved in sequence. This approach is conceptually similar to the one presented here, although it differs significantly in its implementation.

The technique presented here employs the sequential application of a series of second-order systems to obtain a solution to a higher-order system. For example, a fourth-order system can be solved using two second-order systems, a sixth-order system using three second-order systems, and so on. The use of second-order systems is attractive because they are easy to implement on a discrete grid and their numerical behavior is fairly well understood (e.g., stability requirements, boundary conditions, numerical accuracy, etc.). For clarity, a fourth-order system is used to outline the technique; however, extending the approach to higher-order systems is straightforward. The fourth-order equation is initially derived using the continued fraction expansion and is then optimized to be accurate for propagation angles out to nearly 80°. Implementation of the resulting extrapolation system is accomplished as a cascade of two second-order systems which are derived by *factoring* the fourth-order system. This decomposition is exact when the media is laterally invariant and is of the same order of accuracy as the original system when the media is laterally heterogeneous.

In the following discussion, the optimized fourth-order extrapolation system is first presented, followed by a description of the technique in which this system can be factored into a series of second-order systems. Some numerical considerations, including the suppression of artifacts and the implementation of absorbing boundary conditions, are presented in subsequent sections. Finally, this chapter concludes with a discussion of the practical limitations in using this type of approach.

2.2 The one-way wave field extrapolation system

We begin our discussion by considering the 2-D acoustic wave equation appropriate for a homogeneous medium devoid of sources,

$$v^2(\partial_{zz} + \partial_{xx})p = \partial_{tt}p. \tag{2.1}$$

Here, $p(x, z, t)$ is the pressure field, v is the velocity and the symbols ∂_{xx}, ∂_{zz} and ∂_{tt} are used to denote the differential operators $\partial^2/\partial x^2$, $\partial^2/\partial z^2$ and $\partial^2/\partial t^2$.

Transforming this equation into the wavenumber-frequency domain we obtain

$$(k_z^2 + k_x^2)\hat{P} = \frac{\omega^2}{v^2}\hat{P} \tag{2.2}$$

where $\hat{P} = \hat{P}(k_x, k_z, \omega)$ and we have the Fourier transform duals

$$\partial_x \leftrightarrow ik_x, \qquad \partial_z \leftrightarrow ik_z \qquad \text{and} \qquad \partial_t \leftrightarrow -i\omega.$$

Factoring out the wave field $\hat{P}$ from equation (2.2) yields the dispersion relation for the acoustic wave equation

$$(k_z^2 + k_x^2) = \frac{\omega^2}{v^2}. \tag{2.3}$$

Solving for k_z and taking the positive square root, we obtain the dispersion relation for outgoing (positive z) waves

$$k_z = \frac{\omega}{v}(1 - \frac{v^2}{\omega^2}k_x^2)^{1/2}. \tag{2.4}$$

Rewriting this, we have

$$K_z = (1 - K_x{}^2)^{1/2} \tag{2.5}$$

where

$$K_x = \frac{v}{\omega}k_x \qquad \text{and} \qquad K_z = \frac{v}{\omega}k_z$$

are the normalized wavenumbers. Note that equation (2.5) is the wavenumber-frequency domain representation of equation (1.14) and thus represents the exact one-way propagation operator.

Our ultimate goal is to use an expression like equation (2.5) to derive a differential equation which can then be used as a one-way wave field extrapolation system. In order to do this, we need to obtain a suitable expression for the square-root term in equation (2.5). Following the approach of Francis Muir (Claerbout, 1985a, p. 83), we will approximate this expression using a continued fraction expansion. That is, we consider a sequence generated by the recurrence relation

$$K_{z_n} = 1 - \frac{K_x{}^2}{1 + K_{z_{n-1}}} \tag{2.6}$$

with $K_{z_0} = 1$. The first four terms of this sequence are

$$K_{z_1} = 1 - \frac{1}{2}K_x{}^2, \tag{2.7}$$

$$K_{z_2} = \frac{1 - \frac{3}{4}{K_x}^2}{1 - \frac{1}{4}{K_x}^2}, \tag{2.8}$$

$$K_{z_3} = \frac{1 - {K_x}^2 + \frac{1}{8}K_x^4}{1 - \frac{1}{2}{K_x}^2} \tag{2.9}$$

and

$$K_{z_4} = \frac{1 - \frac{5}{4}{K_x}^2 + \frac{1}{8}K_x^4}{1 - \frac{3}{4}{K_x}^2 + \frac{1}{16}K_x^4}. \tag{2.10}$$

These are referred to as the 15°, 45°, 60° and 70° approximations respectively.

The accuracy of these operators is demonstrated in Figure 2.1 where we show the numerical point response of each of the first four paraxial approximations. The 15° and 45° solutions were calculated using the conventional approach, while the 60° and 70° solutions were calculated using the factored system of equations to be described in section 2.2.2. The cusp-like arrivals along the horizontal axes and the sloping arrivals cutting diagonally across the images are numerical artifacts which can be removed with the application of a dipfilter (section 2.2.3).

2.2.1 Optimizing the continued fraction approximation

Following the approach outlined above, the general form of the fourth-order continued fraction approximation to equation (2.5) is given by

$$K_{z_4} = \frac{1 - A{K_x}^2 + BK_x^4}{1 - C{K_x}^2 + DK_x^4}. \tag{2.11}$$

The coefficients A, B, C, and D can be determined from the Muir recursion (i.e., $A = 1.25$, $B = 0.3125$, $C = 0.75$ and $D = 0.0625$); however, an expression which is accurate over a wider range of K_x can be obtained by matching equation (2.11) to

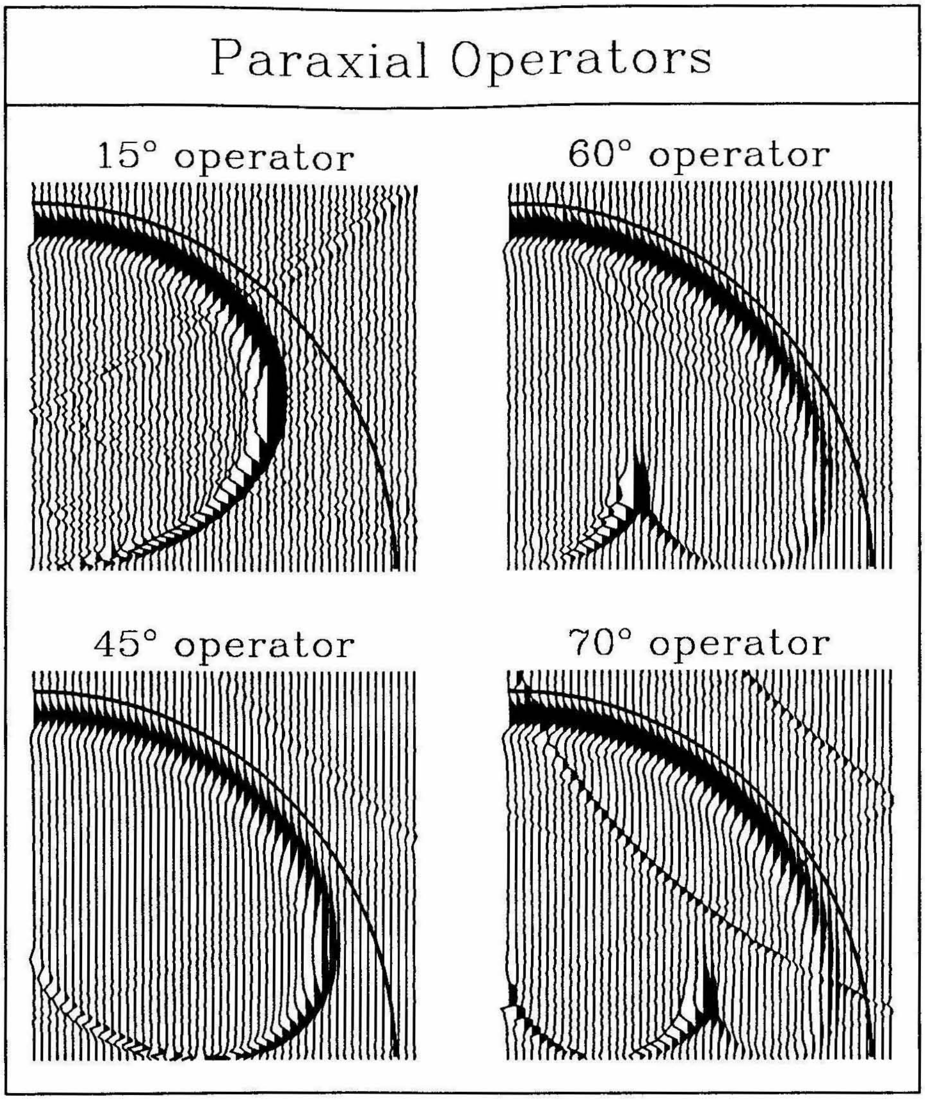

Figure 2.1. Time slices showing the numerical point response of each of the first four paraxial approximations. In each case, a point source was excited at the lower left corner of the model. The proper response for this projection is a quarter-circle as denoted by the heavy curve in each image. The cusp-like arrivals along the horizontal axes and the sloping arrivals cutting diagonally across the images are numerical artifacts which can be removed with a filtering process (section 2.2.3).

equation (2.5) for specific values of K_x and numerically solving for the coefficients (Lee and Suh, 1985; Halpern and Trefethen, 1988). This is illustrated in Figure 2.2 which compares dispersion curves calculated by each of the above methods. For the curve fitting approximation we have fit the exact expression at the points ${K_x}^2 = -0.81, 0.36, 0.64$, and 0.9 which gives $A = 1.434$, $B = 0.457$, $C = 0.933$ and $D = 0.112$.

The left panel of this figure plots these relations in the conventional manner (K_z *vs.* K_x), which allows us to compare the dispersion curves for all propagation angles $0° \leq \phi \leq 90°$. Notice that the curve fitting technique gives a very accurate match to (2.5) for propagation angles out to nearly 80°. In the right panel of this figure, we allow for imaginary values of K_x (${K_x}^2 < 0$) and K_z ($K_z^2 < 0$) to be shown as well. This lets us investigate the behavior of the dispersion curves for evanescent wave propagation. In this case, both of the approximations f_1 and f_2 fit the exact curve very well in the evanescent zone of K_x (i.e., ${K_x}^2 < 0$; exponential decay in x-direction), but diverge completely in the evanescent zone of K_z (i.e., $K_z^2 < 0$; exponential decay in z-direction).

2.2.2 Factoring the extrapolation operator

In order to derive a extrapolation equation from relation (2.11), we proceed in the following manner. First, multiply both sides of equation (2.11) by $\hat{P}$ to obtain

$$K_z\hat{P} = \frac{1 - A{K_x}^2 + BK_x^4}{1 - C{K_x}^2 + DK_x^4}\hat{P}. \tag{2.12}$$

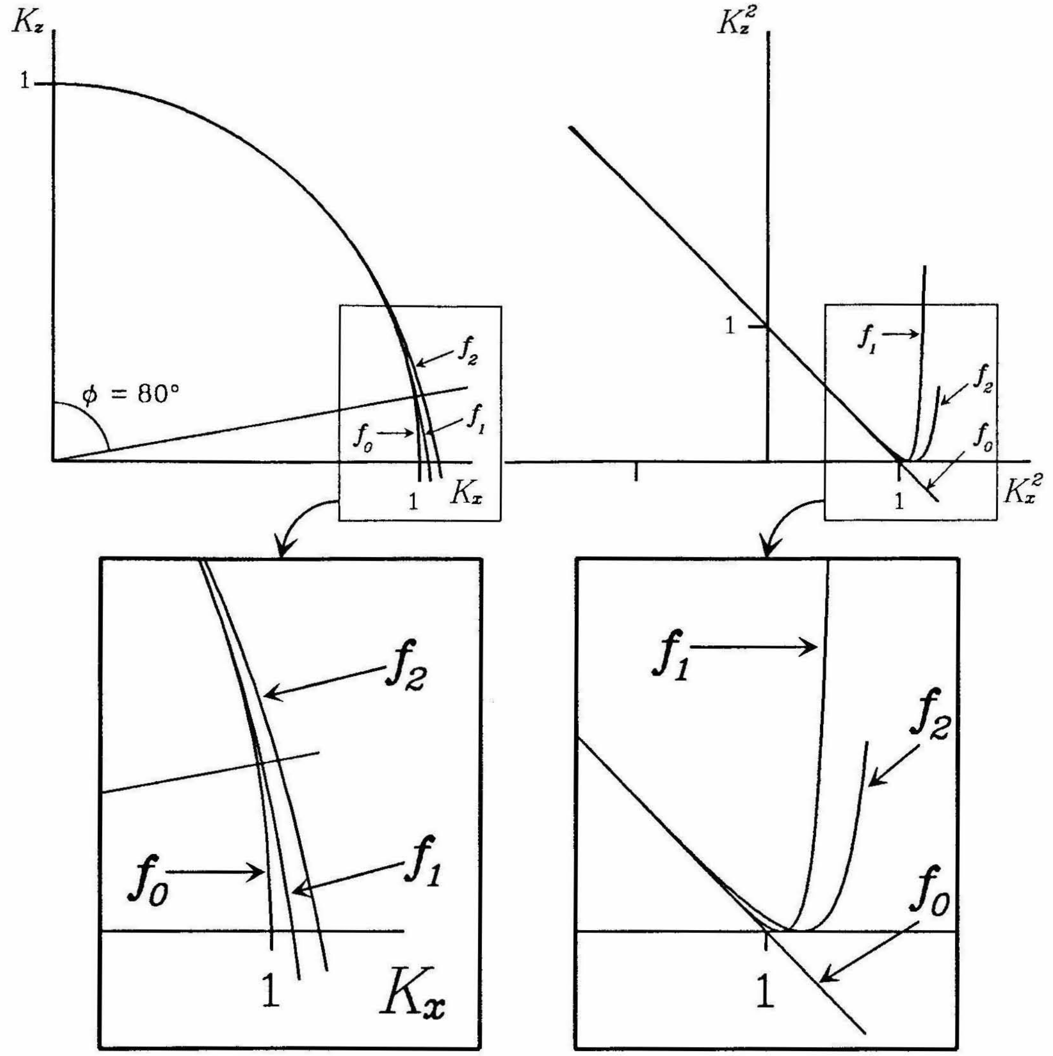

Figure 2.2. Comparison between the exact square-root dispersion relation $f_0 = [1 - {K_x}^2]^{1/2}$ and two fourth-order approximations, f_1 and f_2, which are of the form of equation (2.11). The function f_2 is the Muir approximation and f_1 is a curve-fitting approximation in which the coefficients of equation (2.11) have been chosen to provide a closer match to f_0 in the range $-1 < {K_x}^2 < 1$ (see text for specific values). The left panel plots these relations in the conventional manner (K_z *vs.* K_x) while the right panel allows for imaginary values of K_x (${K_x}^2 < 0$) and K_z ($K_z^2 < 0$) to be shown. The expanded views at the bottom of the figure illustrate the details within the boxed area of each panel.

Then, clearing the denominator and performing an inverse Fourier transform with respect to the wavenumber k_z on the resulting equation, we have the following differential equation

$$\left(1 - C{K_x}^2 + DK_x^4\right)\partial_z\tilde{P} = i\frac{\omega}{v}\left(1 - A{K_x}^2 + BK_x^4\right)\tilde{P} \tag{2.13}$$

where $\tilde{P} = \tilde{P}(k_x, z, w)$. The corresponding Crank-Nicolson finite-difference equation is given by

$$\left(a - b{K_x}^2 + cK_x^4\right)\tilde{P}^{n+1} = i\zeta\left(a^* - b^*{K_x}^2 + c^*K_x^4\right)\tilde{P}^n \tag{2.14}$$

where

$$a = 1 - i\zeta, \quad b = C - iA\zeta, \quad c = D - iB\zeta \quad \text{and} \quad \zeta = \frac{\omega\Delta z}{2v},$$

$\tilde{P}^n = \tilde{P}(k_x, z = z_n, w)$ and the asterisk $(*)$ denotes complex conjugate. Finally, performing an inverse Fourier transform with respect to the wavenumber k_x on equation (2.14) yields the extrapolation equation

$$\left(a + bD_x^2 + cD_x^4\right)P^{n+1} = i\zeta\left(a^* + b^*D_x^2 + c^*D_x^4\right)P^n \tag{2.15}$$

with $P^n = P(x, z = z_n, w)$ and $D_x = \frac{v}{\omega}\partial_x$. The conventional approach to solve equation (2.15) for the unknown wave field P^{n+1} is to discretize the x-axis, approximate the differential operators with finite-difference operators and then solve the resulting matrix equation. However, this procedure requires the inversion of a pentadiagonal matrix (from the D_x^4 term) and this operation may not aways be stable particularly when the media parameters vary in the x dimension. A way to avoid this problem is to factor the operators in equation (2.15) as follows

$$(a + bD_x^2 + cD_x^4) = c(D_x^2 - x_1)(D_x^2 - x_0) \tag{2.16}$$

Using this factorization, we obtain the following series of equations

$$(D_x^2 - x_0)P' = (D_x^2 - x_0^*)P^n, \tag{2.17a}$$

$$(D_x^2 - x_1)P'' = (D_x^2 - x_1^*)P' \tag{2.17b}$$

and

$$cP_f^{n+1} = c^* P''. \tag{2.17c}$$

Discretizing the x-axis and using a second-order finite-difference approximation for D_x^2 reduces equations (2.17a) and (2.17b) into tridiagonal matrix systems for which solutions are easily generated (e.g., Claerbout, 1985a, p. 98). In addition, the solution of these tridiagonal systems can be guaranteed to be stable even in the presence of laterally varying media.

The validity of using the cascaded system of equations (2.17a) to (2.17c) in place of the single equation (2.15) can be checked by recombining equations (2.17) to eliminate the intermediate wave fields P' and P'' and then using the identity (2.16). It should also be noted that the cascaded formulation of the extrapolation system does not introduce any new approximations or error terms in the case of propagation within a homogeneous medium. In addition, for laterally varying media, the cascaded formulation is of the same order of accuracy as the original fourth-order system. The error in this case resulting from the non-commutativity of the operators in equation (2.16) when the media varies as a function of x.

2.2.3 Dipfiltering

As shown earlier, the extrapolation operators derived from the continued fractions expansion can be made to match the exact dispersion relation quite well for ${K_x}^2 < 1$. However, in the evanescent region of k_z [i.e., ${K_x}^2 > 1$] these operators do a very poor job in matching the exact operator. In fact, as discussed previously in section 1.3.5, the operators can produce significant artifacts from energy propagating in the evanescent zone. These effects are illustrated in the left panel of Figure 2.3 which shows the numerical point response of the 80° operator presented in the previous section. In this example, the source is located at ($x = 0$, $z = 0$) and the proper response for this projection would be a quarter circle. The cusp-like arrivals along the x-axis are due to energy in the region ${K_x}^2 > 1$.

In order to eliminate these artifacts, we can apply a dipfilter of the form of equation (1.35) to the wave field at each extrapolation step. Implementation of this filter in the spatial domain is described in Appendix B.

As an example of using this filter, we have recalculated the point response applying equation (1.35) with $n = 8$ and $\epsilon = 0.01$ at each depth step. The result is shown in the right panel of Figure 2.3. Notice that virtually all of the energy in the evanescent zone has been eliminated, while energy in the region ${K_x}^2 < 1$ has

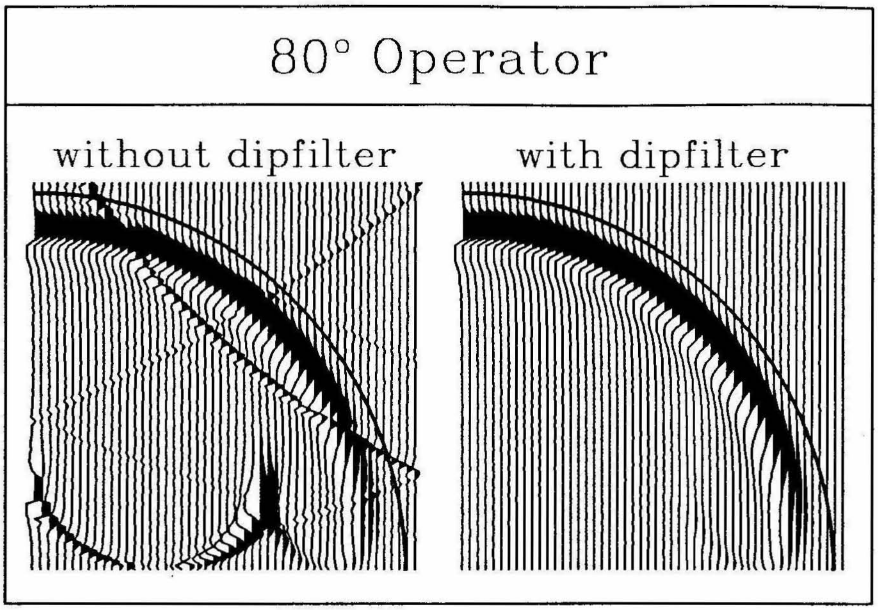

Figure 2.3. Time-slice in the xz plane showing the point response of the fourth-order extrapolation system. The left panel shows the calculation performed with no filtering. Proper response for this projection is a quarter-circle as denoted by the heavy curve. The secondary cusp-like waveforms along the x-axis are due to energy propagating in the region ${K_x}^2 > 1$. Sloping arrival cutting diagonally across the section is an artifact created by wrap-around in the time domain. This effect is caused by the limited frequency band-width used in the calculations. In the right panel we show the same calculation as before except the dipfilter operator has been applied at each extrapolation step. Energy in the evanescent zone is significantly reduced in this calculation and the wrap-around artifact has been eliminated completely.

not been significantly affected.

2.2.4 Absorbing boundary condition

In order to reduce artificial edge reflections, we want to match the interior solution as closely as possible at the boundaries of the system. As shown in Appendix C, each of the operations in equations (2.17a) and (2.17b) can be described by a pseudo dispersion relation of the form

$$k_{\tau_j} = -\frac{2\delta_j}{\Delta\tau_j}\left(\gamma_j + {K_x}^2\right)^{-1}. \tag{2.18}$$

Here $x_j = \gamma_j + i\delta_j$, where $x_j = x_0, x_1$ for equations (2.17a) and (2.17b), respectively and τ_j is a dummy varible which corresponds to a pseudo-depth axis. For the boundaries we must define a dispersion relation which is a good approximation to equation (2.18). However, by using tridiagonal systems for the interior solution, we are restricted to using a two-point side boundary condition. This means that the boundary dispersion relation must be linear in K_x. The most general form of a relation fitting this criteria is a hyperbola given by

$$k_{\tau_j} = -\frac{2\delta_j}{\Delta\tau_j}\left[\frac{1 - c_0 K_x}{c_2 - c_1 K_x}\right] \tag{2.19}$$

where

$$c_0 = \frac{(K_2 - K_1)(K_2 - K_0)(K_1 - K_0)}{\left[K_0^3(K_2 - K_1) + K_2^3(K_1 - K_0) - K_1^3(K_2 - K_0)\right]},$$

$$c_1 = -(K_1 + K_0) + \frac{c_0}{(K_1 - K_0)}\left[K_1(1 + \gamma_j K_1^2) - K_0(1 + \gamma_j K_0^2)\right],$$

$$c_2 = c_1 K_0 + (1 - c_0 K_0)(1 + \gamma_j K_0^2)$$

and $K_x = K_0$, K_1, and K_2 are points at which the hyperbola matches equation (2.18) exactly. This is similar in form to the B3 boundary condition of Clayton and Engquist (1980). For the right side boundary (positive x direction) K_0, K_1, and K_2 should be positive and for the left side boundary (negative x direction) K_0, K_1, and K_2 should be negative. Recalling that $K_x = \sin\theta$, where θ is the angle of propagation with respect to the z-axis (Claerbout, 1985a, p. 17), we want to choose K_0, K_1, and K_2 so that equation (2.19) matches equation (2.18) best for the range of angles at which most of the energy is propagating, such as the direct outgoing wave from the source.

The effectiveness of the absorbing boundary condition is demonstrated in Figure 2.4. This figure shows a series of time-slice panels for a model with a point source located within a homogeneous medium. On the left boundary of the calculation, we have imposed a zero-slope condition (reflection coefficient = 1) and on the right, we have used the absorbing condition described above with $K_0 = 0$, $K_1 = 0.5$ and $K_2 = 0.9$. These values correspond to propagation angles of $\theta = 0°$ (grazing incidence), 30° and 65°, respectively. From this fiqure, it is clear that the absorbing boundary condition works very well for a wide range of incidence angles.

2.3 Conclusions

The wide angle extrapolation technique we have described extends the validity of the paraxial method to propagation angles approaching 80°. In this formulation, solutions to high-order extrapolation equations are obtained by combining a

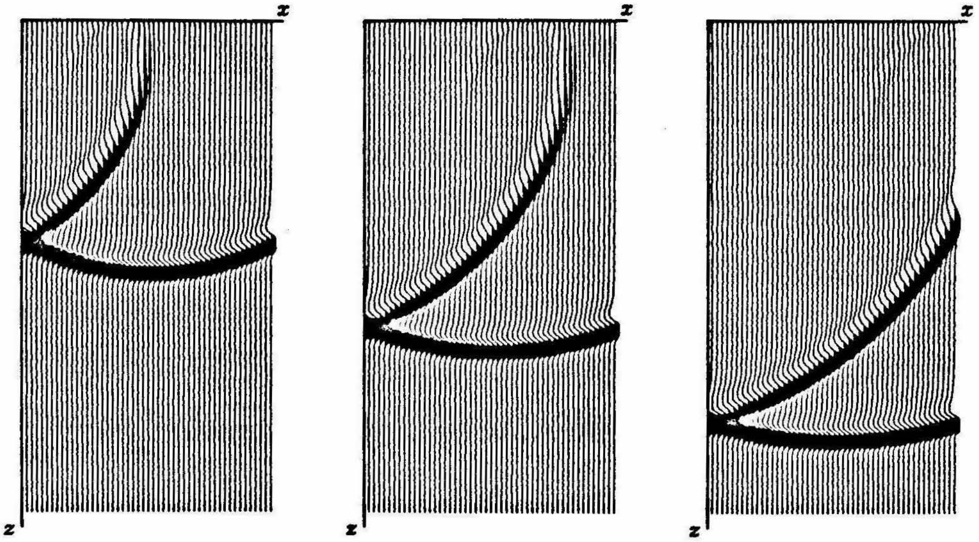

Figure 2.4. Series of time-slices in the xz plane illustrating the effectiveness of the absorbing boundary condition. The source is located at $z = 0$ midway along the x-axis. The left boundary in this calculation is zero-slope (reflection coefficient $= 1$) and the right boundary is absorbing.

sequence of second-order systems which are then solved in series. The advantages of using this approach are that the second-order systems are easy to implement and they can always be cast in a stable manner.

Since the paraxial operators are cast in the temporal frequency domain it is a straightforward task to apply the method to problems containing laterally heterogeneous structure. The simplest approach is to let $v \rightarrow v(x)$ in the extrapolation equations (2.17). As discussed in section 1.3 for the second-order extrapolation system, the main question with this heterogeneous formulation is how well the operator matches the correct reflection and transmission coefficients as the wave field is propagated across a lateral boundary between different types of media. However, addressing this concern is much more difficult here with the fourth-order system than it was with the second-order system because the issue of operator ordering is more complex. Not only are we concerned with the ordering of the operator D_x^2 and the velocity term $v(x)$, but, perhaps more importantly, is the question of how the operator D_x^4 should be represented? Possible choices are $\frac{v^2}{\omega^2}\partial_{xx}\frac{v^2}{\omega^2}\partial_{xx}$, $\frac{v^4}{\omega^4}\partial_{xxxx}$ or $\partial_{xx}\frac{v^4}{\omega^4}\partial_{xx}$. Unfortunately, each of these choices gives a different numerical value for the internal reflection coefficient. Since the full wave equation does not contain any fourth-order terms we have little guidance as to the most appropriate choice.

Another area of concern with the high-order extrapolation system is the issue of implementation cost. The 2-D fourth-order system presented here (including dipfilter) requires the solution of ten tridiagonal matrix systems at each extrapolation step and is accurate to about 80°. The 2-D second-order system presented in Chapter 1 (including dipfilter) only requires the solution of three tridiagonal matrix systems at each depth step and has an accuracy range of about 60°. The tradeoff here is an increase in implementation cost of greater than a factor of three to obtain an increase in angular accuracy of roughly one-third. For the 3-D case, the situation is even worse because the fourth-order extrapolation system would require the application of a fourth-order phase correction filter to reduce azimuthal anisotropy. This, in itself, is not very costly; however, in order to ensure stability, the fourth-order filter requires eighth-order damping terms in contrast to the second-order system which requires only fourth-order damping terms. The net result is that the increased implementation cost is probably not justified in order to obtain only a modest improvement in angular accuracy for the extrapolation system.

The biggest cost in implementing the fourth-order system is the application of the high-order dipfilter. By incorporating the dipfiltering process within the extrapolation system, the entire extrapolation procedure can be made much more efficient; unfortunately, at this time, a straightforward formulation of this process for the higher-order systems has not been found. Future work should concentrate on developing this type of formulation as well as establishing a framework in which to analyze the accuracy and applicability of the higher-order extrapolation systems to problems with laterally varying media.

Chapter 3

Elastic Wave Field Simulation Using Paraxial Extrapolators

3.1 Introduction

The wave propagation techniques discussed in the previous chapters are somewhat limited in that they are appropriate only for acoustic (i.e., fluid) media. The acoustic system is very useful, though, because it provides a good approximation for many seismological problems, e.g., modeling of direct P-waves or SH-waves. However, in order to more fully model realistic earth problems, we need to consider the complete elastic description of the media.

Modeling elastic wave propagation in generally heterogeneous media is best accomplished using a finite-difference formulation of the problem. In this manner, arbitrary media variations are easily represented on a discrete grid of points. Many formulations of this technique in the time-domain have been presented for the two-dimensional (2-D) case (e.g., Kelly et al., 1976; Kosloff et al., 1984; Vireux, 1986). The three-dimensional (3-D) case is more challenging, not only because of the increased computational requirements, but also due to the need for a large block of accessible computer memory. The use of supercomputers (Reshef et al., 1988b) or massively parallel computers (Peter Mora, personal communication) can reduce the computational demands, yet these methods are still restricted by the availability of accessible memory.

Following the same approach used in Chapter 1 for the acoustic case, our goal is to derive a paraxial extrapolation system which is appropriate for elastic wave field simulation. The primary advantage in formulating the problem in this manner is that active computer memory requirements are reduced significantly compared to the complete methods. Preliminary work on this approach was performed by Clayton (1981) who investigated the choice of variables for the elastic formulation. In his work, three sets of variables were considered: displacements, potentials and a mixed set containing combinations of displacements and/or stresses. Displacements were found to be impractical because the system lacks a framework in which higher-order propagation operators can be developed. The use of potentials remedied this problem, but presented other difficulties in describing the scattering effects for heterogeneous media. A practical scheme to implement the mixed set of variables was derived, but this technique proved to be unstable for heterogeneous models.

In the work presented here, we have chosen to describe the elastic system in terms of potentials. In order to formulate reasonable expressions for the scattering terms we have parameterized the media variations in a manner similar to that of Kennett (1972). That is, the media consists of a primary homogeneous part plus a perturbation term to account for any heterogeneity. Assuming that the perturbations are small, we retain only first-order terms in the derivation of the scattering matrix. Doing this allows us to develop a concise, useable formulation of the elastic extrapolation system for the 2-D case. Unfortunately, following this same approach for the 3-D system does not provide useful results.

In the sections that follow, we will first derive the 2-D elastic paraxial extrapolation system. This includes a discussion of the scattering terms as well as the discrete implementation of the resulting equations. Next, we outline the 3-D extrapolation system and describe some of the problems inherent to its implementation. Finally, we present some examples and comparisons for the 2-D formulation in order to illustrate the range of applicability of this method.

3.2 The 2-D P-SV extrapolation system

In this section the elastic extrapolation system is derived for a general isotropic 2-D medium. The derivation that follows is very similar to that performed for the acoustic system in Chapter 1.

3.2.1 Equations of motion

The equations of motion for a 2-D elastic medium are given by the following series of coupled first-order equations

$$\begin{aligned}
-\rho\omega^2 u_x &= \partial_x \tau_{xx} + \partial_z \tau_{xz} + f_x \\
-\rho\omega^2 u_z &= \partial_x \tau_{xz} + \partial_z \tau_{zz} + f_z \\
\tau_{xx} &= (\lambda + 2\mu)\partial_x u_x + \lambda \partial_z u_z \\
\tau_{zz} &= (\lambda + 2\mu)\partial_z u_z + \lambda \partial_x u_x \\
\tau_{xz} &= \mu(\partial_z u_x + \partial_x u_z).
\end{aligned} \tag{3.1}$$

In these equations, u_x, u_z are the displacement components, τ_{xx}, τ_{zz}, τ_{xz} are the stress components, f_x, f_z are the body force components, ρ is the density, λ and μ are Lame coefficients and ω is the frequency. As before, the symbols ∂_x and ∂_z are used as shorthand representations of the differential operators $\partial/\partial x$ and $\partial/\partial z$. Rearranging equations (3.1), we can write this system as a first-order extrapolation system given by

$$\partial_z \mathbf{r} = \mathbf{A}\mathbf{r} + \mathbf{f} \tag{3.2}$$

where $\mathbf{r} = (u_x, \tau_{zz}, u_z, \tau_{xz})^T$ represents the field variables, $\mathbf{f} = (-f_z, 0, -f_x, 0)^T$ is the source vector, and $\mathbf{A}$ is the matrix

$$\mathbf{A} = \begin{pmatrix} 0 & 0 & -\partial_x & \frac{1}{\mu} \\ 0 & 0 & -\rho\omega^2 & -\partial_x \\ -\lambda\gamma\partial_x & \gamma & 0 & 0 \\ -(\partial_x \epsilon \partial_x + \rho\omega^2) & -\partial_x \lambda\gamma & 0 & 0 \end{pmatrix} \tag{3.3}$$

with $\gamma = 1/(\lambda + 2\mu)$ and $\epsilon = 4\mu(\lambda + \mu)/(\lambda + 2\mu)$.

3.2.2 Decoupling the first-order system

Our goal now, is to form a new set of decoupled paraxial extrapolators from the system given by equation (3.2). This is more difficult here with the elastic case than it was before with the acoustic case because we are now dealing with two types of wave fields (i.e., P-waves and S-waves) which are inherently coupled in the presence of heterogeneous media.

In order to account for this added complexity, we must first rewrite equation (3.2) as

$$\partial_z \mathbf{r} = \mathbf{A}_0 \mathbf{r} + \delta \mathbf{A} \mathbf{r} + \mathbf{f} \tag{3.4}$$

where $\mathbf{A}(x,z) = \mathbf{A}_0(z) + \delta\mathbf{A}(x,z)$. That is, the media is parameterized by a primary part $\mathbf{A}_0$ which varies only as a function of z and a secondary part $\delta\mathbf{A}$ which depends on the variable x as well as z. Proceeding as we did before for the acoustic case, we can now decompose $\mathbf{A}_0$ into its eigenvalue and eigenvector representation. Doing this, we find

$$\mathbf{A}_0 = \mathbf{E}\mathbf{\Lambda}\mathbf{E}^{-1} \tag{3.5}$$

where

$$\mathbf{\Lambda} = \begin{pmatrix} i\phi_p & 0 & 0 & 0 \\ 0 & i\phi_s & 0 & 0 \\ 0 & 0 & -i\phi_p & 0 \\ 0 & 0 & 0 & -i\phi_s \end{pmatrix}, \tag{3.6}$$

$$\mathbf{E} = \begin{pmatrix} -\partial_x & -i\phi_s & -\partial_x & -i\phi_s \\ -\mu k^2 & 2i\phi_s\mu\partial_x & -\mu k^2 & 2i\phi_s\mu\partial_x \\ -i\phi_p & \partial_x & i\phi_p & -\partial_x \\ -2i\phi_p\mu\partial_x & -\mu k^2 & 2i\phi_p\mu\partial_x & \mu k^2 \end{pmatrix} \tag{3.7}$$

and

$$\mathbf{E}^{-1} = \frac{1}{2\rho\omega^2}\boldsymbol{\Lambda}^{-1}\begin{pmatrix} 2i\phi_p\mu\partial_x & i\phi_p & \mu k^2 & \partial_x \\ \mu k^2 & -\partial_x & -2i\phi_s\mu\partial_x & i\phi_s \\ -2i\phi_p\mu\partial_x & -i\phi_p & \mu k^2 & \partial_x \\ -\mu k^2 & \partial_x & -2i\phi_s\mu\partial_x & i\phi_s \end{pmatrix} \tag{3.8}$$

with

$$\phi_p = \left(\frac{\omega^2}{\alpha^2} + \partial_{xx}\right)^{1/2},$$

$$\phi_s = \left(\frac{\omega^2}{\beta^2} + \partial_{xx}\right)^{1/2},$$

$$k^2 = -\left(\frac{\omega^2}{\beta^2} + 2\partial_{xx}\right)$$

and the quantities $\alpha = [(\lambda + 2\mu)/\rho]^{1/2}$ and $\beta = [\mu/\rho]^{1/2}$ representing, respectively, the P- and S-wave velocities of the medium. Note that since $\mathbf{A}_0$ is not a function of x, this decomposition is exact. We now define a new solution vector

$$\mathbf{p} = \begin{pmatrix} P_f \\ S_f \\ P_b \\ S_b \end{pmatrix} = \mathbf{E}^{-1}\mathbf{r} \tag{3.9}$$

where $\Phi = P_f + P_b$ and $\Psi = (0, S_f - S_b)^T$ are P- and S-wave potentials such that

$$\mathbf{u} = -\nabla\Phi + \nabla \times \Psi. \tag{3.10}$$

The subscripts f and b refer to the forward-scattered and backscattered portion of each potential and, as before, we have chosen the forward-scattered potential to represent energy which is propagating in the positive z direction. Using equations (3.5) and (3.7) in equation (3.4) transforms the system into

$$\partial_z\mathbf{E}\mathbf{p} = \mathbf{E}\boldsymbol{\Lambda}\mathbf{p} + \mathbf{E}\delta\mathbf{A}\mathbf{p} + \mathbf{f}.$$

Differentiating through the left side, premultiplying by $\mathbf{E}^{-1}$, and defining

$$\mathbf{f}_{_E} = \mathbf{E}^{-1}\mathbf{f} \quad \text{and} \quad \mathbf{S} = \mathbf{E}^{-1}\delta\mathbf{A}\mathbf{E} - \mathbf{E}^{-1}\mathbf{E}_z, \tag{3.11}$$

where $\mathbf{E}_z = \partial\mathbf{E}/\partial z$, we obtain

$$\partial_z\mathbf{p} = \mathbf{\Lambda}\mathbf{p} + \mathbf{S}\mathbf{p} + \mathbf{f}_{_E} \tag{3.12}$$

as the 2-D elastic extrapolation system.

The advantage of writing the elastic system in the form of equation (3.12) is that solutions are built-up by modeling a set of scalar potentials which can then be recombined to obtain the full vector wave field. Using scalar wave fields is attractive because the propagation aspects of the forward- and backscattered P- and S-waves of the elastic system are decoupled and can be modeled with a simple set of equations. The coupling between these modes is accommodated through the scattering matrix $\mathbf{S}$, which is only non-zero at points where the medium changes. As before, we will treat the scattering as if it were a pseudo source.

3.3 The propagation matrix

If we neglect for the moment the scattering contribution (i.e., assume a homogeneous medium), and the real sources of equation (12), then the problem reduces to solving the decoupled system

$$\partial_z \begin{pmatrix} P_f \\ P_b \\ S_f \\ S_b \end{pmatrix} = \begin{pmatrix} i\phi_p & 0 & 0 & 0 \\ 0 & i\phi_s & 0 & 0 \\ 0 & 0 & -i\phi_p & 0 \\ 0 & 0 & 0 & -i\phi_s \end{pmatrix} \begin{pmatrix} P_f \\ P_b \\ S_f \\ S_b \end{pmatrix}. \tag{3.13}$$

This system represents a set of scalar wave equations, each of which is of the same form as the acoustic extrapolation system discussed in Chapter 1.

As derived in the previous section, the propagation operators ϕ_p and ϕ_s are homogeneous in the sense that they do not vary as a function of x. In the next section, we will relax this restriction; however, doing this will not change the form of equation (3.13) (i.e., the propagation system will remain decoupled).

Solutions for the set of equations (3.13) (in either the homogeneous or the heterogeneous formulation) are easily obtained by first using a paraxial approximation for the operators ϕ_p and ϕ_s and then implementing the resulting difference equations on a finite numerical grid. The details of this technique are given in section 1.3.

3.4 The scattering matrix

3.4.1 Parameterization of the scattering terms

The scattering effects for elastic waves can be quite complicated. Not only are we concerned with the coupling between forward- and backscattered waves of a particular type (i.e. P or S), but we must also account for the conversion of energy between these two modes as well. The incorporation of these scattering effects within the extrapolation system [equation (3.12)] is accomplished through the scattering matrix **S**. In its explicit form, the scattering matrix is given by

$$\mathrm{S} = \frac{1}{2} \begin{pmatrix} \mathrm{S}_1 - \mathrm{S}_2 \end{pmatrix} \tag{3.14}$$

where $\mathbf{S}_1 = 2\mathbf{E}^{-1}\delta\mathbf{A}\mathbf{E}$ and $\mathbf{S}_2 = 2\mathbf{E}^{-1}\mathbf{E}_z$. Notice that $\mathbf{S}_1$ is nonzero only when the media varies as a function of x (through the term $\delta\mathbf{A}$) and $\mathbf{S}_2$ is nonzero only when the media varies as a function of z (through the term $\mathbf{E}_z$). In order to derive suitable expressions for these terms we must make some simplifications. First, let us consider the matrix $\mathbf{S}_1$.

The general form of $\mathbf{S}_1$ can be written as

$$\mathbf{S}_1 = \begin{pmatrix} \mathbf{L}_{ff} & \mathbf{L}_{fb} \\ \mathbf{L}_{bf} & \mathbf{L}_{bb} \end{pmatrix}$$

where $\mathbf{L}_{ff}$, $\mathbf{L}_{fb}$, $\mathbf{L}_{bf}$ and $\mathbf{L}_{bb}$ are 2×2 sub-matrices. The subscripts f and b refer to the types of waves (forward- and backscattered) which are involved in the scattering. That is, the term $\mathbf{L}_{ff}$ couples forward-scattered energy with forward-scattered energy, the term $\mathbf{L}_{fb}$ couples forward-scattered energy with backscattered energy (vice versa for the term $\mathbf{L}_{bf}$) and the term $\mathbf{L}_{bb}$ couples backscattered energy with backscattered energy. In addition, note that $\mathbf{L}_{ff} = -\mathbf{L}_{bb}$ and $\mathbf{L}_{fb} = -\mathbf{L}_{bf}$.

To obtain a better understanding of the relative importance of these scattering terms, consider the following. In the high frequency limit, we expect that a forward-scattered wave propagating through a media which varies only as a function of x would produce only forward-scattered waves and that no backscattered waves would be present. This idea is illustrated qualitatively in Figure 3.1. As it turns out, this concept is valid over a wide range of frequencies and can be verified numerically. Based on this, we will neglect the terms $\mathbf{L}_{fb}$ and $\mathbf{L}_{bf}$ from $\mathbf{S}_1$ and by

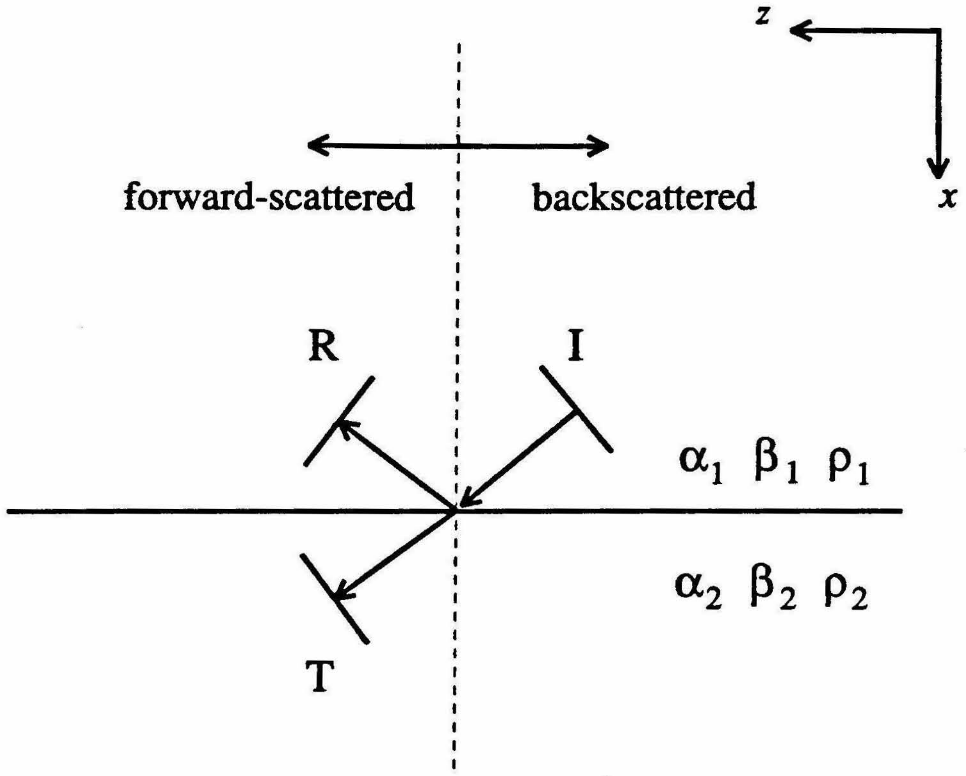

Figure 3.1. Scattering effects from a horzontal interface. A high frequency, locally planar wave front (I) is incident on a horizontal interface resulting in a reflected wave (R) and a transmitted wave (T). In this case, the incident, transmitted and reflected waves are all forward-scattered relative to the extrapolation direction (z-axis).

setting $\mathbf{L} = \mathbf{L}_{ff} = -\mathbf{L}_{bb}$ we have

$$\mathbf{S}_1 = \begin{pmatrix} \mathbf{L} & 0 \\ 0 & -\mathbf{L} \end{pmatrix} . \tag{3.15}$$

In order to calculate the individual elements of $\mathbf{L}$ we must first specify the matrix $\delta\mathbf{A}$. To do this, we will parameterize the media in the following manner

$$\begin{aligned} \rho(x,z) &= \rho_0(z) + \delta\rho(x,z) \\ \lambda(x,z) &= \lambda_0(z) + \delta\lambda(x,z) \\ \mu(x,z) &= \mu_0(z) + \delta\mu(x,z) \end{aligned} \tag{3.16a}$$

where we will assume that

$$|\rho_0| \gg |\delta\rho|, \quad |\lambda_0| \gg |\delta\lambda| \quad \text{and} \quad |\mu_0| \gg |\delta\mu|. \tag{3.16b}$$

This assumption requires that the lateral variations of the media be small in comparison to the primary values. The implications of this restriction will be discussed later by considering some numerical examples. If we then neglect terms of second- and higher order in the construction of $\delta\mathbf{A}$, we obtain the following

$$\delta\mathbf{A} = \begin{pmatrix} 0 & 0 & 0 & \delta\mu/\mu_0^2 \\ 0 & 0 & -\delta\rho\omega^2 & 0 \\ -\delta\sigma\partial_x & \delta\gamma & 0 & 0 \\ -(\partial_x\delta\epsilon\partial_x + \delta\rho\omega^2) & -\partial_x\delta\sigma & 0 & 0 \end{pmatrix} \tag{3.17}$$

where

$$\delta\gamma = (\delta\lambda + 2\delta\mu)\gamma_0^2$$

$$\delta\sigma = 2(\mu_0\delta\lambda - \lambda_0\delta\mu)\gamma_0^2$$

$$\delta\epsilon = 4[\mu_0^2\delta\lambda + (\lambda_0^2 + 2\lambda_0\mu_0 + 2\mu_0^2)\delta\mu]\gamma_0^2$$

and

$$\gamma_0 = 1/(\lambda_0 + 2\mu_0).$$

Now using equations (3.7), (3.8), (3.14) and (3.17) along with the plane wave approximations $\phi_p \approx \frac{\omega}{\alpha_0}$ and $\phi_s \approx \frac{\omega}{\beta_0}$ and again neglecting terms of second- and higher order, we obtain for the matrix $\mathbf{L}$

$$\mathbf{L} = \begin{pmatrix} l_1 & l_2 \\ l_3 & l_4 \end{pmatrix} \tag{3.18}$$

where

$$\begin{aligned} l_1 &= -i\frac{\alpha_0}{\omega}\frac{\rho_x}{\rho_0}\partial_x + i\frac{\omega}{\alpha_0}\left(\frac{\delta\rho}{\rho_0} - \frac{\delta\lambda + 2\delta\mu}{\lambda_0 + 2\mu_0}\right) \\ l_2 &= -2\frac{\mu_x}{\mu_0} + \frac{\alpha_0}{\beta_0}\frac{\rho_x}{\rho_0} \\ l_3 &= 2\frac{\beta_0^2}{\alpha_0^2}\frac{\mu_x}{\mu_0} - \frac{\beta_0}{\alpha_0}\frac{\rho_x}{\rho_0} \\ l_4 &= -i\frac{\beta_0}{\omega}\frac{\rho_x}{\rho_0}\partial_x + i\frac{\omega}{\beta_0}\left(\frac{\delta\rho}{\rho_0} - \frac{\delta\mu}{\mu_0}\right). \end{aligned} \tag{3.19}$$

In deriving the above relations we have also made use of the following

$$\frac{\partial}{\partial x}\delta\rho = \frac{\partial}{\partial x}\rho \equiv \rho_x \qquad \text{and} \qquad \frac{\partial}{\partial x}\delta\mu = \frac{\partial}{\partial x}\mu \equiv \mu_x .$$

In the equations for l_1 and l_4 listed in (3.19), the second term in each corresponds to a perturbation in velocity which can be expressed as

$$\left(\frac{\delta\rho}{\rho_0} - \frac{\delta\lambda + 2\delta\mu}{\lambda_0 + 2\mu_0}\right) = -2\frac{\delta\alpha}{\alpha_0} \tag{3.20a}$$

and

$$\left(\frac{\delta\rho}{\rho_0} - \frac{\delta\mu}{\mu_0}\right) = -2\frac{\delta\beta}{\beta_0} \tag{3.20b}$$

(Aki and Richards, 1980, p. 731). Using this, these equations can be rewritten as

$$l_1 = -i\frac{\alpha_0}{\omega}\frac{\rho_x}{\rho_0}\partial_x - 2\frac{\omega}{\alpha_0}\frac{\delta\alpha}{\alpha_0} \tag{3.21a}$$

and

$$l_4 = -i\frac{\beta_0}{\omega}\frac{\rho_x}{\rho_0}\partial_x - 2\frac{\omega}{\beta_0}\frac{\delta\beta}{\beta_0} \tag{3.21b}$$

Since these terms occur along the diagonal elements of $\mathbf{S}_1$, they can be absorbed into the propagation matrix $\mathbf{\Lambda}$ by letting the terms ϕ_p and ϕ_s vary as a function of x. These expressions are given by

$$\phi_p + \frac{1}{2}l_1 \rightarrow \phi_p(x) = \left(\frac{\omega^2}{\alpha^2} + \rho\,\partial_x\frac{1}{\rho}\partial_x\right)^{1/2} \tag{3.22a}$$

and

$$\phi_s + \frac{1}{2}l_4 \rightarrow \phi_s(x) = \left(\frac{\omega^2}{\beta^2} + \rho\,\partial_x\frac{1}{\rho}\partial_x\right)^{1/2}. \tag{3.22b}$$

These substitutions are accurate to first-order with respect to variations in the media parameters as a function of x (see appendix D).

Returning to the scattering terms given in equations (20), the expressions for l_2 and l_3 can be further simplified by replacing the subscripted media variables by their non-subscripted forms [e.g., $\rho_0(z) \rightarrow \rho(x,z)$]. This is consistent with the assumption that the scattering effects are only significant to first-order. The reason for doing this is that now the model can be described by one set of media parameters [e.g., $\rho(x,z)$, $\mu(x,z)$ and $\lambda(x,z)$] instead of specifying both the primary and perturbed values of these parameters for each point (x,z). The final form of the matrix $\mathbf{S}_1$ is then given by

$$\mathbf{S}_1 = \begin{pmatrix} 0 & l & 0 & 0 \\ -l\beta^2/\alpha^2 & 0 & 0 & 0 \\ 0 & 0 & 0 & -l \\ 0 & 0 & l\beta^2/\alpha^2 & 0 \end{pmatrix} \tag{3.23}$$

with

$$l = -2\frac{\mu_x}{\mu} + \frac{\alpha}{\beta}\frac{\rho_x}{\rho}.$$

Now let us consider the second scattering term, i.e., the matrix $\mathbf{S}_2$. As was done in the case of $\mathbf{S}_1$, the general form of $\mathbf{S}_2$ can be written as

$$\mathbf{S}_2 = \begin{pmatrix} \mathbf{M}_{ff} & \mathbf{M}_{fb} \\ \mathbf{M}_{bf} & \mathbf{M}_{bb} \end{pmatrix}$$

where $\mathbf{M}_{ff}$, $\mathbf{M}_{fb}$, $\mathbf{M}_{bf}$ and $\mathbf{M}_{bb}$ are 2×2 sub-matrices and, as before, the subscripts f and b refer to the types of waves which are involved in the scattering. In addition, note that in this case, $\mathbf{M}_{ff} = \mathbf{M}_{bb}$ and $\mathbf{M}_{fb} = \mathbf{M}_{bf}$.

Since $\mathbf{S}_2$ represents scattering due to media variations with respect to the extrapolation or z direction, we expect that the conversion between forward- and backscattered energy to be of significant importance and thus, we cannot neglect the terms $\mathbf{M}_{fb}$ and $\mathbf{M}_{bf}$ here as we did with $\mathbf{L}_{fb}$ and $\mathbf{L}_{bf}$ in the derivation of $\mathbf{S}_1$ (see Figure 3.2).

Writing $\mathbf{M}_1 = \mathbf{M}_{ff} = \mathbf{M}_{bb}$ and $\mathbf{M}_2 = \mathbf{M}_{fb} = \mathbf{M}_{bf}$, we can write $\mathbf{S}_2$ as

$$\mathbf{S}_2 = \begin{pmatrix} \mathbf{M}_1 & \mathbf{M}_2 \\ \mathbf{M}_2 & \mathbf{M}_1 \end{pmatrix}. \tag{3.24}$$

Now using equations (3.7), (3.8) and (3.14) along with the plane wave approximations $\phi_p \approx \dfrac{\omega}{\alpha_0}$ and $\phi_s \approx \dfrac{\omega}{\beta_0}$ and neglecting terms of second- and higher order, we obtain for $\mathbf{M}_1$ and $\mathbf{M}_2$

$$\mathbf{M}_1 = \begin{pmatrix} m_1 + n_1 & m_2 + n_2 \\ m_3 + n_3 & m_4 + n_4 \end{pmatrix} \qquad \text{and} \qquad \mathbf{M}_2 = \begin{pmatrix} m_1 - n_1 & m_2 - n_2 \\ m_3 - n_3 & m_4 - n_4 \end{pmatrix} \tag{3.25}$$

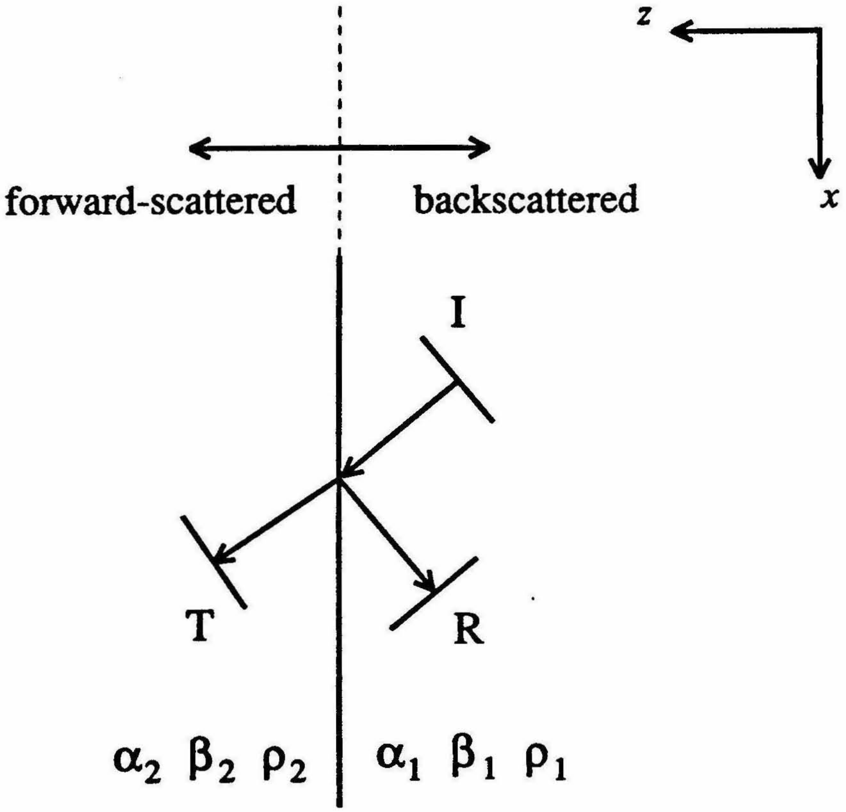

Figure 3.2. Scattering effects from a vertical interface. A high frequency, locally planar wave front (I) is incident on a vertical interface resulting in a reflected wave (R) and a transmitted wave (T). In this case, the incident and transmitted waves are forward-scattered relative to the extrapolation direction (z-axis), but the reflected wave is backscattered.

where

$$\begin{aligned}
m_1 &= \frac{\rho_z}{\rho} & n_1 &= -\frac{\alpha_z}{\alpha} \\
m_2 &= 2i\frac{\beta}{\omega}\frac{\mu_z}{\mu}\partial_x & n_2 &= -i\frac{\alpha}{\omega}\frac{\rho_z}{\rho}\partial_x \\
m_3 &= -i\frac{\beta}{\omega}\frac{\rho_z}{\rho}\partial_x & n_3 &= -2i\frac{\beta}{\alpha}\frac{\beta}{\omega}\frac{\mu_z}{\mu}\partial_x \\
m_4 &= -\frac{\beta_z}{\beta} & n_4 &= \frac{\rho_z}{\rho}.
\end{aligned} \tag{3.26}$$

3.4.2 Discrete Implementation

Returning to equation (3.12) and using equations (3.23) and (3.24) for the scattering terms, we can write the extrapolation system (neglecting the source term) as the following set of coupled differential equations

$$\partial_z P_f = i\phi_p P_f + \frac{\kappa}{\Delta z}\left(s_{11}P_f + s_{12}S_f + s_{13}P_b + s_{14}S_b\right) \tag{3.27a}$$

$$\partial_z S_f = i\phi_s S_f + \frac{\kappa}{\Delta z}\left(s_{21}P_f + s_{22}S_f + s_{23}P_b + s_{24}S_b\right) \tag{3.27b}$$

$$\partial_z P_b = -i\phi_p P_b + \frac{\kappa}{\Delta z}\left(s_{31}P_f + s_{32}S_f + s_{33}P_b + s_{34}S_b\right) \tag{3.27c}$$

$$\partial_z S_b = -i\phi_s S_b + \frac{\kappa}{\Delta z}\left(s_{41}P_f + s_{42}S_f + s_{43}P_b + s_{44}S_b\right) \tag{3.27d}$$

where $\kappa = \Delta z/2$ and the s_{ij} are the elements of the matrix $\mathbf{S}_1 - \mathbf{S}_2$. Discretizing the z-axis and writing these as a set of coupled difference equations centered at the depth step $z_{n+\frac{1}{2}} = (n+\frac{1}{2})\Delta z$, we have

$$\begin{aligned}
P_f^{n+1} - P_f^n = i\theta_p(P_f^{n+1} + P_f^n) & \\
+ \frac{1}{2}\kappa\left(s_{11}(P_f^{n+1} + P_f^n) + s_{12}(S_f^{n+1} + S_f^n)\right) & \\
+ \frac{1}{2}\kappa\left(s_{13}(P_b^{n+1} + P_b^n) + s_{14}(S_b^{n+1} + S_b^n)\right) &
\end{aligned} \tag{3.28a}$$

$$\begin{aligned}S_f^{n+1} - S_f^n = i\theta_s(S_f^{n+1} + S_f^n) \\ + \frac{1}{2}\kappa \left(s_{21}(P_f^{n+1} + P_f^n) + s_{22}(S_f^{n+1} + S_f^n) \right) \\ + \frac{1}{2}\kappa \left(s_{23}(P_b^{n+1} + P_b^n) + s_{24}(S_b^{n+1} + S_b^n) \right)\end{aligned} \tag{3.28b}$$

$$\begin{aligned}P_b^{n+1} - P_b^n = -i\theta_p(P_b^{n+1} + P_b^n) \\ + \frac{1}{2}\kappa \left(s_{31}(P_f^{n+1} + P_f^n) + s_{32}(S_f^{n+1} + S_f^n) \right) \\ + \frac{1}{2}\kappa \left(s_{33}(P_b^{n+1} + P_b^n) + s_{34}(S_b^{n+1} + S_b^n) \right)\end{aligned} \tag{3.28c}$$

$$\begin{aligned}S_b^{n+1} - S_b^n = -i\theta_s(S_b^{n+1} + S_b^n) \\ + \frac{1}{2}\kappa \left(s_{41}(P_f^{n+1} + P_f^n) + s_{42}(S_f^{n+1} + S_f^n) \right) \\ + \frac{1}{2}\kappa \left(s_{43}(P_b^{n+1} + P_b^n) + s_{44}(S_b^{n+1} + S_b^n) \right)\end{aligned} \tag{3.28d}$$

where $\theta_p = \phi_p \Delta z/2$ and $\theta_s = \phi_s \Delta z/2$. Given that there are only incident forward-scattered P- and S-wave fields, denoted by P_f^n and S_f^n respectively, and no incident backscattered wave fields (i.e., $P_b^{n+1} = S_b^{n+1} = 0$), then we can solve for the unknown fields P_f^{n+1}, S_f^{n+1}, P_b^n and S_b^n. These fields are given by

$$\begin{aligned}P_f^{n+1} &= f_1 P' + f_2 S' \\ S_f^{n+1} &= f_3 P' + f_4 S' \\ P_b^n &= f_5 P' + f_6 S' \\ S_b^n &= f_7 P' + f_8 S'\end{aligned} \tag{3.29}$$

where

$$\begin{aligned}
f_1 &= 1 - \frac{\kappa}{(1+\zeta_p^2)}(m_1+n_1) & f_2 &= \frac{\kappa(l_2-m_2-n_2)}{(1-i\zeta_p)(1+i\zeta_s)} \\
f_3 &= \frac{\kappa(l_3-m_3-n_3)}{(1-i\zeta_s)(1+i\zeta_p)} & f_4 &= 1 - \frac{\kappa}{(1+\zeta_s^2)}(m_4+n_4) \\
f_5 &= \frac{\kappa}{(1+\zeta_p^2)}(m_1-n_1) & f_6 &= \frac{\kappa(m_2-n_2)}{(1-i\zeta_p)(1+i\zeta_s)} \\
f_7 &= \frac{\kappa(m_3-n_3)}{(1-i\zeta_s)(1+i\zeta_p)} & f_8 &= \frac{\kappa}{(1+\zeta_s^2)}(m_4-n_4)
\end{aligned} \tag{3.30}$$

and

$$\begin{aligned}
P' &= \frac{(1+i\theta_p)}{(1-i\theta_p)}P_f^n \\
S' &= \frac{(1+i\theta_s)}{(1-i\theta_s)}S_f^n.
\end{aligned} \tag{3.31}$$

In deriving these equations we have again neglected terms of second- and higher order in regards to their effects on scattering. Thus, we have the additional terms, $\zeta_p = \omega\Delta z/(2\alpha)$ and $\zeta_s = \omega\Delta z/(2\beta)$ which are the plane wave approximations to θ_p and θ_s, respectively.

Notice that equations (3.31) are simply the discrete representation of the first two equations of the propagation system (3.12) and thus P' and S' can be calculated using the paraxial technique given in section 1.3. Once P' and S' are known, then $P_f^{n+1}, S_f^{n+1}, P_b^n$ and S_b^n can be obtained from equations (3.29) and (3.30).

The approximations made in deriving the scattering terms presented in this section will certainly place some limitations on the applicability of this technique. It is difficult to analyze the accuracy of these terms directly because the exact expression for the scattering matrix **S** [equation (3.11)] does not have a simple analytic representation. In a later section, we will consider some numerical comparisons to obtain an idea as to the range of problems for which this method is appropriate.

3.5 The complete 3-D elastic extrapolation system

For completeness, we now present the 3-D elastic extrapolation system. The coupled first-order equations of motion are given by

$$\begin{aligned}
-\rho\omega^2 u_x &= \partial_x \tau_{xx} + \partial_y \tau_{xy} + \partial_z \tau_{xz} + f_x \\
-\rho\omega^2 u_y &= \partial_x \tau_{xy} + \partial_y \tau_{yy} + \partial_z \tau_{yz} + f_y \\
-\rho\omega^2 u_z &= \partial_x \tau_{xz} + \partial_y \tau_{yz} + \partial_z \tau_{zz} + f_z \\
\tau_{xx} &= (\lambda + 2\mu)\partial_x u_x + \lambda(\partial_y u_y + \partial_z u_z) \\
\tau_{yy} &= (\lambda + 2\mu)\partial_y u_y + \lambda(\partial_x u_x + \partial_z u_z) \qquad (3.32) \\
\tau_{zz} &= (\lambda + 2\mu)\partial_z u_z + \lambda(\partial_x u_x + \partial_y u_y) \\
\tau_{xy} &= \mu(\partial_y u_x + \partial_x u_y) \\
\tau_{xz} &= \mu(\partial_z u_x + \partial_x u_z) \\
\tau_{yz} &= \mu(\partial_z u_y + \partial_y u_z).
\end{aligned}$$

In these equations, u_x, u_y, u_z are the displacement components; τ_{xx}, τ_{yy}, τ_{zz}, τ_{xy}, τ_{xz}, τ_{yz} are the stress components; f_x, f_y, f_z are the body force components; ρ is the density; λ and μ are Lame coefficients and ω is the frequency. The symbols ∂_x, ∂_y and ∂_z are used as shorthand representations of the differential operators $\partial/\partial x$,

$\partial/\partial y$ and $\partial/\partial z$. Writing these equations as a first-order extrapolation system we have

$$\partial_z \mathbf{r} = \mathbf{A}\mathbf{r} + \mathbf{f} \tag{3.33}$$

where

$$\mathbf{r} = (u_x, \tau_{zz}, u_y, \tau_{yz}, u_z, \tau_{xz})^T$$

represents the field variables,

$$\mathbf{f} = (-f_z, 0, -f_y, 0, -f_x, 0)^T$$

is the source vector and $\mathbf{A}$ is the matrix

$$\mathbf{A} = \begin{pmatrix} \mathbf{M_N} & \mathbf{M_{A_1}} \\ \mathbf{M_{A_2}} & \mathbf{M_N} \end{pmatrix} \tag{3.34}$$

where $\mathbf{M_N}$ is a null 3×3 sub-matrix

$$\mathbf{M_N} = \begin{pmatrix} 0 & 0 & 0 \\ 0 & 0 & 0 \\ 0 & 0 & 0 \end{pmatrix},$$

$\mathbf{M_{A_1}}$ is the 3×3 sub-matrix

$$\mathbf{M_{A_1}} = \begin{pmatrix} -\partial_x & \dfrac{1}{\mu} & \\ -\partial_y & -\rho\omega^2 & -\partial_x \\ \dfrac{1}{\mu} & -\partial_y & 0 \end{pmatrix}$$

and $\mathbf{M_{A_2}}$ is the 3×3 sub-matrix

$$\mathbf{M_{A_2}} = \begin{pmatrix} -(\partial_y \eta \partial_x + \partial_x \mu \partial_y) & -\partial_y \lambda\gamma & -(\partial_y \epsilon \partial_y + \partial_x \mu \partial_x + \rho\omega^2) \\ -\lambda\gamma\partial_x & \gamma & -\lambda\gamma\partial_y \\ -(\partial_x \epsilon \partial_x + \partial_y \mu \partial_y + \rho\omega^2) & -\partial_x \lambda\gamma & -(\partial_x \eta \partial_y + \partial_y \mu \partial_x) \end{pmatrix}$$

with $\gamma = 1/(\lambda + 2\mu)$, $\eta = 2\lambda\mu/(\lambda + 2\mu)$ and $\epsilon = 4\mu(\lambda + \mu)/(\lambda + 2\mu)$.

Following the same sequence of steps performed in section 3.2.2 for the 2-D case, we can rewrite equation (3.33) as the decoupled extrapolation system

$$\partial_z \mathbf{p} = \mathbf{\Lambda p} + \mathbf{Sp} + \mathbf{f}_E \tag{3.35}$$

where

$$\mathbf{f}_E = \mathbf{E}^{-1}\mathbf{f} \quad \text{and} \quad \mathbf{S} = \mathbf{E}^{-1}\delta\mathbf{AE} - \mathbf{E}^{-1}\mathbf{E}_z. \tag{3.36}$$

Here, the eigenvalue matrix is

$$\mathbf{\Lambda} = \begin{pmatrix} \mathbf{M_\Lambda} & \mathbf{M_N} \\ \mathbf{M_N} & -\mathbf{M_\Lambda} \end{pmatrix} \tag{3.37a}$$

with $\mathbf{M_\Lambda}$ given by

$$\mathbf{M_\Lambda} = \begin{pmatrix} i\phi_p & 0 & 0 \\ 0 & i\phi_s & 0 \\ 0 & 0 & i\phi_s \end{pmatrix}, \tag{3.37b}$$

the eigenvector matrix is

$$\mathbf{E} = \begin{pmatrix} \mathbf{M_{E_1}} & \mathbf{M_{E_1}} \\ \mathbf{M_{E_2}} & -\mathbf{M_{E_2}} \end{pmatrix} \tag{3.38a}$$

with $\mathbf{M_{E_1}}$ and $\mathbf{M_{E_2}}$ given by

$$\mathbf{M_{E_1}} = \begin{pmatrix} -\partial_x & i\partial_x\phi_s & \partial_y \\ -\mu k^2 & -2i\mu\phi_s\nabla^2 & 0 \\ -\partial_y & i\partial_y\phi_s & -\partial_x \end{pmatrix} \tag{3.38b}$$

and

$$\mathbf{M_{E_2}} = \begin{pmatrix} -2i\mu\phi_p\partial_y & -\mu\partial_y k^2 & -i\mu\partial_x\phi_s \\ -i\phi_p & -\nabla^2 & 0 \\ -2i\mu\phi_p\partial_x & -\mu\partial_x k^2 & i\mu\partial_y\phi_s \end{pmatrix} \tag{3.38c}$$

and the inverse of the eigenvector matrix is

$$\mathbf{E}^{-1} = \frac{1}{2\rho\omega^2\nabla^2}\mathbf{\Lambda}^{-1}\begin{pmatrix} \mathbf{M}_{\mathbf{E}_3} & \mathbf{M}_{\mathbf{E}_4} \\ -\mathbf{M}_{\mathbf{E}_3} & \mathbf{M}_{\mathbf{E}_4} \end{pmatrix} \tag{3.39a}$$

with $\mathbf{M}_{\mathbf{E}_3}$ and $\mathbf{M}_{\mathbf{E}_4}$ given by

$$\mathbf{M}_{\mathbf{E}_3} = \begin{pmatrix} 2i\nabla^2\mu\phi_p\partial_x & i\nabla^2\phi_p & 2i\nabla^2\mu\phi_p\partial_y \\ \mu k^2\partial_x & \nabla^2 & \mu k^2\partial_y \\ i\rho\omega^2\phi_s\partial_y & 0 & -i\rho\omega^2\phi_s\partial_x \end{pmatrix} \tag{3.39b}$$

and

$$\mathbf{M}_{\mathbf{E}_4} = \begin{pmatrix} \partial_y\nabla^2 & \mu k^2\nabla^2 & \partial_x\nabla^2 \\ -i\partial_y\phi_s & -2i\mu\phi_s\nabla^2 & -i\partial_x\phi_s \\ -\frac{\omega^2}{\beta^2}\partial_x & 0 & \frac{\omega^2}{\beta^2}\partial_y \end{pmatrix} \tag{3.39c}$$

In addition, we have also used the following identities in the above equations

$$\begin{aligned} \phi_p &= \left(\frac{\omega^2}{\alpha^2} + \nabla^2\right)^{1/2}, \\ \phi_s &= \left(\frac{\omega^2}{\beta^2} + \nabla^2\right)^{1/2}, \\ k^2 &= -\left(\frac{\omega^2}{\beta^2} + 2\nabla^2\right), \\ \nabla^2 &= \partial_{xx} + \partial_{yy} \end{aligned}$$

where $\alpha = [(\lambda + 2\mu)/\rho]^{1/2}$ and $\beta = [\mu/\rho]^{1/2}$ represent, respectively, the *P*- and *S*-wave velocities of the medium.

The new solution vector is given by

$$\mathbf{p} = \begin{pmatrix} P_f \\ S_{f_1} \\ S_{f_2} \\ P_b \\ S_{b_1} \\ S_{b_2} \end{pmatrix} = \mathbf{E}^{-1}\mathbf{r} \tag{3.40}$$

where $\Phi = P_f + P_b$, $\mathbf{\Psi_1} = (0, 0, S_{f_1} - S_{b_1})$ and $\mathbf{\Psi_2} = (0, 0, S_{f_2} + S_{b_2})$ are P- and S-wave potentials such that

$$\mathbf{u} = -\nabla\Phi + \nabla \times \nabla \times \mathbf{\Psi_1} + \nabla \times \mathbf{\Psi_2}. \tag{3.41}$$

By convention, we have chosen the $\mathbf{\Psi_2}$ potential to represent the component of shear displacement which is contained entirely within the xy plane (i.e., the plane perpendicular to the extrapolation or z-axis). Thus for a model geometry in which the z-axis is pointing vertically downward and the structure varies only as a function of depth, this potential would represent pure SH motion and the $\mathbf{\Psi_1}$ potential would represent pure SV motion.

Deriving suitable expressions for the scattering terms in the 3-D system is quite complicated. One major difficulty is obtaining a rational expression for the term ∇^{-2} which appears in the matrix $\mathbf{E}^{-1}$. Another problem is determining the relative importance of the higher order scattering terms in regards to coupling between the various potentials. A third concern is the sheer mathematical complexity of these expressions and the difficulties involved with implementing them on a discrete grid. Because of these issues, we have not pursued the derivation of the 3-D system past this point.

3.6 Numerical Examples

In this section, we consider two examples which illustrate the accuracy and applicability of the paraxial extrapolator (PE) technique with respect to 2-D elastic wave propagation problems. For the purposes of comparison, we will check the results obtained with the PE method with those computed using a 2-D elastic time-domain finite-difference (FD) calculation. In both of the examples, we use an isotropic, explosive point source having a two-sided Gaussian time function with a half-width of 0.15 s.

3.6.1 Interface model

The first problem we consider consists of simple interface dividing two welded half-spaces (Figure 3.3). The media contrast between the two half-spaces is small (about six percent), thus we expect the PE method, as formulated in the preceding sections, to be applicable to this type of problem.

Figure 3.4 shows displacement seismograms recorded along the receiver array in this model for the two techniques. In general, the agreement between the two methods is good, particularly in regards to the timing of the various phases. A more detailed comparison at selected receiver locations is given in Figure 3.5. Note that since we have used an explosive source, the wave motions are most dominant along the radial direction. Comparing the two calculations, it is clear that the PE technique models the P wave very well, in both timing and amplitude. Since this phase is comprised primarily from energy traveling directly from the source and is not significantly affected by scattering at the interface, we expect the paraxial formulation to be very accurate in this situation.

The accuracy of the paraxial formulation with respect to scattering effects can be seen by examining the converted phases (i.e., the S wave and the Rayleigh

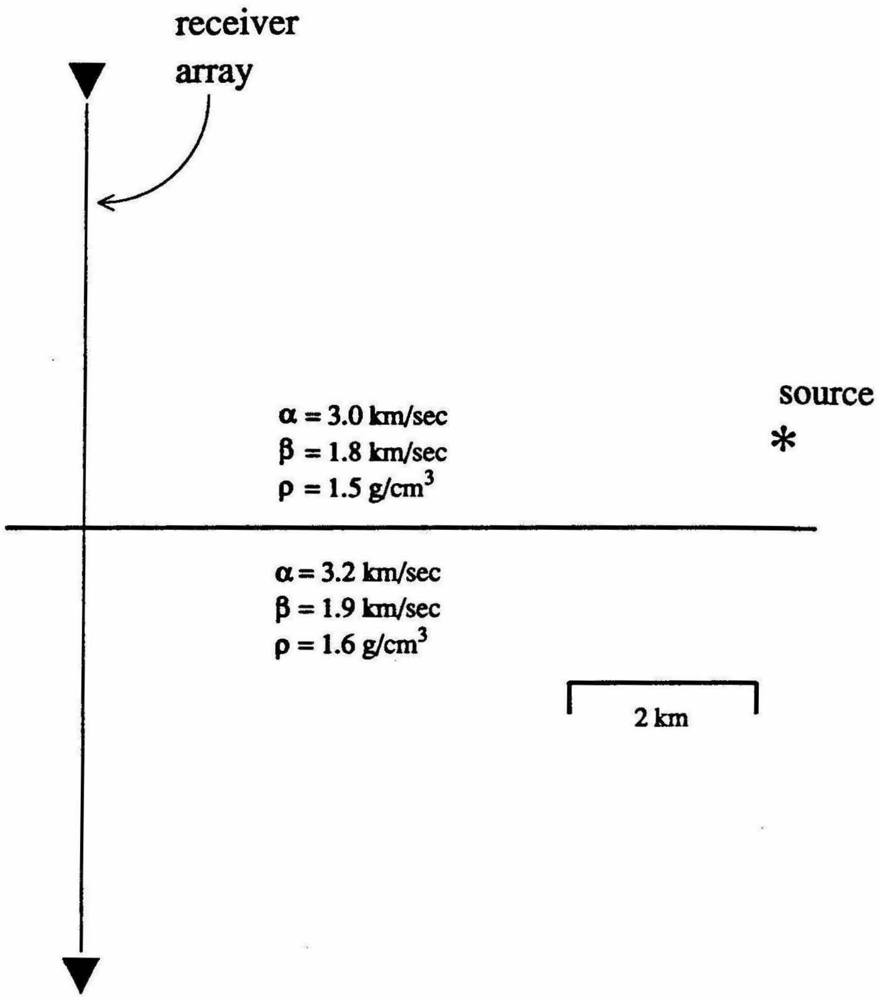

Figure 3.3. Model geometry and media parameters for a simple interface problem.

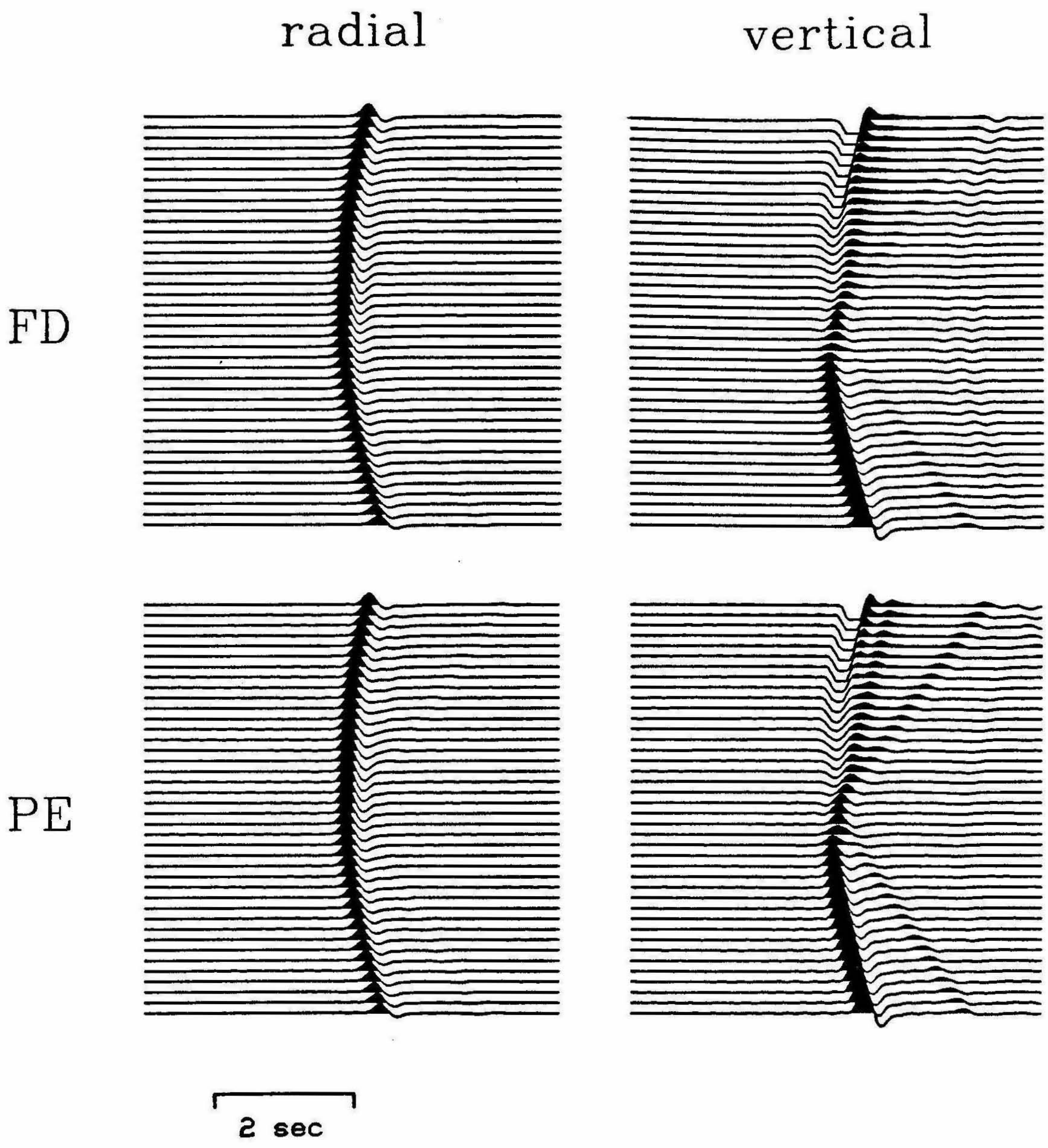

Figure 3.4. Comparison of displacement seismograms calculated for the interface model using conventional finite-difference (FD) and the paraxial extrapolator technique (PE). The solutions for each component have been normalized to the same maximum amplitude to reflect true amplitude variations along each section. In general, the agreement between the two calculations is good. See figure 3.5 for a more detailed comparison.

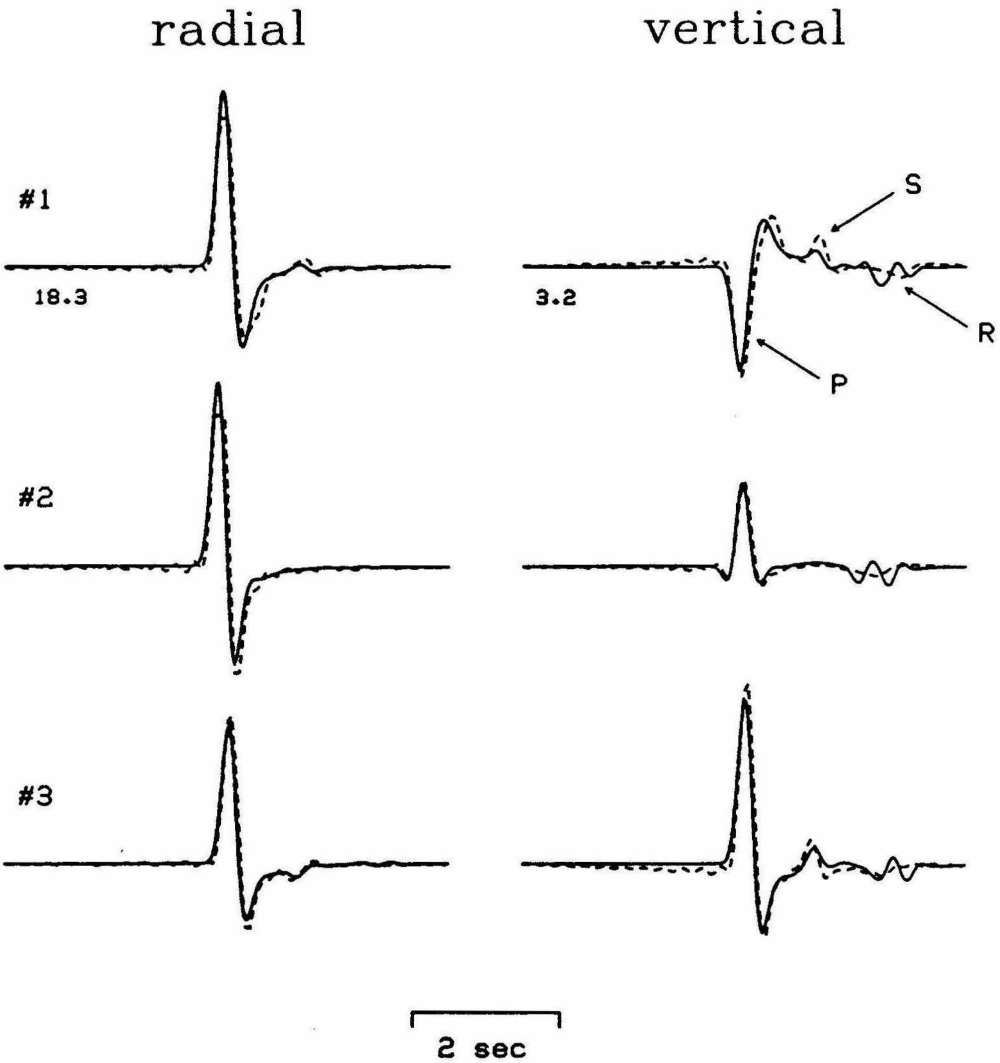

Figure 3.5. Detailed comparison of FD (solid line) and PE (dashed line) solutions for the interface model at selected locations within the receiver array. Locations #1 and #3 are positioned 2.5 km above and 2.5 km below the interface, respectively, and location #2 is just below the interface. Peak amplitudes for the FD calculation are given for the responses at location #1. All other traces for each component are scaled relative to this response. Note that each component has a different amplitude scale. The labeled arrivals on the vertical component at location #1 are as follows: *P* - direct *P* wave, *SV* - *SV* wave and *R* - Rayleigh wave.

wave) in this example. These phases are most evident on the vertical component as plotted in Figure 3.5. From this figure, we see that the converted S wave is modeled fairly well by the PE method. Although the amplitude of this phase is slightly overestimated, the timing is predicted quite well. Moving on to the Rayleigh wave, we find that the PE technique does a rather poor job in modeling this phase. Figure 3.5 shows an arrival computed by the PE method which matches the predicted arrival time of the Rayleigh wave; however, this phase does not match the amplitude or waveform of the Rayliegh wave as seen in the FD result.

Part of the difficulty in modeling this phase may result from the use of the dipfilter in the extrapolation process. As discussed in section 1.3.5, the use of the dipfilter is necessary to suppress artifacts propagating in the evanescent region of k_z; however, this filter also damps energy in the evanescent region of k_x; specifically, for imaginary wavenumbers k_x such that $\frac{\alpha^2}{\omega^2}k_x^2 > -1$ for P waves and $\frac{\beta^2}{\omega^2}k_x^2 > -1$ for S waves. Since the Rayleigh mode contains both evanescent P and evanescent S energy, some of the signal may be damped due to the application of this filter.

Another problem in modeling this phase may result from the neglect of the higher order terms in the scattering process. For this model, these terms are probably significant in order to accurately depict the sharp structural discontinuity. This high degree of accuracy may be important for the Rayliegh wave since this phase travels along the interface for a great distance in the extrapolation direction. Even though the error in the scattering contribution at each extrapolation step may be small, the accumulated error after many steps may be significant. The converted S wave does not suffer from this error accumulation since it samples only a short section of the interface before propagating away from the discontinuity.

3.6.2 Free surface model

The second example we consider is the free surface model shown in Figure 3.6. In order to correctly represent the free surface in the numerical simulations, one of the following approaches must be employed: (1) explicitly satisfying the free surface boundary condition (i.e., zero tangential stress and zero normal stress), or (2) allowing the media parameters to vary as they naturally would at the air-solid interface (e.g., $v \rightarrow 0$ and $\rho \rightarrow 0$).

Method (1) is the approach that is commonly used in conventional FD simulations (e.g., Vidale and Clayton, 1986); however, it is difficult to formulate the zero stress condition in terms of potentials such that this approach can be used for the paraxial technique. Method (2) has been successfully implemented using the pseudospectral method (Reshef et al., 1988b) and this is the approach we follow for the PE formulation.

Figure 3.7 compares displacement seismograms calculated for the free surface model using the FD and PE methods. Clearly, the results do not agree well with one another. In particular, very little energy is present near the free surface in the PE calculation, indicating that this interface is not modeled accurately in our formulation.

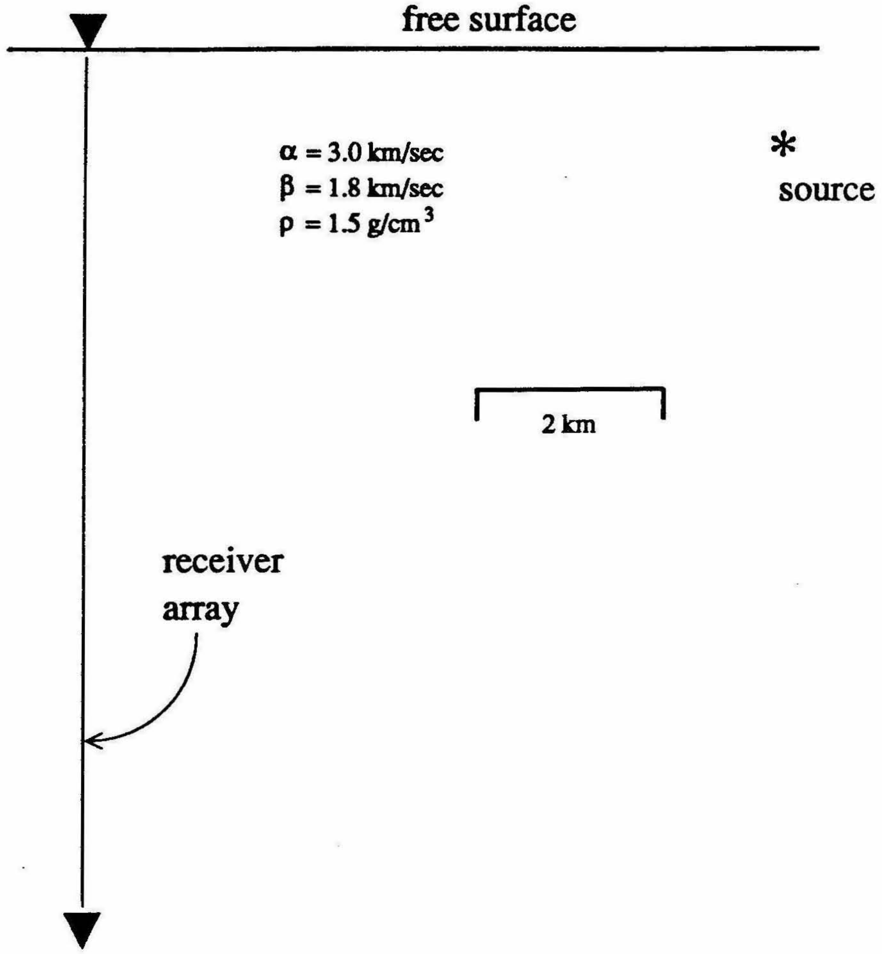

Figure 3.6. Model geometry and media parameters for free surface problem.

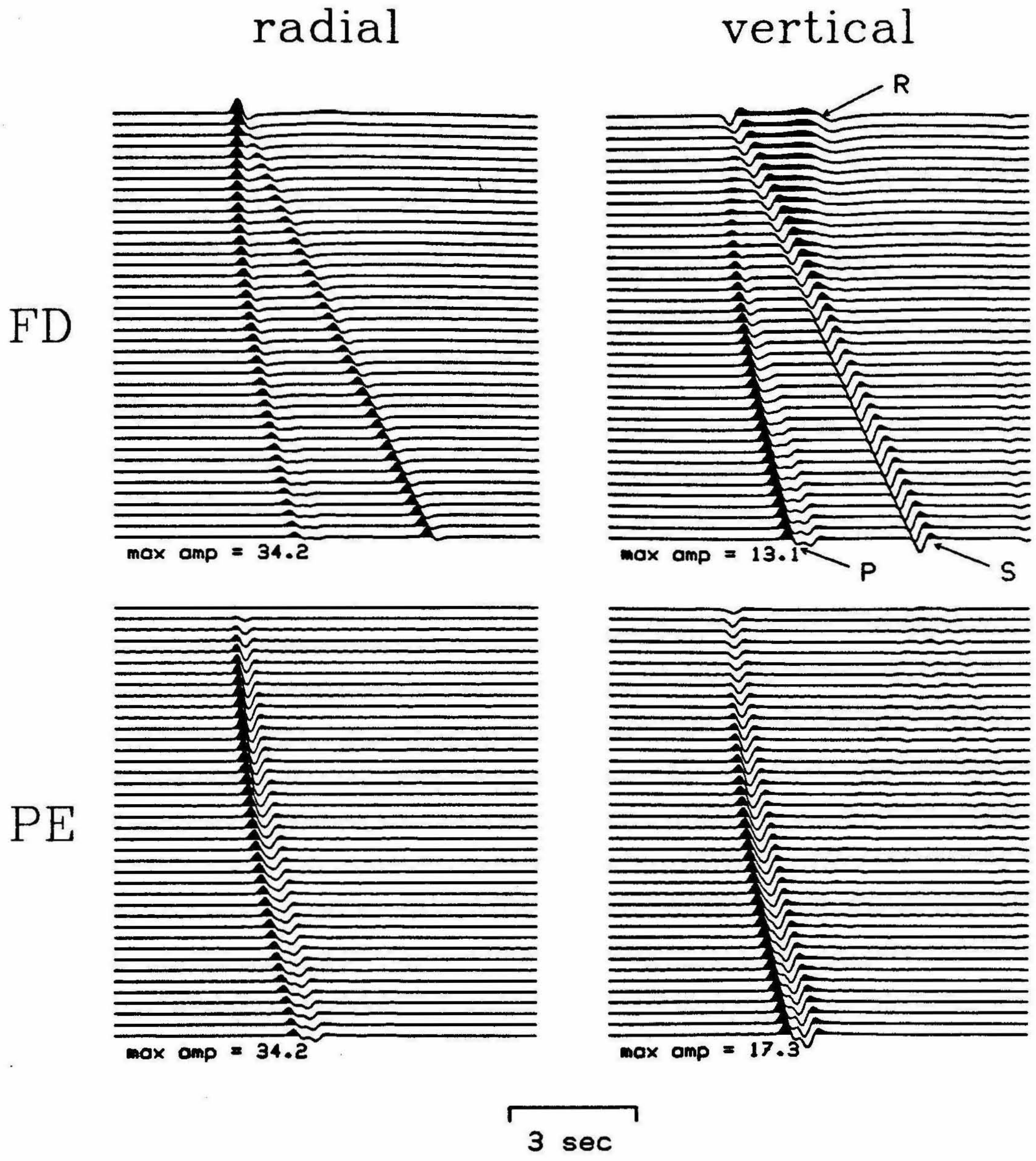

Figure 3.7. Comparison of displacement seismograms calculated for the free surface model using conventional finite-difference (FD) and the paraxial extrapolator technique (PE). The maximum amplitude given below each section corresponds to the peak amplitude found in that section. The two calculations are normalized so that the peak amplitude on the radial component of the FD result matches the peak amplitude on the radial component of the PE result. The labels *P*, *S* and *R* refer to the direct *P* wave, the surface reflected *SV* wave and the surface generated Rayleigh wave. Note that the PE response is very poor in matching the expected result for the near surface receivers.

One drawback with our approach is that the media contrast at the free surface is quite dramatic, thus the assumptions made in deriving the PE scattering formulation in the previous section [equations (3.16)] are probably not valid for this model. A way to reduce this effect is to smooth the boundary vertically. In this manner, the boundary is specified as a gradient in the media parameters which is spread over a finite depth, rather than as a discontinuity occurring at a single point. By doing this, the variation of the media parameters from one grid point to the next is not so severe. This type of approach was used successfully by Stead (1989) to model the effects of topography on the free surface using an 2-D elastic FD technique.

Following this idea, the PE calculation was recomputed, this time specifying the free surface boundary as a gradient spread over 10 grid points. The results are compared with those from the previous calculation in Figure 3.8. We find that the gradient formulation improves the situation slightly, but the response is still far from correct. It appears from this figure, that with either formulation the coupling between the P potential and the S potential is too weak to provide an accurate response along the interface.

Part of the problem may lie in the *implied* free surface boundary conditions used for the P and S potentials. Letting the media parameters go to zero at this interface implies that the scalar potentials must also go to zero in order to satisfy the propagation equations (3.13). This is equivalent to the acoustic free surface boundary condition. Clearly, this is not correct for the elastic problem. A more

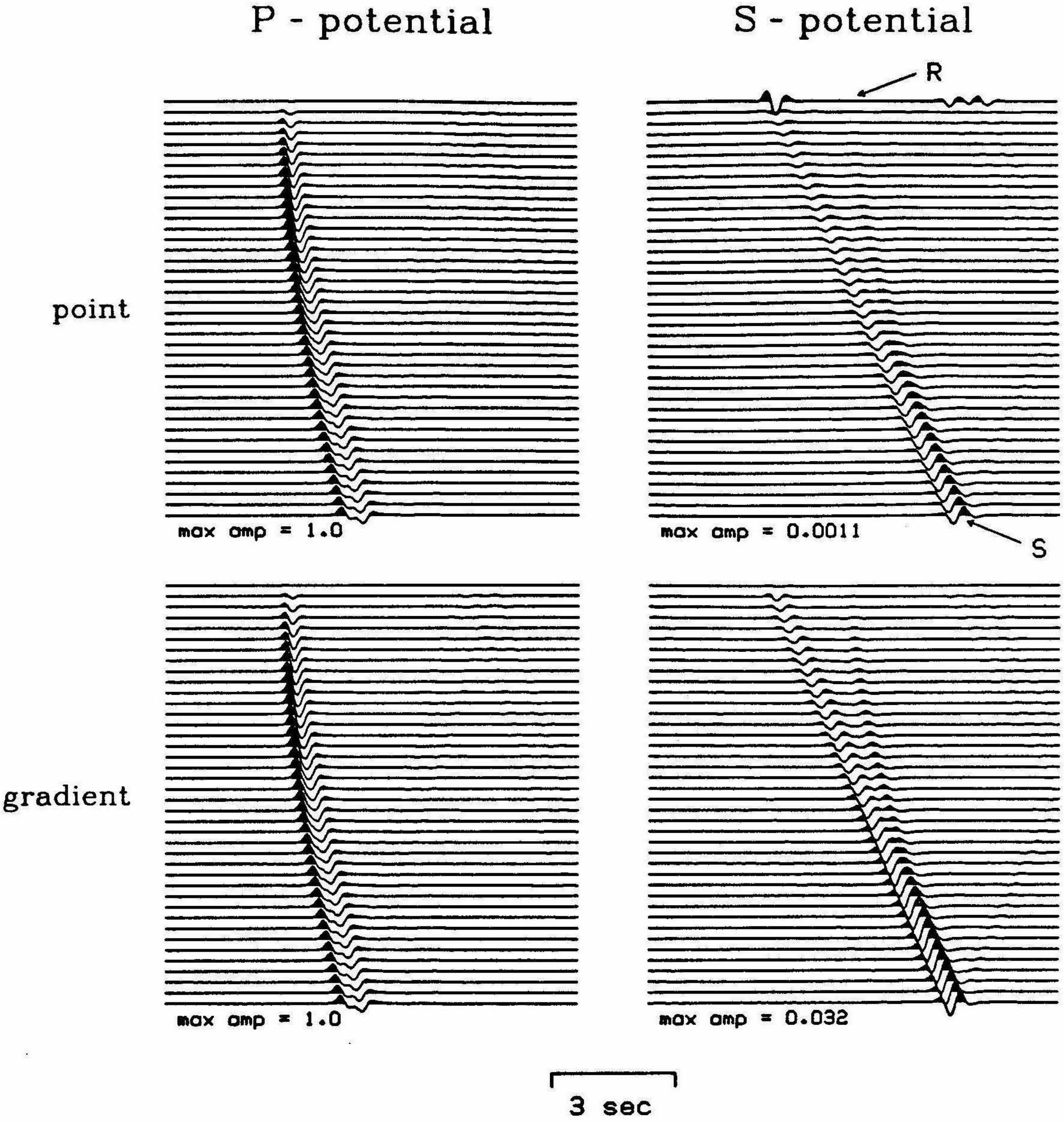

Figure 3.8. Comparison of PE calculations for the free surface model in which the free surface is represented as a point discontinuity (top panel) and as a gradient over 10 grid points (bottom panel). In this figure, the seismograms are plotted as potentials. Amplitude scaling is the same as in the previous figure. The labels *S* and *R* indicate the times at which the *SV* wave and the Rayleigh wave would arrive as predicted by the FD calculation. For this model, the coupling between the two potentials is not computed correctly, thus the energy in the *S*-potential is severely underestimated in both implementations.

appropriate formulation should address the behavior of the individual potentials at the boundary in addition to the effects of coupling produced by the scattering terms.

3.7 Conclusions

The formulation of an elastic wave field extrapolation system using the paraxial technique has proven to be a complicated task. In our approach, we have chosen to describe the elastic system by employing a set of scalar potentials. The primary difficulty with this approach is the incorporation of scattering effects to represent coupling between the potentials in the presence of heterogeneous media.

In order to derive a reasonable set of expressions for the 2-D case, we need to assume that the media variations are small with respect to the reference values of the medium parameters. Numerical tests indicate that this assumption may not be to restrictive for some applications, but this parameterization clearly breaks down when the media contrasts are large, as in the case of a free surface boundary. The inclusion of higher-order approximations in the formulation of the scattering terms may improve this situation (i.e., in a manner similar to that used for the source term described in section 1.5.1); however, doing this will also raise new concerns, e.g., stability considerations and increased computation costs. By formulating an explicit free surface boundary condition (i.e., satisfying a zero stress condition at this interface) for the individual potentials, this problem may be alleviated. Unfortunately, we have not been able to find a straightforward manner in which this can be done.

A mathematical description of the 3-D elastic paraxial extrapolation system has been formulated; however, suitable expressions for the discrete implementation of this system have not been derived. In light of the problems still present with the 2-D system, work on the 3-D formulation should be postponed until a better understanding of the 2-D problem is achieved.

Chapter 4

Modeling Path Effects in Three-Dimensional Basins Using a Reciprocal Source Experiment

4.1 Introduction

One of the major concerns facing seismologists today deals with seismic hazard evaluation. This is especially important in regions of high seismic activity, such as the Pacific rim, because many of the large population centers of the world (e.g., Los Angeles, San Francisco, Tokyo) are located in these areas. Since the occurrence of large earthquakes is inevitable in the regions, being able to reliably forecast expected patterns of strong ground motions associated with these events is necessary in order to avert potentially great economic and personal losses.

In terms of addressing this problem, we first need to develop an understanding of the physical processes which are associated with the occurrence of strong motions. In general, we can group these physical processes into three basic categories: (1) source effects, (2) site effects and (3) path effects. The first two categories deal with the physical processes which operate locally within the source region or at the observation site, respectively, while the third is related to wave propagation phenomena which affects the energy as it travels from the source area to the observation site. A substantial amount of previous work has been done on describing the details of the seismic source (e.g., Aki and Richards, 1980, Chap. 3; Heaton, 1982; Kanamori and Satake, 1990) and on characterizing the site response due to local geologic conditions in these regions (e.g., Duke et al., 1972; Kagami et al., 1986; Seale and Archuleta, 1989). Unfortunately, it is much more difficult to quantify path effects because of the enormous complexity of the problem. Every possible source location has an infinite number of observation points, each with its own unique set of wave propagation paths. As a result of this and the scarcity of sufficiently complete data sets, the path effects are usually combined with the source and site effects to obtain empirical scaling relationships which are appropriate for a given generalized region (Joyner and Boore, 1981; Campbell, 1981; Hadley et al., 1982; Abrahamson and Litchiser, 1989). Nonetheless, path effects, particularly in regions containing strongly heterogeneous media, can have a tremendous influence on the observed seismic signal. These effects can include focusing and defocusing of energy, the generation of multiple arrivals and surface waves and the amplification of resonant modes. In light of this, our analysis of seismic hazard should not only be concerned with the development of an accurate model of the seismic source and a description of the response at a given observation site, but also with an adequate analysis of how the energy is propagated from the source to the site.

Recently, several studies have been conducted which address, in detail, the effects of propagation paths through heterogeneous material on the observed patterns of strong ground motions. These include analyses of the 1971 San Fernando, California earthquake (Drake and Mal, 1972; Liu and Heaton, 1984; Vidale and Helmberger, 1988), the 1985 Michoacan earthquake (Flores et al., 1987; Sanchez-Sesma et al., 1988; Bard et al., 1988; Campillo et al., 1989) and the 1989 Loma Prieta earthquake (Somerville and Yoshimura, 1990). These studies found that structural variations along the propagation path can have a profound impact on the amplitude and duration of the recorded seismic signal. However, one drawback of these studies is that the analyses were all performed using two-dimensional (2-D) models. With this approach it is difficult to quantify the effect that 3-D structural variations have on the observed patterns of strong ground motions. The goal in the present study is to improve our understanding of the influence that these 3-D structures have on seismic wave propagation and then use this information to aid in the prediction of strong ground motions for a given earthquake.

The approach we follow is to use the numerical technique described in Chapter 1 to model wave propagation within a prescribed 3-D media. This approach does have some limitations (the paraxial approximation and the restriction to acoustic media), which will be discussed in more detail in a later section; however, the method is capable of handling arbitrary media variations, and thus, effects due to focusing and defocusing, diffraction and the generation of multiple reflections and refractions are modeled quite well. With this technique, path effects for local earthquakes recorded at two southern California stations are analyzed using a reciprocal source experiment. In this experiment, a point source is excited at the given station location and then the wave field is propagated and recorded throughout a 3-D grid of points. The principle of reciprocity is then used to reverse source and receiver locations. This allows us to model all possible source locations within a given 3-D volume for a given site using only one simulation. A numerical check of the reciprocity concept verifies the validity of using this approach.

For the numerical simulations, the station locations were chosen at Pasadena (PAS) and the University of Southern California (USC). These particular sites are well suited for this experiment because they both operate high dynamic range, broadband digital recording instruments and each station is situated in a different geologic setting; PAS is located on a hard rock site while USC is located above a thick column of sediments within the Los Angeles basin. The modeling results show that the 3-D structure of the Los Angeles, San Fernando and San Gabriel basins create strong patterns of focusing and defocusing for paths coming into these stations. By comparing these calculations with earthquake data recorded at both stations, we can begin to investigate the nature in which these propagation effects contribute to observed patterns of strong ground motions.

In the sections that follow, we first describe the compilation of an appropriate structural model for the southern California region of interest. Next, we present a discussion of the modeling technique along with a consideration of the practical limitations in using this type of approach. This is followed by a description of the reciprocal source experiment and its application to the stations at PAS and USC. We conclude this chapter with a discussion of the results and some proposals on ways to improve future analyses of this type.

4.2 Structural model of southern California basins

Before we begin the modeling process, we need to parameterize a structural model which represents the southern California region of interest. Since our numerical modeling technique is based on finite-differences, the media parameters used to describe this model must ultimately be specified on a 3-D grid of points. This, in itself, can be quite a complicated task due to the wide variety of geologic formations and structures found in this region. One approach to this problem is to subdivide the region into small blocks, each of which represents a given geologic province. The velocity and density structure within each province is constrained to vary only as a function of depth and the individual blocks are then combined to form a fully 3-D model. This type of parameterization was used successfully by Magistrale (1990) to derive a 3-D velocity model of southern California for use in determining earthquake locations. For the present study, we are primarily interested in the effect that the large sediment filled basins of this region have on seismic energy which is propagated through these structures. To this end, we have chosen to specify provinces which best represent the geomorphology of these enclosed basins.

In order to simplify the numerical parameterization of the model, the geometries of the basins are specified by using 3-D shapes that have simple mathematical descriptions. The actual model grid which is used during a given numerical simulation can then be calculated, as needed, from these mathematical descriptions. This approach is advantageous for several reasons: (1) only a few parameters are needed to describe the entire model, thus computer storage requirements are tremendously reduced as opposed to retaining the whole model on a 3-D grid of points, (2) the parameterization is not "locked" to a specific grid size, this gives us the flexibility to easily address problems of different length scales and bandwidths without respecifying the model and (3) it allows us to make changes and additions to the model in a convenient and straightforward manner.

We have found that the general shape of an enclosed basin is modeled reasonably well using the lower hemisphere of an ellipsoid (Figure 4.1). The cartesian equation for this ellipsoid is given by

$$x^2/a^2 + y^2/b^2 + z^2/c^2 = 1. \tag{4.1}$$

In the model, we have constrained the x and y axes to lie in the horizontal plane and the z axis is fixed at vertical downward. Using equation (4.1), the lengths of the major and minor horizontal axes of the basin are $2a$ and $2b$, respectively and the depth of the basin is given by c. Based on surface geology and available data on depth to basement rock, the regional model was divided into four enclosed basins, each specified with an expression of the form of equation (4.1). Individual

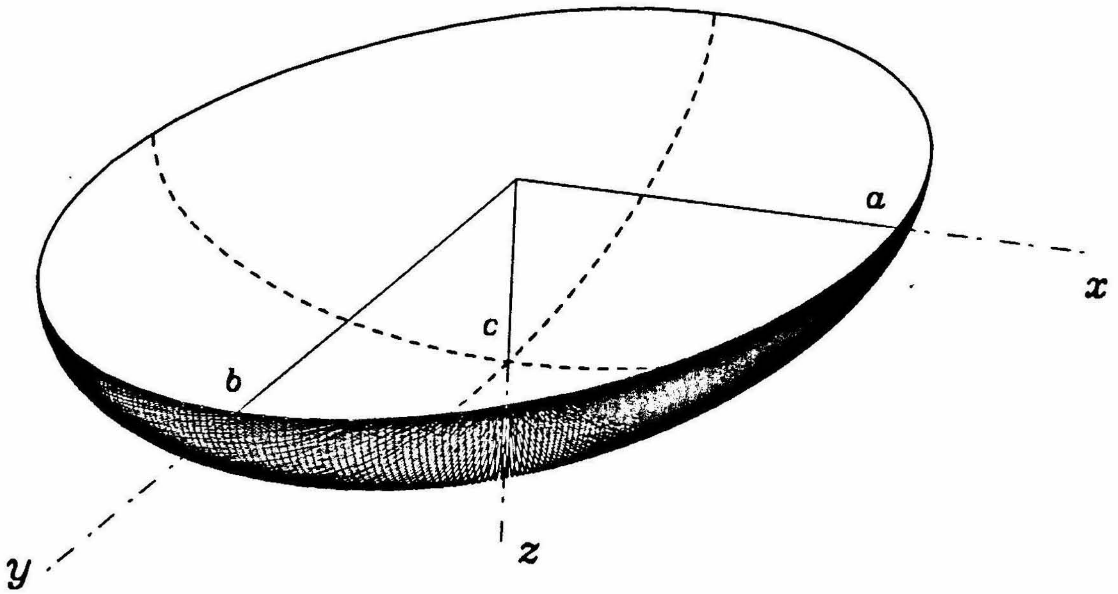

Figure 4.1. Perspective view of the lower hemisphere of an ellipsoid used in the modeling of an enclosed basin. The x and y axes are set in the horizontal plane and the z axis points downward. The parameters a and b control the lengths of the major and minor horizontal axes, respectively, and c specifies the depth of the basin.

basins are defined by selecting the appropriate values of a, b and c for each basin and then translating and rotating the resulting ellipsoid to best conform with the known geologic structure of that basin. The values of these parameters for each of the basins are given in Table 4.1. The surface expression of these basins is compared with a geologic map showing surface exposures of Quaternary alluvium in Figure 4.2. From this figure, it is obvious that the smooth form of the ellipsoids cannot match the details of the actual geology; however, the gross nature of the basins is represented quite well. Below the surface, the detailed structure of the basins is less well constrained, but the general form of the basins is ellipsoidal in shape (Yerkes et al., 1965; Davis et al., 1989). Since we are mostly concerned with determining the large scale influence of these basins on seismic wave propagation, the omission of the small scale variations in structure is probably of no great consequence.

The model is completed by specifying one-dimensional (1-D) velocity and density profiles appropriate for the material within each of the basins, as well as specifying a 1-D background media used to represent the host material around and beneath the basins. The profiles were obtained from sources in the literature and are listed in Table 4.2. These profiles were chosen to be representative of the average vertical structure within each of the provinces. For the Los Angeles and San Fernando basins, the profiles were taken from Duke et al. (1971). These models were derived using well log data and seismic refraction studies. Based on similarities in stratigraphy and structure between the San Gabriel and San

Table 4.1. Geometry parameters for model basins.

basin name	basin center location	rotation angle[1]	major axis ($2a$)	minor axis ($2b$)	depth[2] (c)
Los Angeles	33.86° N 118.12° W	56°	38.5 km	17.0 km	9 km
San Bernardino	34.05° N 117.5° W	-70°	24.0 km	14.2 km	1.5 km
San Fernando	34.22° N 118.45° W	77°	14.2 km	7.0 km	4.5 km
San Gabriel	34.1° N 118.02° W	72°	13.4 km	7.5 km	3.5 km

The values for basin center location, rotation angle, major axis and minor axis were measured from the Geologic Map of California (Jennings et al., 1977). Other references are as noted.

[1] The rotation angle is defined to be the angle between the major axis of the basin and north (counter-clockwise positive).

[2] Depths for the Los Angeles, San Gabriel and San Fernando basins taken from Davis et al. (1989); depth of the San Bernardino basin obtained from Yerkes et al. (1965) and Hadley and Combs (1974).

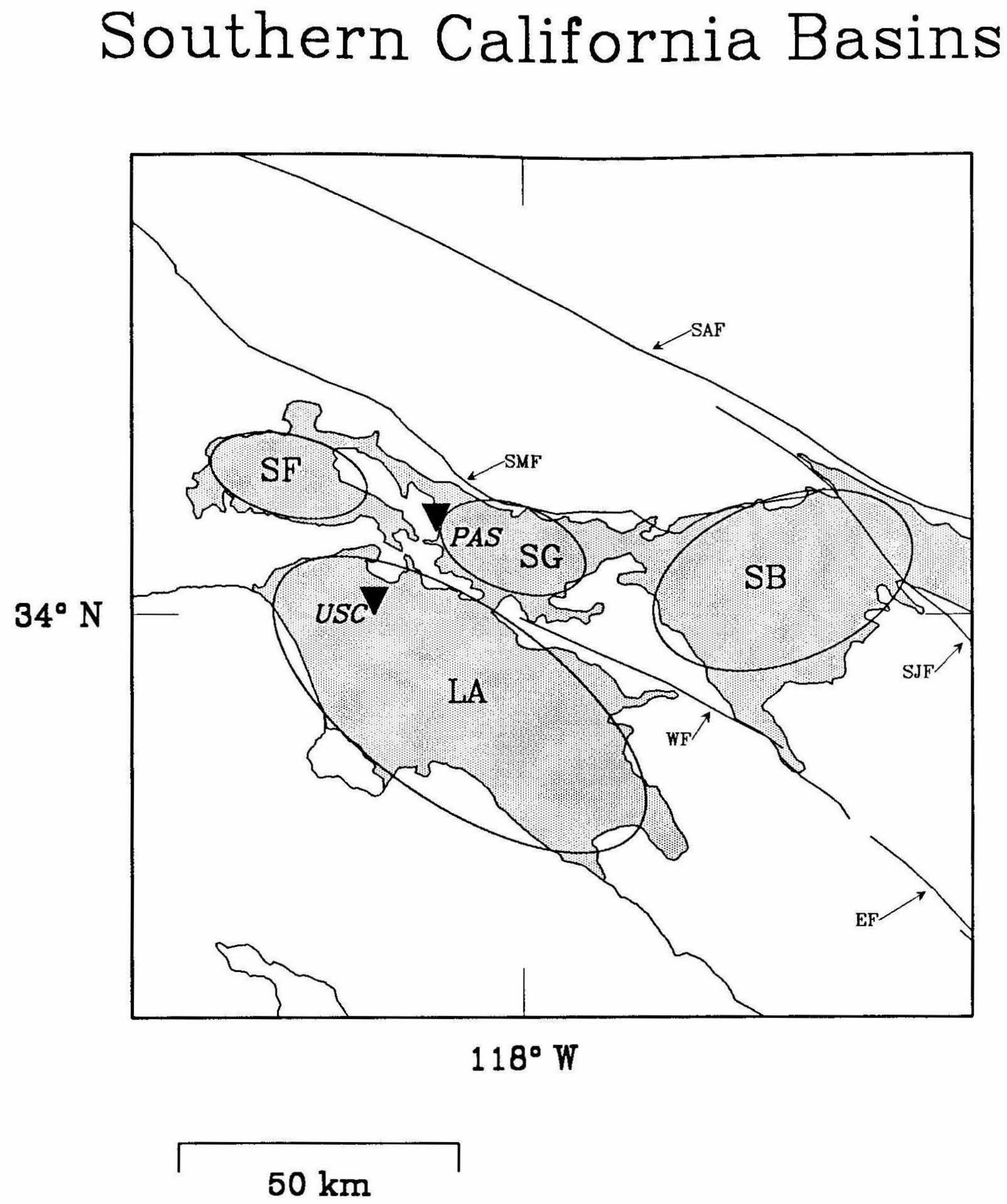

Figure 4.2. Map view of the southern California region showing the location of the basins used in the modeling exercise. The shaded area represents surface exposures of Quaternary alluvium (reproduced from Jennings et al., 1977) which are used to define the outlines of the basins. Ellipsoidal basins used in the model are indicated by the oval outlines which delineate the surface expressions of these structures. For reference, these basins are referred to as; LA - Los Angeles, SB - San Bernardino, SF - San Fernando and SG - San Gabriel. Also shown on the map are the major faults of the region; EF - Elsinore Fault, SAF - San Andreas Fault, SJF - San Jacinto Fault, SMF - Sierra Madre Fault and WF - Whittier Fault, as well as the location of the recording stations PAS and USC (solid triangles).

Table 4.2. Velocity and density profiles for southern California model.

province	velocity	density	depth	reference
Los Angeles basin	2.1	1.8	0.0	Duke et al. (1971)
	2.4	1.9	0.75	
	3.1	2.1	1.75	
	3.5	2.2	3.0	
	4.3	2.3	5.0	
	5.5	2.5	9.0	
San Bernardino basin	2.1	1.8	0.0	Hadley and Combs (1974)
	2.9	2.0	0.5	
San Fernando basin	2.1	1.8	0.0	Duke et al. (1971)
	2.4	1.9	0.5	
	3.0	2.1	1.2	
	3.5	2.2	2.5	
	5.5	2.5	4.2	
San Gabriel basin	2.1	1.8	0.0	inferred from structure of San Fernando basin
	2.4	1.9	0.5	
	3.0	2.1	1.2	
	3.5	2.2	2.5	
Background media	3.6	2.2	0.0	Hadley and Kanamori (1977)
	5.5	2.5	2.0	
	6.3	2.7	4.0	
	6.7	2.9	16.0	
	7.8	2.9	32.0	

Velocity is P-wave velocity measured in (km/sec), density is measured in (gm/cm^3) and depth is to top of layer measured in (km).

Fernando basins (Davis et al., 1989), the velocity and density profiles for the San Gabriel basin were inferred from the San Fernando basin values. This procedure was necessitated by the lack of published information regarding the San Gabriel basin. The velocity and density structure of the San Bernardino basin is rather poorly constrained and is based primarily on a refraction study by Hadley and Combs (1974). For the background media, we used the average southern California model given by Hadley and Kanamori (1977), modified to include a thin, low velocity, near surface layer to represent the uppermost crust.

4.3 Numerical modeling technique

Ideally, to properly analyze the effects of 3-D structure on observed patterns of strong ground motions, one would like to model the full elastic wave field in generally heterogeneous 3-D media. Complete solutions to these types of problems can be formulated using a conventional finite-difference approach, but as discussed section 3.1, this is generally not practical due to the large amount of computer memory required by these techniques. The paraxial formulation presented in Chapter 1 alleviates the problem of limited computer memory, yet this formulation is presently only applicable to acoustic media. Using an acoustic approach to model what is unquestionably a fully elastic problem may seem like a gross oversimplification; however, this type of approach has been used successfully in other areas, for example in the analysis of seismic reflection data. Certainly, the technique is not able to model all of the elastic propagation effects (e.g., P-S coupling) or incorporate appropriate earthquake source mechanisms and radiation patterns; nevertheless, the acoustic formulation is useful in modeling focusing and diffraction effects as the wave field is propagated through heterogeneous media. Using the acoustic approach to develop a quantitative understanding of these effects is beneficial because these same types of phenomena are also present in the fully elastic problem. Following this line of reasoning, we would expect that structures which produce a particular effect in an acoustic simulation (e.g., a crustal wave guide which concentrates and amplifies seismic energy) would also produce similar effects in an elastic simulation.

In order to test this hypothesis, we compare results obtained from an acoustic calculation with those obtained from an elastic calculation for a simulation of the 1971 San Fernando earthquake. Vidale and Helmberger (1988) used a 2-D elastic finite-difference technique to model a profile of three-component strong motion recordings from this event. Their study found that lateral variations in structure along this profile produced strong effects on the observed seismic signals. These effects include variations in amplitude due to focusing and defocusing of seismic energy and generation of surface waves within the sedimentary basins. If our hypothesis is correct, we should be able to model these same types of effects using an acoustic formulation of this problem.

The model which was used in the acoustic simulation is taken from the regional southern California model discussed in the previous section. This model represents a 3-D block of the crust extending to a depth of 25 km and encompassing the entire

San Fernando basin, as well as portions of the Los Angeles and San Gabriel basins (Figure 4.3). The section labeled AA' in this figure roughly corresponds to the location of the profile which was modeled by Vidale and Helmberger in the elastic simulation. Figure 4.4 shows the vertical structure of the acoustic model along AA'.

For this calculation, we have used a volume injection type source (isotropic explosion) set at a depth of 10 km in the model. Numerical implementation of the source was accomplished following the method described in section 1.5.2. The source was driven with Gaussian type time function [equation (1.58)] having a half-width parameter a of 0.6 sec. The energy in this source is concentrated in the period range from 1-10 sec. Ensuring that the entire frequency bandwidth is modeled accurately requires a grid spacing of 0.125 km in the extrapolation direction and 0.25 km in the other two dimensions. This results in a model space occupying 1.2×10^7 grid points.

First, let us examine the results of this calculation as recorded along a dense line of surface receivers located on the profile AA'. Figure 4.5 plots the envelope of the recorded pressure field as a function of time for each of these receivers. For orientation purposes, we have included a sketch of the model cross-section at the bottom of this figure. It is evident from this figure that the structural variations in the model produce significant effects in the recorded pressure field. The relatively low velocity material present in the Los Angeles and San Fernando basins tends to channel and trap seismic energy, thus amplifying the strength of

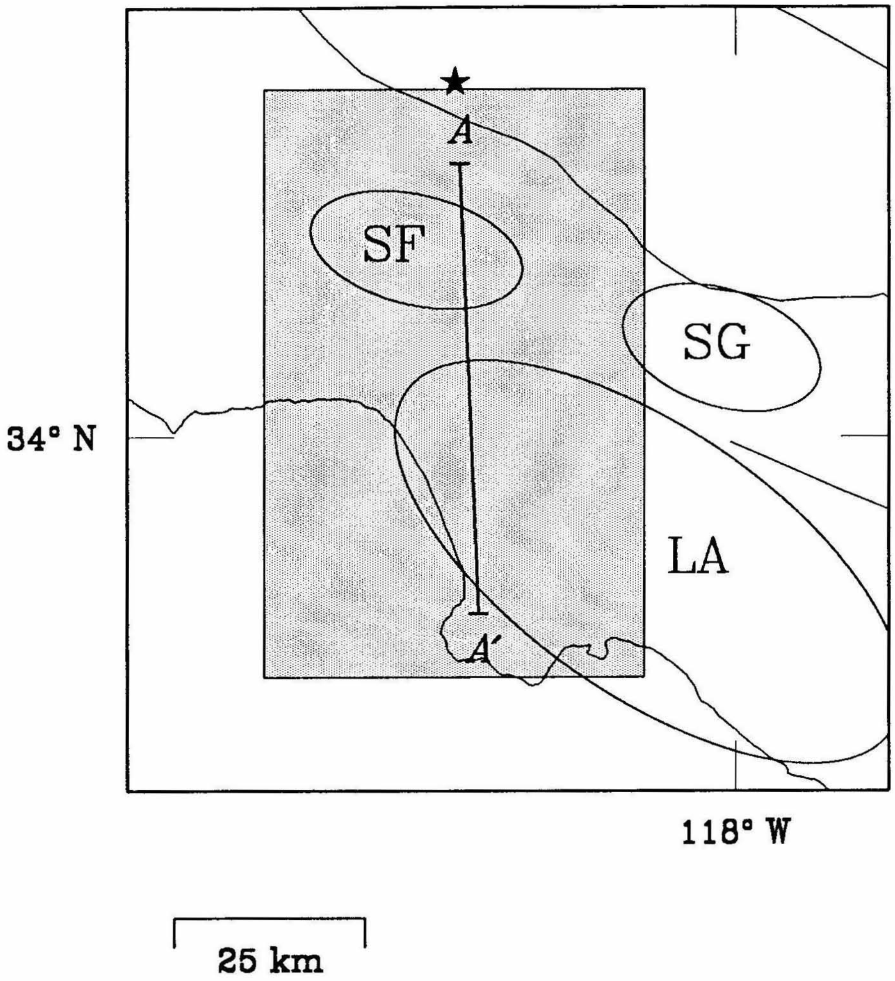
San Fernando EQ

Figure 4.3. Map view showing surface expression of the 3-D model (shaded region) used for the acoustic simulation of the San Fernando earthquake. Epicenter is indicated by the star. Basins and faults are the same as shown in Figure 4.1.

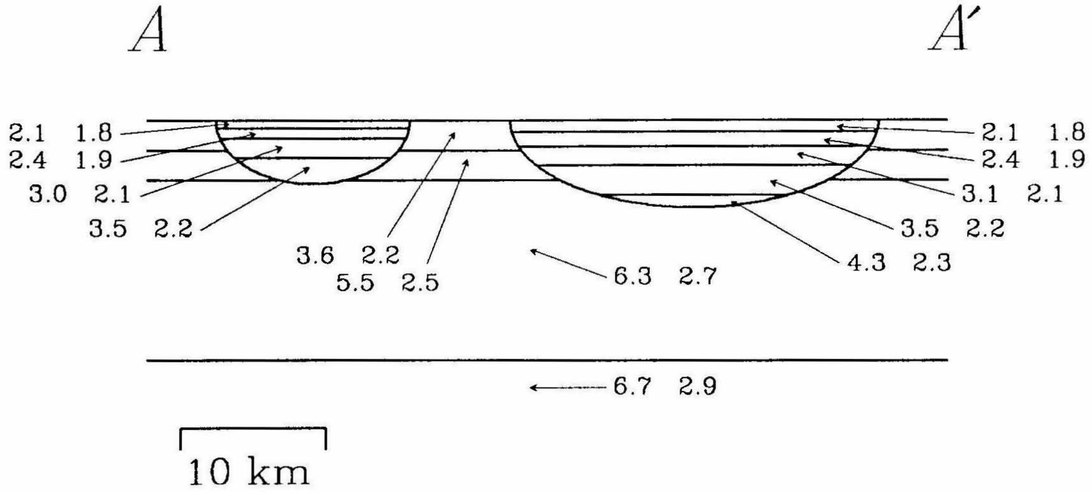

Figure 4.4. Vertical cross-section of 3-D acoustic model taken along the profile AA' shown in Figure 4.3. Paired numbers are P-wave velocity (km/sec) and density (g/cm^3) for each of the layers in the model. The bowl-shaped features in this section are the San Fernando (on the left) and Los Angeles (on the right) basins. Structurally, these basins are separated by the east-west trending Santa Monica mountains.

the signals observed in these areas as opposed to those signals observed along the ridge of the Santa Monica mountains. In addition, the geometry of the layered structure within the basins creates a series of multiply refracted and reflected arrivals (surface waves) which propagate across the section with a slow apparent velocity. These surface waves are created at the near source edges of both basins, although some of the surface wave energy originating in the San Fernando basin tunnels through the Santa Monica mountains into the Los Angeles basin.

The results from the elastic simulation are presented in Figure 4.6 which is a reproduction of Figure 14 from Vidale and Helmberger (1988). This figure plots the envelope of the transverse (*SH*) component of velocity as calculated with a 2-D elastic finite-difference scheme for a structural model similar to the one shown in Figure 4.4. Here, we have shown only the *SH* component for ease of comparison; the elastic simulation produces similar effects in the radial and vertical components of velocity (see Vidale and Helmberger, 1988 for a more detailed discussion of this profile). Comparing the *SH* results with those from the acoustic calculation shown in Figure 4.5, we see many striking similarities, e.g., the amplification of energy within the basins and the generation of surface waves.

In some sense, this result is not unexpected, due to the closeness of form between the 2-D *SH* wave equation and the acoustic wave equation. In fact, the acoustic results could be made to mimic the *SH* results more closely by simply changing the time scale in Figure 4.5 to match up with that used in Figure 4.6. This would be similar to replacing the P-wave velocities in the acoustic model with

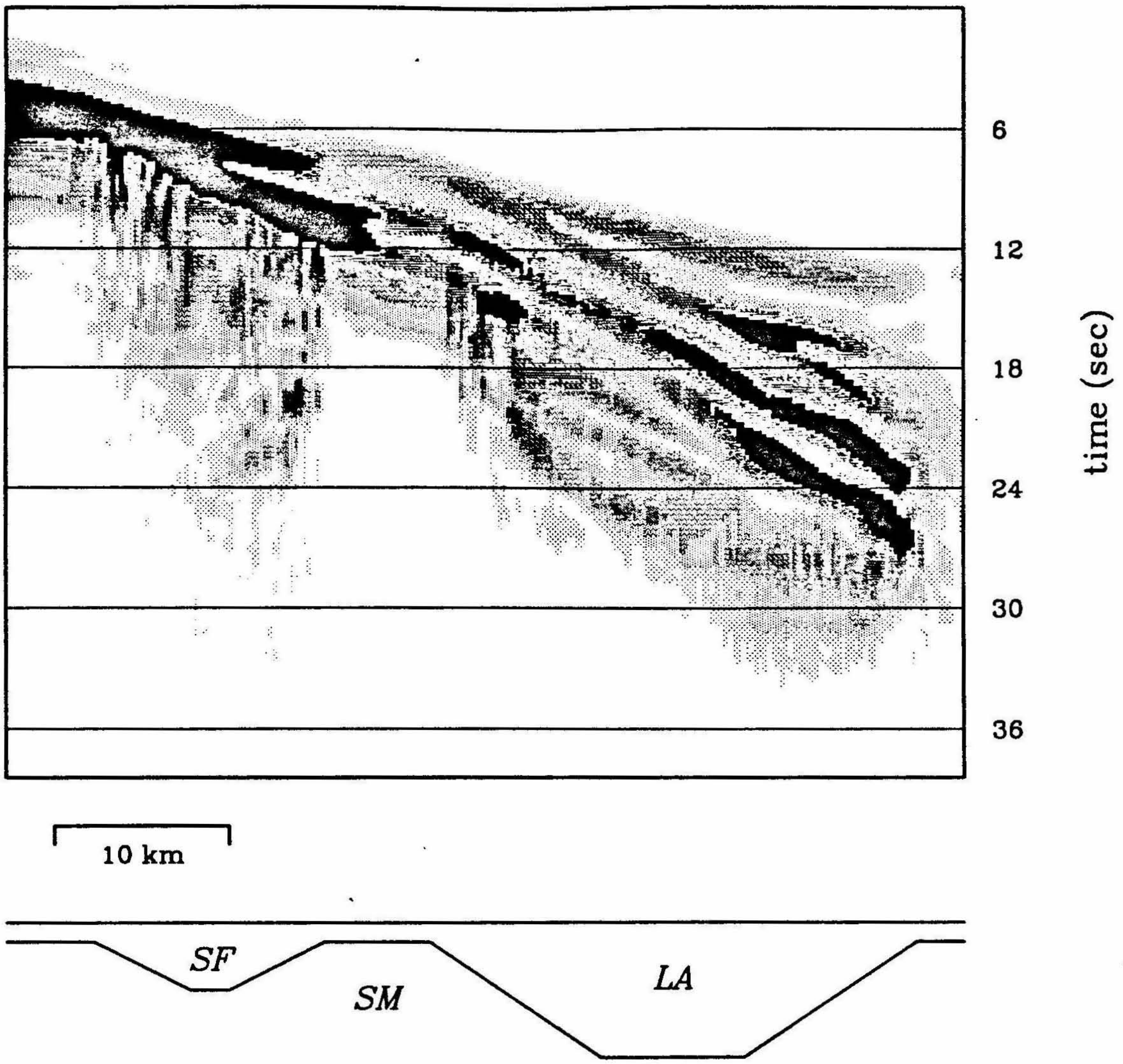

Figure 4.5. A record section of the envelope of the observed pressure field along the profile AA' shown in figure 4.3, as calculated in the acoustic simulation. The intensity of the image is scaled to correspond with the amplitude of the seismic energy that is recorded at a particular time. Thus, the dark portions of the image indicate the highest amplitude arrivals, while the lighter areas indicate arrivals of lesser amplitude. Below the section, we have sketched the major geologic structures along this profile, where LA denotes the Los Angeles basin, SF the San Fernando basin, and SM the Santa Monica mountains.

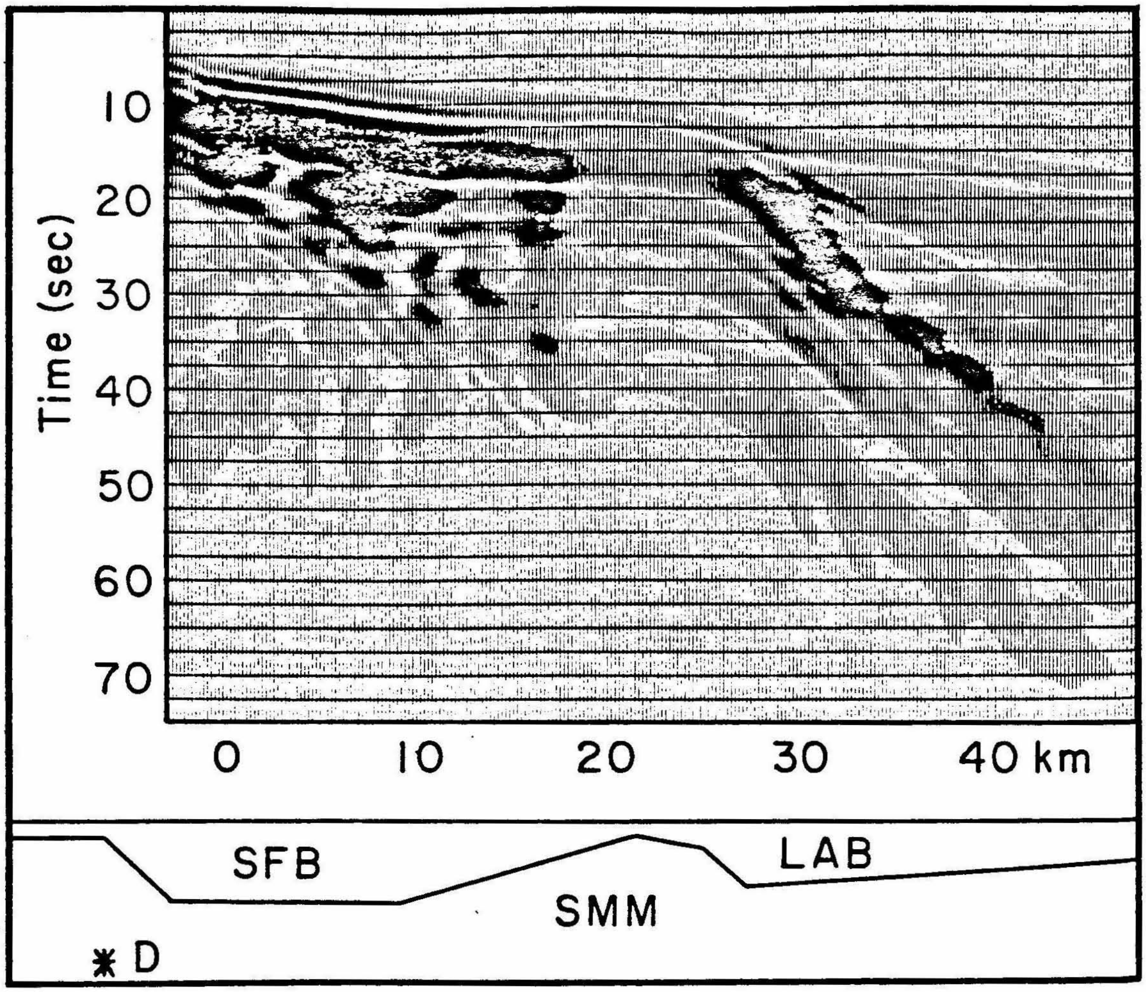

Figure 4.6. A record section of the envelope of the transverse component of velocity along a profile similar to AA', taken from Vidale and Helmberger (1988). The scaling of this image is similar to that of figure 4.5. The major geologic structures along this profile are again sketched below the section, where LAB denotes the Los Angeles basin, SFB the San Fernando basin, and SMM the Santa Monica mountains. The source location used in the simulation is indicated by the asterisk.

the appropriate S-wave velocities and performing the calculation again. This leads to the logical question, why not simply model the *SH* waves in the first place? This is not done for the following reasons.

First, for generally heterogeneous 3-D media, shear waves cannot be completely decoupled into two orthogonal modes, *SV* and *SH*, as they can for 2-D media. In fact, the *SH* wave equation is only strictly valid under the condition that structures are invariant in the third dimension, thus the 3-D *SH* formulation does not represent a true physical system. For media which is only weakly heterogeneous in the third dimension, the *SH* formulation may provide an adequate approximation to the true system. This type of approach would conceptually similar to the one used here in that the propagation effects for a given mode are modeled correctly, yet coupling effects with other modes are neglected.

Using the *SH* formulation presents another problem which results from increased computational requirements. In order to accurately model the same frequency range as used in the acoustic simulations, a finer grid mesh is required in the *SH* problem due to the lower S-wave velocities. Assuming a constant Poisson's ratio of 0.25, the scaling between the P-wave and S-wave velocities would be $V_p/V_s = \sqrt{3}$. Unless a sacrfice is made in terms of frequency resolution, the change in grid size would increase the computation time needed for a given model by more than a factor of five. Because of this added cost, we feel that this approach is not currently practical.

In summary, the comparison between these two techniques is quite encouraging. It appears that the acoustic simulation can reproduce many of the same propagation effects that are modeled with the elastic formulation and this gives us confidence to proceed with the acoustic modeling exercise.

Before discussing the reciprocal source experiment, we have two more comments regarding the preceding comparison. The first concerns the modeling of backscattered energy within the basin structures. As Vidale and Helmberger noted, the elastic calculation produces very little backscattered energy from the edges of the basins. This energy would show up as set of arrivals with a reversed slope to the direct arrivals in Figure 4.6. The paraxial formulation, as stated in Chapter 1, is a one-way extrapolation technique. That is, the propagation aspects of the forward-scattered and backscattered wave fields is completely decoupled and conversions between these two modes must be calculated explicitly. The acoustic results shown in Figure 4.5 represent only the direct forward-scattered wave field (including transmission effects) propagating outward from the source. In order to incorporate the backscattered energy, the reflected wave field would have to be calculated by sweeping through the model in the opposite direction, picking up the backscattered contributions as determined from the scattering matrix (section 1.4). This would effectively double the computation time neeeded for the calculation. Based on the lack of backscattered energy in the elastic simulation, we conclude that this added step is not necessary and that modeling only the forward-scattered energy is sufficient for these types of models.

The second comment we have is in regards to the tradeoffs between using a realistic model of wave propagation (the elastic formulation) with an approximate structural model (the 2-D approximation) versus using an approximate model of wave propagation (the acoustic formulation) with a realistic structural model (the full 3-D parameterization). Although we will not attempt to provide an exhaustive discussion of the relative merits of these two approaches, we will state the following: In order to quantify the effects of 3-D structure on seismic wave propagation, we must be able to model these phenomena in their full 3-D context. This point is illustrated in Figure 4.7 which plots the peak pressure amplitude recorded at all surface grid points used in the acoustic simulation of the San Fernando earthquake. From this figure, it is clear that the variation of peak amplitudes across the model is quite dramatic. While some of these effects could be predicted using 2-D models; e.g., the general amplification of energy within the basins, other effects are truly 3-D in nature; e.g., the east-west variation of peak amplitude values across the San Fernando and Los Angeles basins (values recorded in the northwest portion of the Los Angeles basin are a factor of three greater than those recorded in the northeast portion of the basin, at similar source-receiver distances). Effects such as these would not be easily predicted using simple 2-D models.

In the next section, we will use plots similar to the one shown in Figure 4.7, to map out and quantify the effects of focusing and defocusing on seismic energy as created by the 3-D structure of the basins.

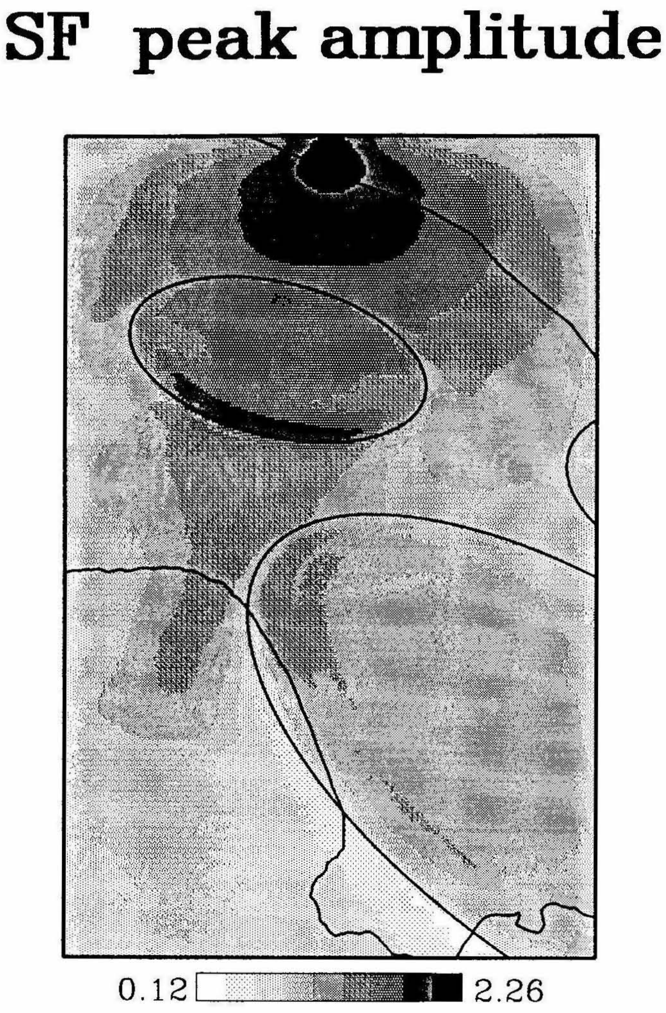

Figure 4.7. Peak pressure amplitude recorded for all surface grid points used in the 3-D acoustic simulation of the San Fernando earthquake. The region shown corresponds to the shaded area of Figure 4.3, with the basin outlines, coastline and faults indicated by the solid lines. A logarithmic ($\log_{10}$) scaling has been applied to the absolute peak amplitude values. Note the strong influence of the basin structures on the observed pattern of peak amplitude attenuation. The anisotropic nature of the source (i.e., weak radiation to the east and west) results from the paraxial approximation used in the calculation. This effect is only significant for energy leaving the source at high propagation angles and has little affect on the region of interest.

4.4 Reciprocal source experiment

Using the technique outlined in the previous section we will now focus our attention on modeling the path effects for data recorded at the stations PAS and USC. Since each of these stations is located in a different geologic setting, we can obtain a relative comparison of the path effects for energy propagating through these different structures by analyzing the response at these stations for a given event.

4.4.1 Forward modeling

In order to model the path effects for arbitrary source locations, we use a reciprocal source experiment. This experiment consists of two numerical simulations, one for the station PAS and one for the station USC. In each simulation we excite a point source at the given station location and then observe the wave field throughout a 3-D grid of points as it propagates away from the site. The principle of reciprocity is then used to interchange source and receiver locations. Using this concept, the wave field observed at a particular grid point is the same as would be observed at the station if the source had been located at that grid point. This approach allows us to model all possible source locations for a given site and within a given 3-D volume using only one simulation. Since we are using isotropic point sources and modeling a scalar wave field, we need not be concerned with the relative orientation or radiation pattern of the sources and receivers. By comparing the results obtained from the two simulations, we can then quantify the nature of the path effects into these two sites for any given source location.

The models used in the two simulations are again taken from the regional southern California model discussed in section 4.2. Each model represents a 3-D block of crust extending to a depth of 25 km and covering an area of 14,400 km^2 (120 km × 120 km). The surface expression of these models is shown in Figure 4.8. Note that the region of overlap between the two models encompasses a large portion of southern California. All grid points lying within this region of overlap represent potential source locations that will be observed at both stations. Since we are interested in the relative nature of the propagation paths into the two sites, only these points will be used in the reciprocal source experiment. Analyzing the same event observed at different sites is useful because we can remove many of the complexities regarding the source from the problem. By doing this, any differences in the observed waveforms at the two sites will result primarily from differences in the propagation paths from the source to each of the recording sites.

For each simulation, the numerical source is located at the surface and is centered within the square lateral area of the model (Figure 4.8). In using the paraxial technique for the simulations, we must take care to ensure that the region of interest lies within the 60° angular accuracy limitations of this method. For example, if we were to extrapolate vertically downward from the source point, propagation paths to grid points at or near the surface would be at about 90° with respect to the extrapolation direction and thus would not be modeled very accurately. Setting the extrapolation direction in the horizontal plane alleviates this problem, yet we are now faced with a lateral variation in accuracy. This

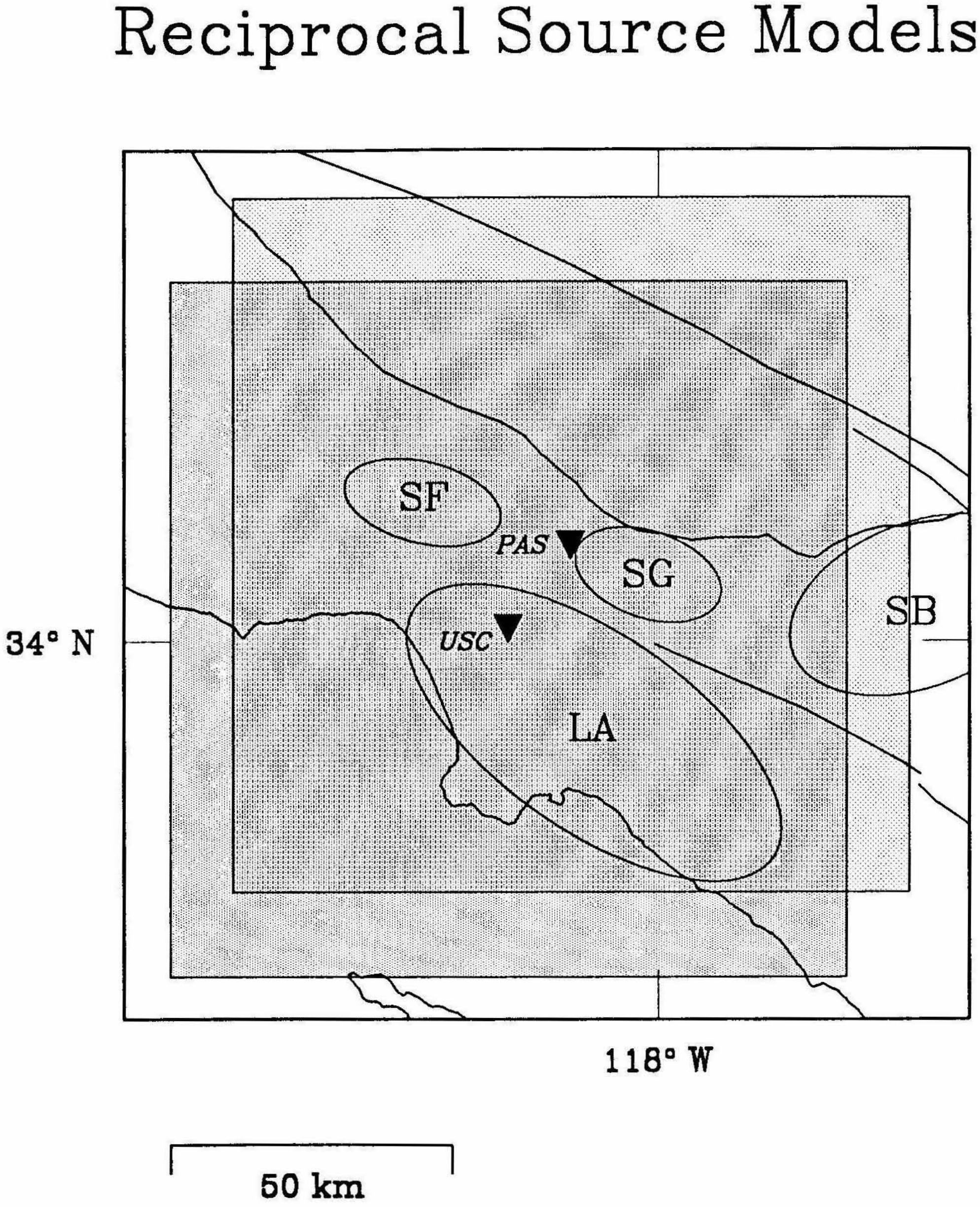
Reciprocal Source Models

Figure 4.8. Map view showing surface expression of 3-D models used for the reciprocal source experiment. The model for station PAS is denoted by the region of light shading and the model for station USC by the region of medium shading. Each station site is located in the center of its respective model and corresponds to the location of the numerical source used in the simulations. The area of heavier shading represents the region of overlap between the two models. Basins and faults are the same as shown in Figure 4.2.

problem can be avoided by dividing the model into four submodels, performing simulations for each of these submodels and then recombining the results from these submodels in such a way as to minimize the region for which the solution has limited accuracy. This idea is illustrated schematically in Figure 4.9.

The first panel (Figure 4.9a) represents the desired model; in this case, the simulation for station PAS. The four submodels are chosen to represent the areas north, south, east and west of the source, respectively (Figure 4.9b). For each of these submodels, the wave field is extrapolated outward from the source in the direction indicated in Figure 4.9b. The results from the submodel calculations are then modified with the application of a weighting function to remove the regions of poor accuracy (Figure 4.9c). The weighting function varies only as a function of azimuth with respect to the extrapolation direction. Denoting the azimuthal direction by θ ($\theta = 0$ being the extrapolation axis), the specific form of the weighting function is given by

$$W(\theta) = \begin{cases} 1, & 0^\circ \le |\theta| \le 40^\circ; \\ (50^\circ - |\theta|)/10^\circ, & 40^\circ \le |\theta| \le 50^\circ; \\ 0, & 50^\circ \le |\theta| \le 90^\circ. \end{cases} \tag{4.2}$$

After weighting the results, the submodels are added together to obtain the final model (Figure 4.9d).

Although it is not indicated in this figure, there is still a limited region of poor accuracy which occupies a narrow cone extending vertically downward from the source. This region could be modeled with the addition of a fifth submodel; however, this is not done for the following reasons. First, the region involves energy

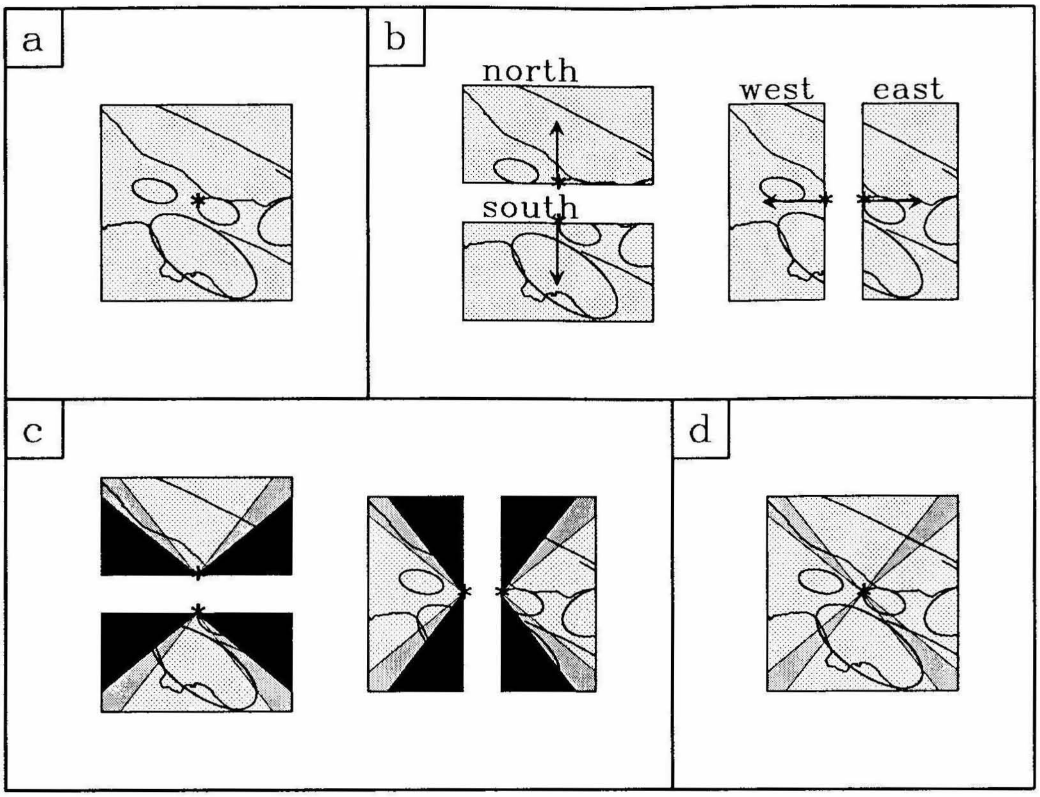

Figure 4.9. Schematic representation of model construction. (a) Desired region to be modeled. Source location is denoted by asterisk. (b) Submodels used to perform the actual simulations. The arrows indicate the extrapolation direction used for each of the four submodels. Recall that the paraxial solution is accurate for propagation angles out to 60° with respect to the extrapolation axis. (c) Map view of the weighting function as applied to each of the submodels. Regions of light shading are all pass, regions of medium shading have a linear taper with increasing azimuth and regions of dark shading are zero [see equation (4.2)]. (d) Final model obtained from the summation of the four submodels. The areas of medium shading indicate regions of overlap between adjacent submodels. The weighting function is designed to sum to a value of unity for all grid points in the final model.

which has left the source with propagation angles of 30° or less with respect to the vertical. This region represents only a small subset of the entire volume which is being investigated. The second reason deals with the one-way nature of the paraxial technique used in the calculations. For near vertical propagation, the multiple reverberations among the predominantly horizontal layers of the model can become quite significant. In order to model all of these phases, we would need to sweep through the model with successive passes of the one-way extrapolators; first downward away from the source, then back upward to the surface to pick up the first-order back-scattered energy. This process of successive passes would have to be repeated many times in order to obtain the higher-order reflections. Obviously, this would require a great deal of computations, involving many hours of computer time. For this reason, we feel that this step is not currently practical.

Before discussing the results of the simulations, there is one more issue regarding the principle of reciprocity that we need to address. Eventually, we will use this principle to interchange source and receiver positions in each of the calculations and then use these results to investigate differences in the propagation paths into the two stations for common source locations. In order to do this properly, we must ensure that the source used in each of the calculations has the same strength. Since we are modeling the acoustic pressure field, the appropriate source to use is a volume injection (Claerbout, 1985b, sec 9.4). This type of source is dimensionless and describes the strain associated with an isotropic explosion. By applying a volume injection source of equal magnitude in each simulation, we can then compare the results along a common baseline. In addition, since we are only comparing the results in a relative sense, the absolute numerical magnitude of the source is not important.

In each of the simulations, the source is driven by a two-sided Gaussian type time function with a half-width parameter a of 0.6 sec [equation (1.58)]. The bandwidth of this source lies in the period range from 1-10 sec. Grid spacing in each of the submodels is 0.125 km in the extrapolation direction and 0.25 km in the other two dimensions. Over 9.2×10^7 grid points are needed to obtain the final model for each simulation.

Unfortunately, the model space is much too large to output and store seismograms for each grid point. In order to reduce the size of the output, the simulations were sampled along horizontal planes at four characteristic depths: 0 km (surface), 5 km, 10km and 15 km. Furthermore, within each of these planes, the output was recorded on a 1 km square mesh. This reduces the size of the retained output to a manageable 1.2×10^5 grid points for each model. By sampling the solutions on a coarse mesh we have lost some information; however, for the period range we have modeled, the effects of spatial aliasing in the output are not that significant.

Since the numerical simulations have been computed using an acoustic formulation initiated with an isotropic point source, the resulting wave fields are only affected by the distance of propagation and the structure sampled along the propagation path. In addition, the effects of anelastic attenuation (seismic Q) have not been included in the modeling process, although this is not a necessary restriction of our numerical method.

Figures 4.10 and 4.11 show wave field time slices for the two simulations, PAS and USC respectively, recorded along the surface of each model. Examining these figures, we see that the presence of the basins has a dramatic influence on the observed wave field. As the seismic energy propagates through the the basin structures, distortions in both the timing and amplitude of the advancing wave field become apparent. These effects are created by the enclosed geometric form of the basins coupled with the relatively low seismic velocity of the layered material within these structures. Some of the observed effects include: (1) waves traveling within the basins are retarded in time relative to waves traveling outside of the basins, (2) energy is channeled and focused by the basin structures, thus amplifying the strength of waves observed in these areas and (3) multiple arrivals and surface waves develop within the basins as the wave field propagates laterally across these structures. These effects act together to create a complex pattern of wave propagation phenomena throughout the entire modeled region.

Figures 4.12 and 4.13 plot the peak pressure amplitude recorded along the four depth planes (0 km, 5 km, 10 km and 15 km depth) for both simulations. In producing these images, the value at the source point is not included since the paraxial solution right at the source is dominated by evanescent energy with erroneously high amplitude (see section 1.5.2). Again, these figures demonstrate the strong influence on the observations resulting from the presence of the basin

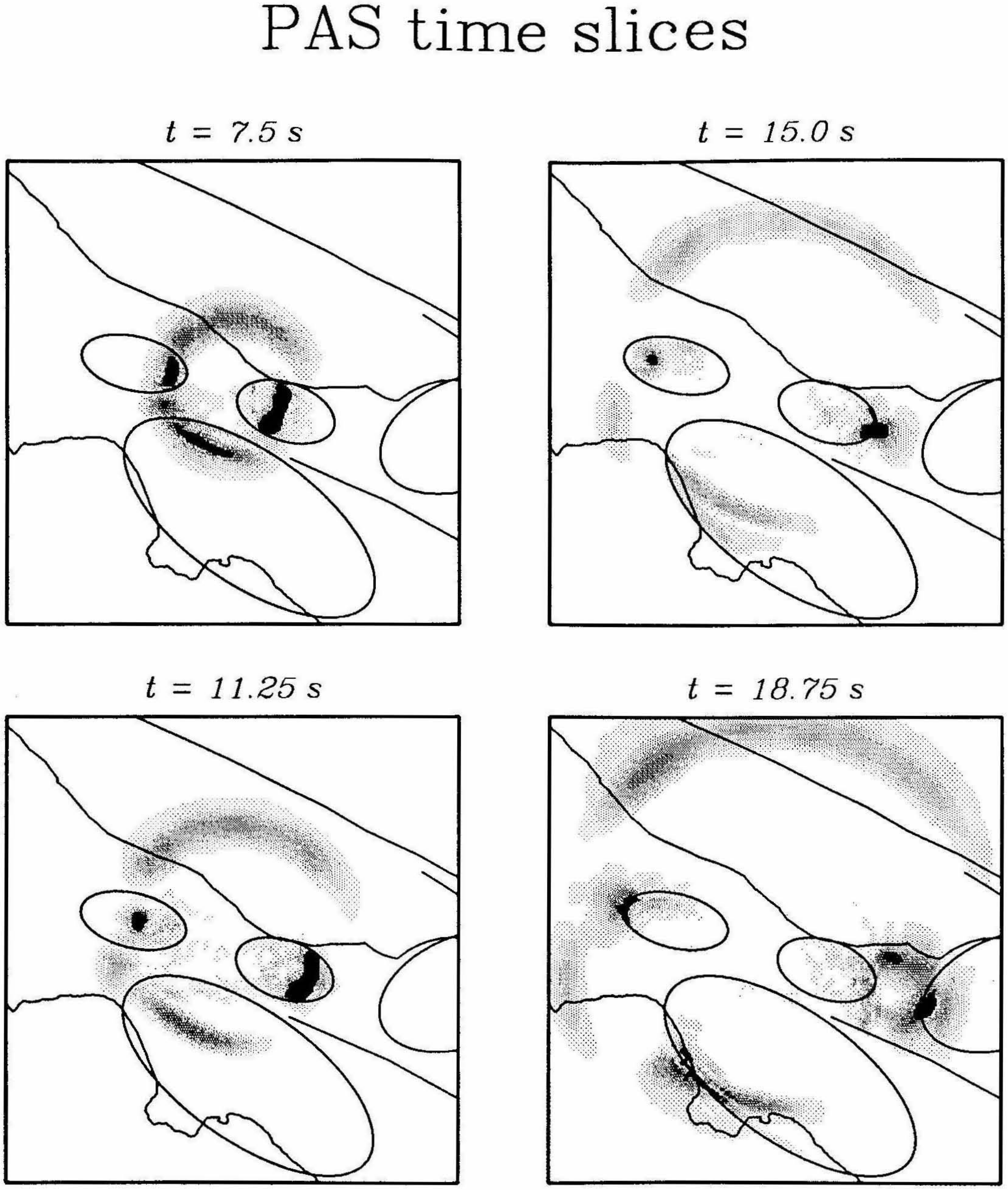

Figure 4.10. Snapshots of the envelope of the wave field recorded along the surface for the PAS simulation at four selected time steps. The area shown in these images represents the surface exposure of the PAS model depicted in Figure 4.8. For each image, the intensity of the wave field is scaled to correspond with the amplitude of the seismic energy which is observed at that time. The dark portions of the images indicate the highest amplitude arrivals, while the lighter areas indicate arrivals of lesser amplitude. Note the strong influence of the basins on the observed wave field.

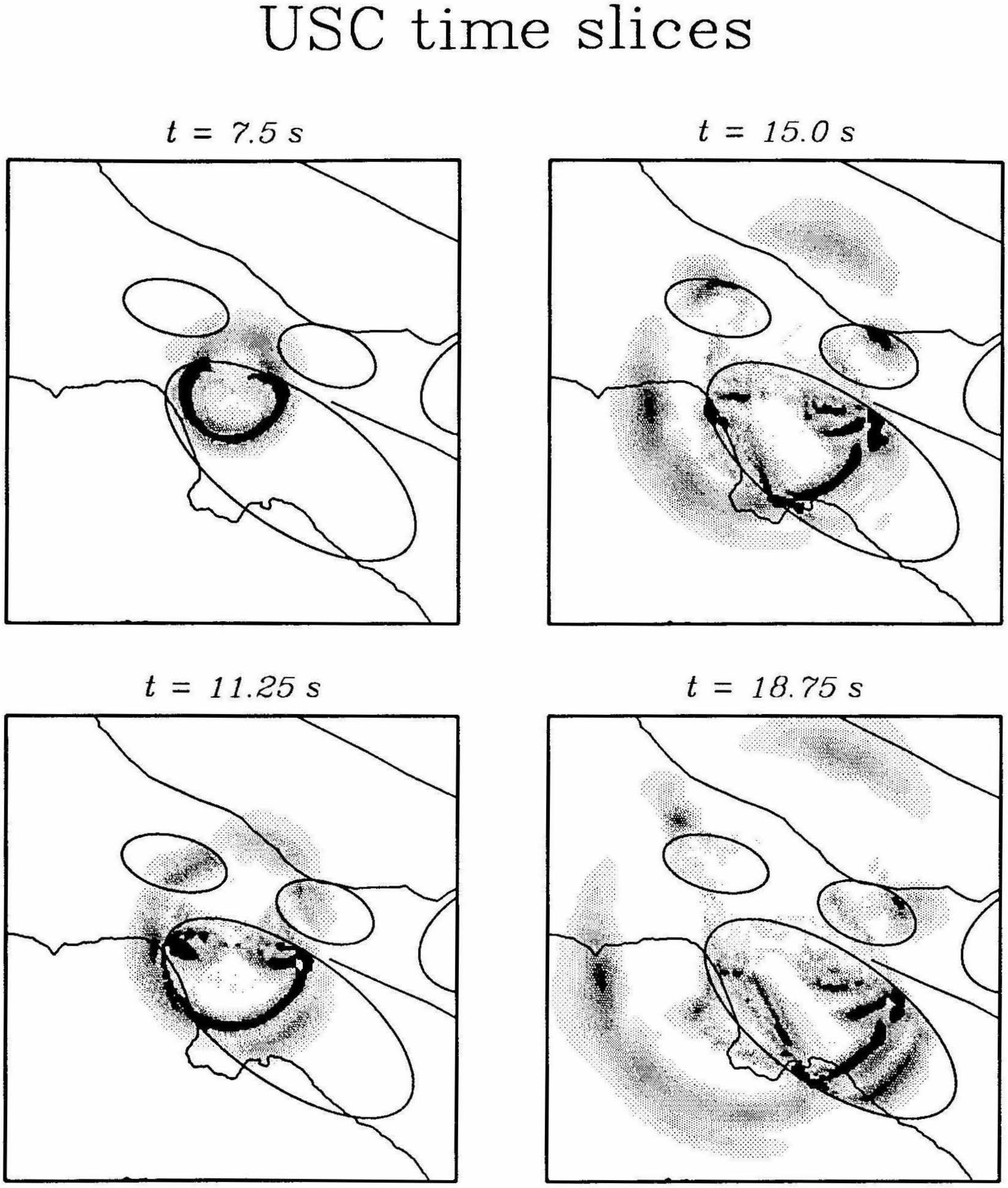

Figure 4.11. Snapshots of the envelope of the wave field recorded along the surface for the USC simulation at four selected time steps. The area shown in these images represents the surface exposure of the USC model depicted in Figure 4.8. Scaling is the same as in Figure 4.10. Again, note the strong influence of the basins on the observed wave field.

structures. The effects due to these structures are most noticeable near the surface and diminish with increasing depth. The peak recorded amplitudes are, in general, higher within the basins than they are in regions outside the basins, although shadow zones (regions of relatively low amplitudes) and bright spots (regions of relatively high amplitudes) are created in areas both inside and outside of the basins, depending on the relative geometry of the basins and the source. This is seen, for example, by comparing results from the two simulations at depth of 10 km beneath the southern portion of the Los Angeles basin. In the simulation for PAS, the Los Angeles and San Gabriel basins channel away energy to create a shadow zone in this region, while in the USC calculation, the Los Angeles basin focuses energy to create a bright spot in this same area. Some of these effects can be simulated using 2-D models (e.g., Hill et al., 1990); however, effects such as the strong azimuthal variation in amplitude attenuation seen in Figures 4.12 and 4.13 would be impossible to predict without incorporating 3-D structural variations into the model.

The influence of the basin structures on the observed patterns of amplitude attenuation is illustrated in more detail in Figure 4.14 where we compare amplitude decay curves for two 3-D numerical calculations. The first calculation is for a model in which the media varies only as a function of depth. The vertical structure of this model is the same as the background or host material used for the regional southern California model (Table 4.2). The second set of curves is taken from the PAS simulation. In order to simplify the comparison, we will examine the

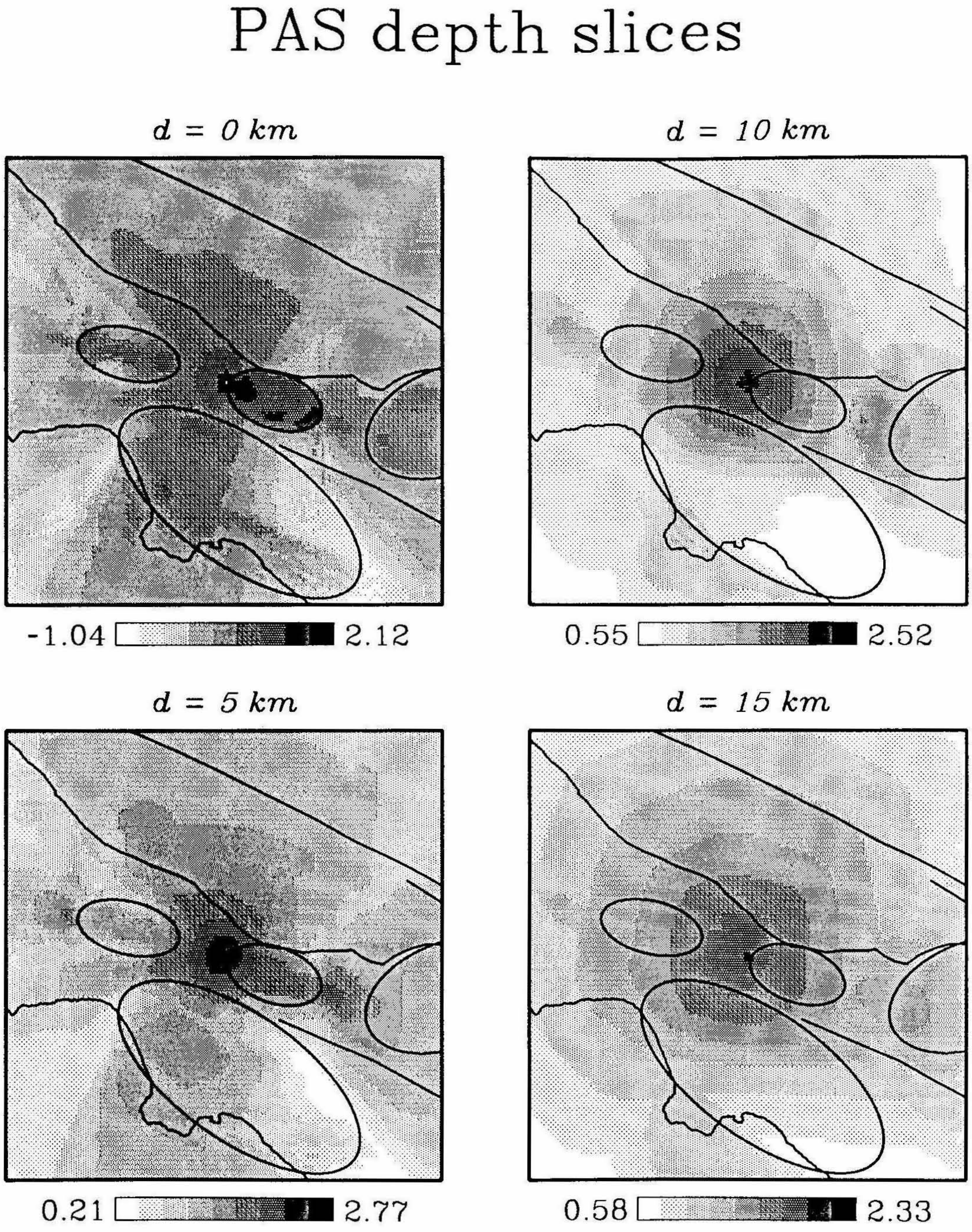

Figure 4.12. Peak acoustic amplitude recorded along four depth slices from the PAS simulation. For orientation purposes, we have superimposed the surface exposures of the basin outlines, faults and coastline on all four images. In each image, a logarithmic scaling ($\log_{10}$) has been applied to the absolute peak amplitude values. The presence of the basin structures creates a complex pattern of amplitude decay throughout the entire modeled region.

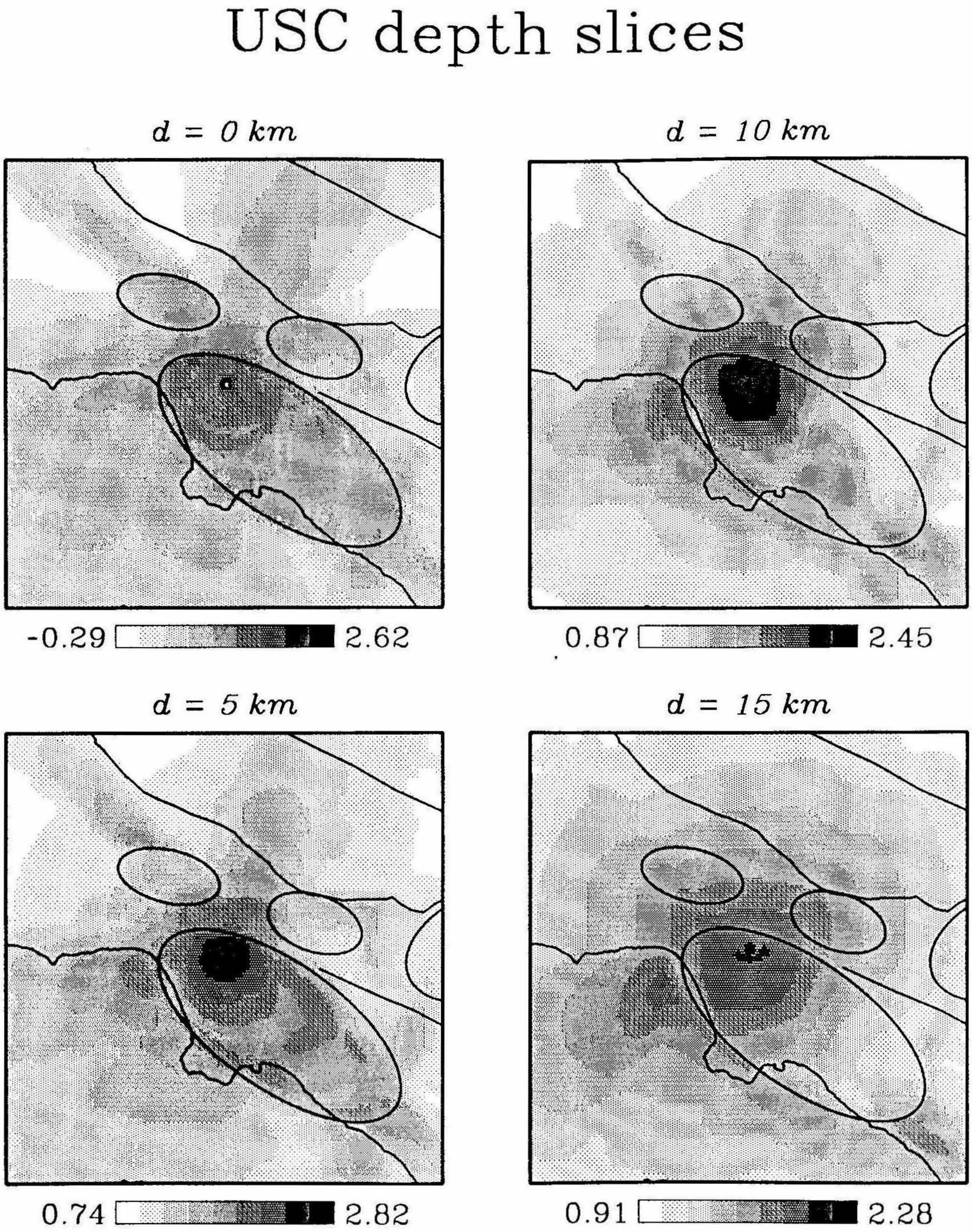

Figure 4.13. Peak acoustic amplitude recorded along four depth slices from the USC simulation. As in Figure 4.12, we have superimposed the surface exposures of the basin outlines, faults and coastline for this model on all four images. In each image, a logarithmic scaling ($\log_{10}$) has been applied to the absolute peak amplitude values. Again, the observed pattern of amplitude decay is strongly affected by the presence of the basin structures.

results along radial lines extending horizontally outward from the source location at depths of 0 km, 5 km, 10 km and 15 km. Although the results from the host calculation are azimuthally invariant, the results from the PAS calculation are highly dependent on azimuth (see Figure 4.12). To obtain a representative slice of the basin structure from the PAS model, the results from this simulation were taken along radial lines heading due east from the source point for each of the four depths. Along this azimuth, the surface line in the PAS model cuts across portions of the San Gabriel and San Bernando basins while the three depth lines all lie beneath these basin structures.

As might be expected, the results for the host model calculation show a simple monotonic decrease in amplitude with increasing distance for all depth slices. The results for the PAS simulation, on the other hand, show a strong influence due to the 3-D basin structures. Near the source, energy is channeled and focused within the San Gabriel basin. This effect not only amplifies the strength of the signals recorded inside the basin, but also creates a shadow zone in the region behind the basin at a distance range of just beyond 20 km from the source. The shadow zone is very strong at the surface and extends to below 5 km in depth. With increasing depth, the two calculations become more similar, although the PAS results still show elevated amplitudes for distances beyond 30 km. The amplification in this region is again a result of the focusing caused by the San Gabriel basin. Initially, this energy was channeled into the basin near the source along the surface of the model. As the energy is transmitted downward through the bottom of the basin

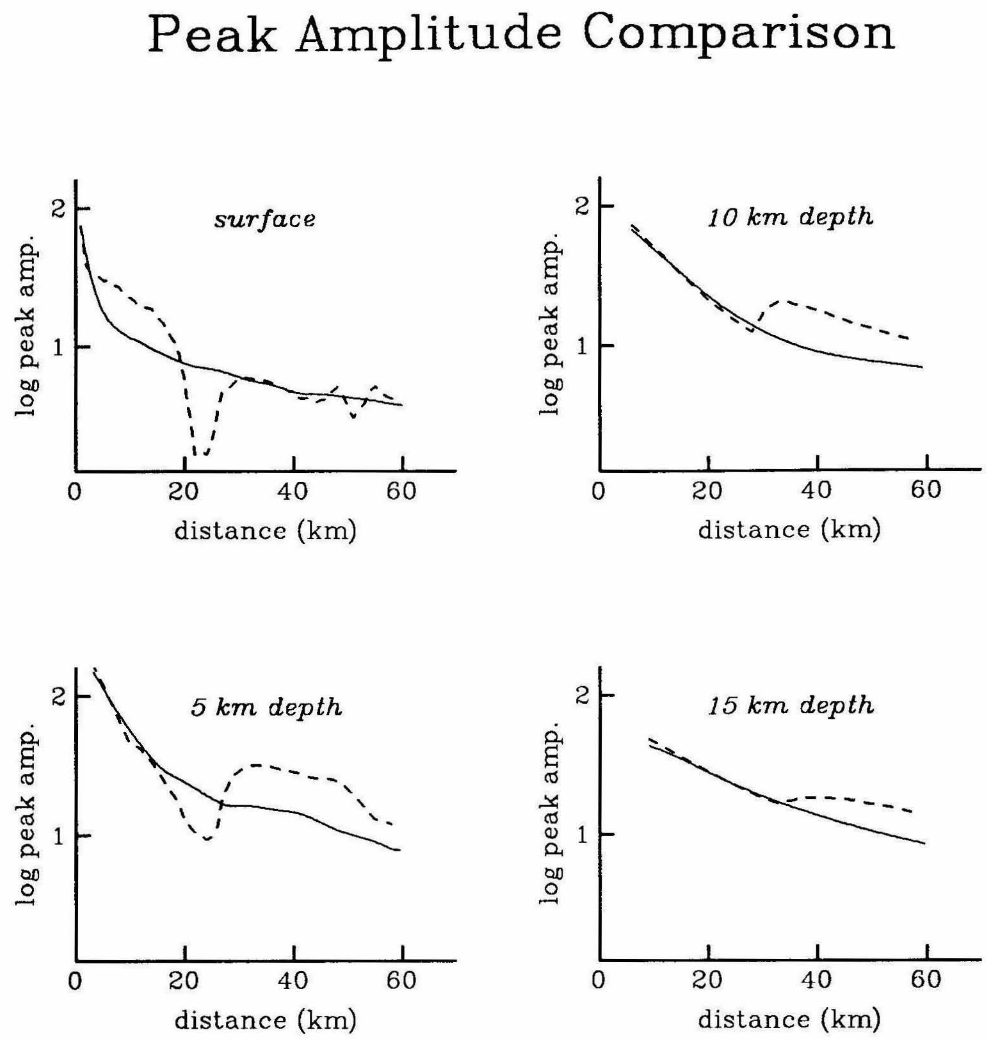
Peak Amplitude Comparison

Figure 4.14. Comparison of peak amplitude decay as a function of horizontal source/receiver distance at four selected depths for two 3-D numerical calculations. A logarithmic scaling ($\log_{10}$) has been applied to the observed peak amplitude values. The first set of results (solid line in each graph) is for a laterally homogeneous model with a vertical structure given by the host material used for the regional southern California model (Table 4.2). The second set of curves (dashed line in each graph) represents results obtained along radial lines heading due east from the source point in the PAS simulation. As discussed earlier, the results have limited accuracy for take-off angles within 30° of vertical, thus, these values are not included in this comparison.

and into the deeper portions of the model, it becomes focused and amplified due to the 3-D geometry of the basin. This process is analogous to the focusing of light rays through an optical lens.

Due to the extremely smooth form of the ellipsoidal basins used in our model, the intensity of the focusing and defocusing predicted by these results may be overestimated. To obtain a semi-quantitative understanding of these effects, consider the following. Focusing of energy results from constructive interference, in space and time, of waves which have been refracted or reflected by different structures throughout the modeled region. For areas of strong focusing, the superposition of the waves is very coherent, with the phase of the interfering wavefronts being nearly identical. If these individual wavefronts are shifted in phase by various amounts, then the pattern of focusing will become blurred and reduced in magnitude. Such a phase shift could result from variations in the model structure which would delay or advance waves scattered from different regions. Assuming that a phase shift of a quarter wavelength or greater will begin to degrade the intensity of the interference pattern, we can obtain a measure of the length scale of the structural variations required to produce this effect for the period range we have modeled. The numerical simulations are peaked at about 2 sec period, which gives a characteristic wavelength on the order of 10 km. The quarter wavelength criterion suggests that structures with length scales on the order of 2-3 km or greater may begin to affect the intensity of focusing. It is reasonable to expect that the actual basin structures contain variations on this order which are not modeled accurately using the ellipsoidal parameterization (see Figure 4.2). Although these variations may affect the intensity of focusing, they should not alter the general pattern of focusing and defocusing observed in the results.

In summary, it is clear from the comparisons presented in Figure 4.14 along with the results shown in Figures 4.12 and 4.13 that the 3-D nature of the basin structures can create complicated patterns of focusing and defocusing which cannot be explained using laterally homogeneous models.

Returning to the results of the PAS and USC calculations, we will now perform a numerical check to verify the principle of reciprocity. If the simulations were parameterized correctly, then the waveform observed at the USC site for the source located at PAS should be the same as the waveform observed at the PAS site for the source located at USC. A comparison of the two observed waveforms is shown in Figure 4.15. Note that the agreement between these results is very good, both in the timing and amplitude of the various phases. The traces in this figure are plotted on the same amplitude scale, and it is apparent that the strength of the observed signals is nearly identical. This is a very important result, because it means that the strength of the sources in the two simulations is also the same. From this comparison, we conclude that reciprocity does exist between the sources and receivers in each of the numerical simulations.

Applying the principle of reciprocity to each of the calculations, we can view the output as a set of seismograms observed at a particular site, PAS or USC, for a variety of source locations. Thus, the waveform recorded at each grid point

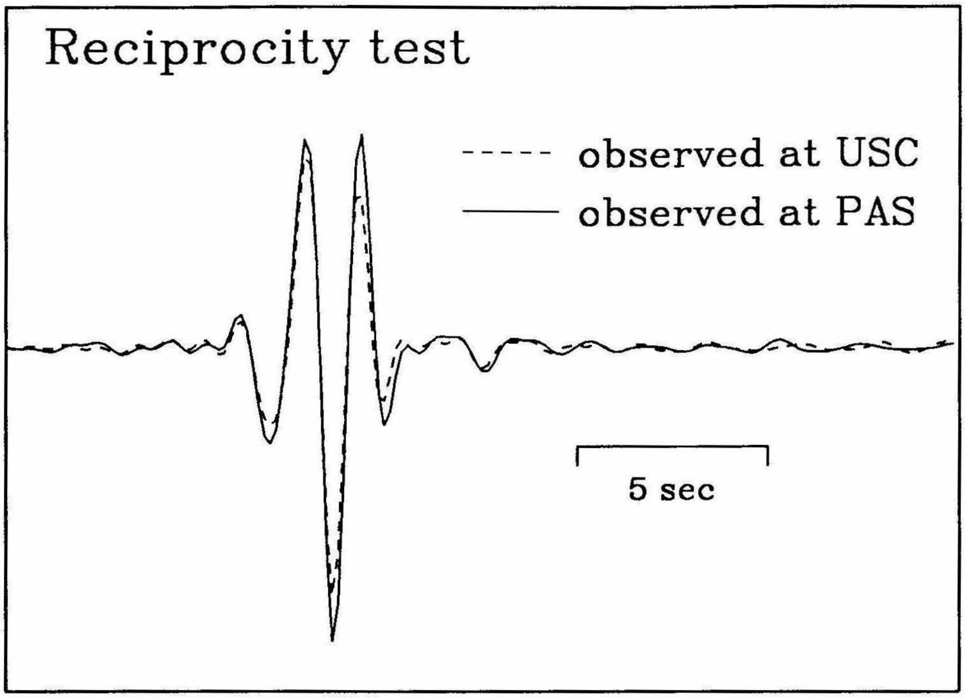

Figure 4.15. Numerical test of source/receiver reciprocity. The dashed line is the waveform observed at USC for a source located at PAS and the solid line is for the reciprocal calculation. The traces are plotted relative to the same amplitude scale.

in each simulation now represents the waveform which would be observed at the station site for a source located at that particular grid point. In addition, since all of the sources have the same strength, we are able to easily compare the results of the two calculations. This allows us to investigate the relative nature of the path effects into these two sites for any possible source located within the region of overlap of the two models (Figure 4.8). In the next section, we will utilize this capability to analyze data recorded at these two stations.

4.4.2 Data analysis

The modeling results presented in the previous section suggest that the presence of the low velocity, 3-D basin structures in southern California can have a significant and noticeable impact on the propagation of seismic wave fields within this region. This hypothesis is tested by comparing the results from our numerical simulations with earthquake data recorded at the stations PAS and USC.

In order to select an appropriate data set, several criteria need to be satisfied: (1) data for a given event must be recorded by the broadband instrument at each station and the location of the event must also lie within the region of overlap of the two numerical models (Figure 4.8), (2) events located directly beneath either station cannot be used due to the limited accuracy of the modeling results in these regions and (3) since the simulations use isotropic point sources, each event must have an known focal solution with a simple radiation pattern. This last requirement is necessary to eliminate those events with complicated sources. Due to the close proximity of the two stations with respect to one another, differences in the observed signals caused by the radiation pattern should not be too significant.

Using the above criteria, three events were selected for the modeling analysis. A map view of epicentral locations for these events is shown in Figure 4.16, along with the surface expressions of the models used for the numerical simulations. Table 4.3 lists the locations and focal parameters for each of these events. The Malibu and Newport Beach events were used by Hauksson (1990) in an analysis of faulting and stress in the Los Angeles basin and the Upland event has been modeled in detail by Dreger and Helmberger (1990).

Broadband recordings of the vertical component of velocity as observed at the two stations for each event are plotted in Figure 4.17. Since the horizontal component data are not available for all of the events, we will use the vertical component data to be representative of the general energy path between the source and a given receiver. This approach is valid in the sense that wave propagation phenomena such as focusing and defocusing of energy and the generation of surface waves will create similar observational effects on the vertical as well as horizontal components.

Due to the flat spectral response of the broadband instruments used in this study, we can view the data shown in Figure 4.17 as representing the Green's function response of the earth (including anelastic attenuation) convolved with the appropriate source time function for each event. For the small events used in this study, the source time function can be adequately approximated as a delta

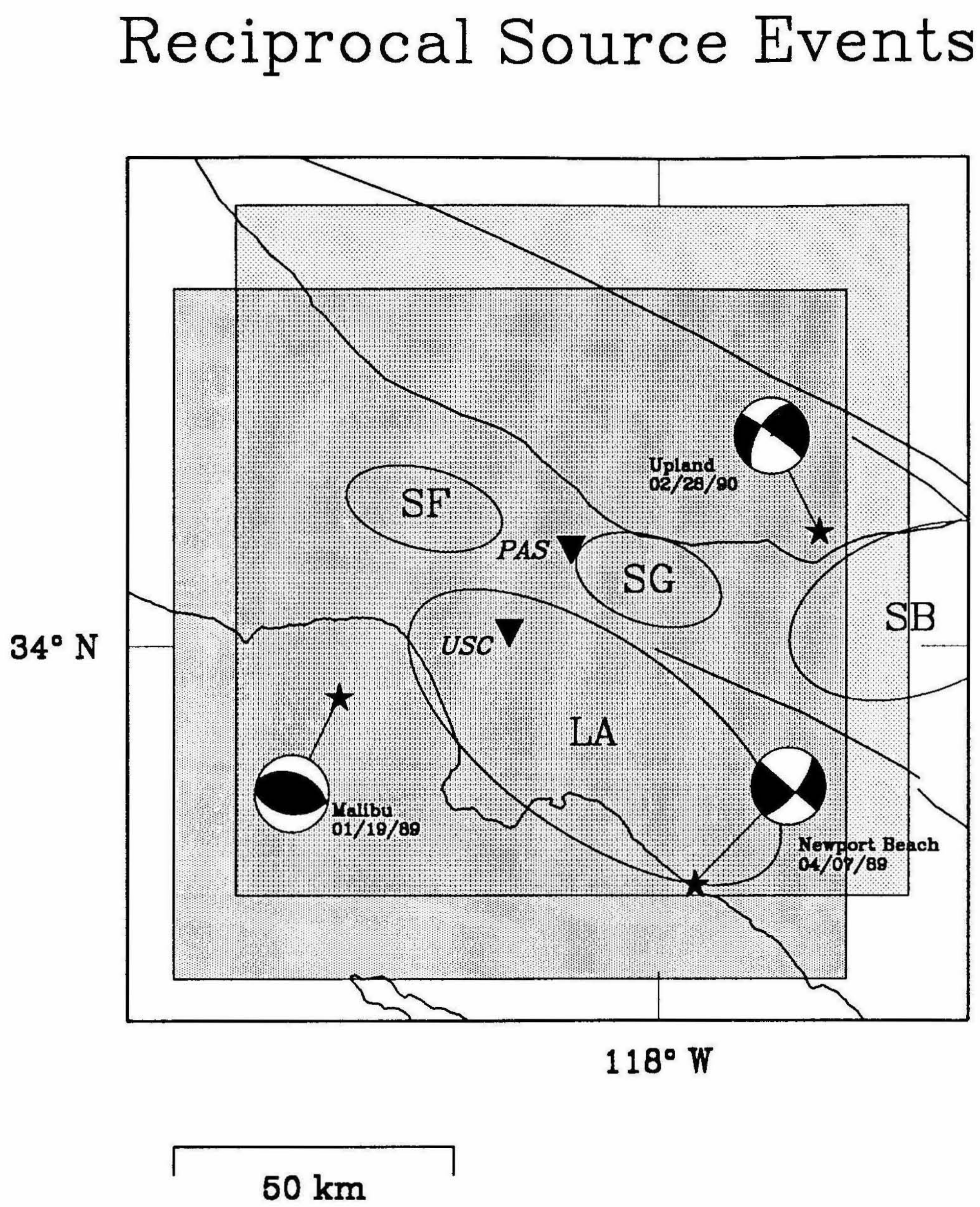

Figure 4.16. Map view showing surface expression of reciprocal source models along with the locations of the three events (location is denoted by a star) used for the data analysis. The focal mechanism for each event is also shown. Basins, faults and model outlines are the same as shown in Figure 4.8.

Table 4.3. Locations and focal parameters for studied events.

earthquake	location	M_L	depth	strike	dip	rake
Malibu 01/19/89	33.92° N 118.62° W	5.0	13.8 km	-71°	45°	99°
Newport Beach 04/07/89	33.63° N 117.93° W	4.6	11.6 km	-50°	90°	160°
Upland 02/28/90	34.18° N 117.69° W	5.5	6.0 km	212°	60°	-6°

The parameters for the Malibu and Newport Beach events were obtained from Hauksson (1990). Parameters for the Upland event are from Dreger and Helmberger (1990).

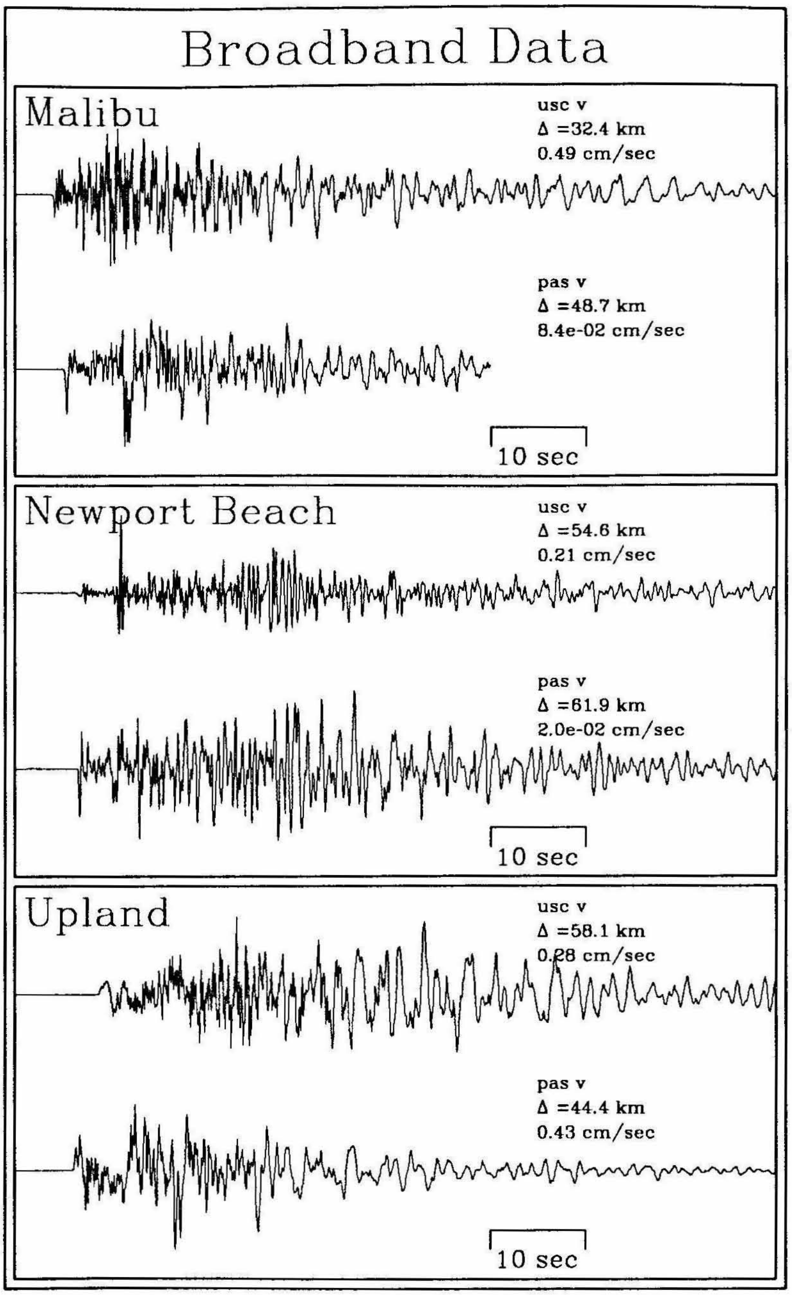

Figure 4.17. Broadband recordings of the vertical component of velocity as observed at the stations PAS and USC for the three events listed in Table 4.3. Traces are plotted relative to origin time for each event. Peak recorded velocity is listed above each trace.

function, and thus, we can regard the data as just the Green's functions for elastic wave propagation through the given earth structure. This property allows us to examine the path effects for any given frequency range by simply applying a bandpass filter to the data. In order to match the frequency bandwidth of the modeling results, the data has been filtered with the same Gaussian time function used to drive the numerical simulations. The filtered data are plotted in Figure 4.18.

Comparing the observations at PAS and USC shown in Figure 4.18, we can make some general statements about the characteristics of the data recorded at these stations for each event. First, the coda observed in the records from USC is much longer than that seen in the records from PAS. The longer coda at USC develop primarily from the interaction of the propagating wave field with the complicated structure of the Los Angeles basin. As the energy travels through the basin, the waves are reflected and refracted many times within the subsurface structure, thus resulting in a long series of arrivals at this site.

Another interesting characteristic seen in these data is the much wider range in the ratio of the peak amplitudes observed at the two stations compared to the values predicted using an empirical relationship. This is demonstrated in Table 4.4 which compares the measured peak amplitude ratios from the data (USC relative to PAS) to the values obtained from amplitude attenuation curves derived by Joyner and Boore (1981). The empirical values are corrected for station distance and site response. From this comparison, it is apparent that the data are showing

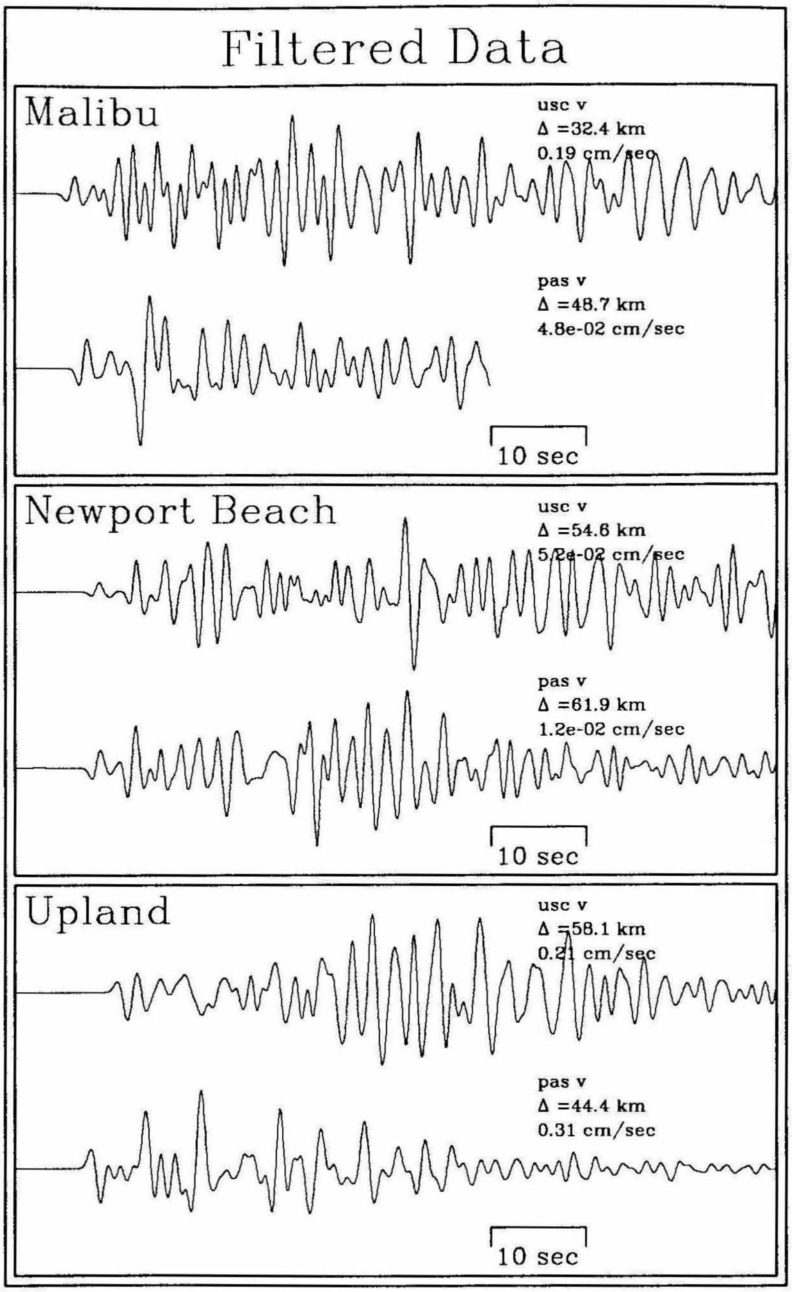

Figure 4.18. Filtered velocity records obtained by convolving the broadband records shown in Figure 4.17 with the Gaussian time function used to drive the source in the numerical simulations. The peak recorded velocity of the filtered records is listed above each trace.

Table 4.4. Comparison of observed and empirical peak amplitude ratios.

earthquake	(USC/PAS) data	(USC/PAS) empirical*
Malibu	4.3	2.5
Newport Beach	4.0	1.7
Upland	0.68	1.0

*The empirical values are from Joyner and Boore (1981). We have used the soft rock curves for USC and the hard rock curves for PAS.

the effects of some physical process which has not been accounted for properly in the empirical relationships, namely, the effects of focusing and defocusing of energy along the propagation path.

Synthetics seismograms were obtained from the reciprocal source models for locations corresponding as closely as possible to the locations of the three events discussed above. Since the results of the numerical simulations were retained only on 1 km square grids at the depths of 0 km, 5 km, 10 km and 15 km, we are not able to match the exact location for each event. However, the modeled event locations will never be more than ± 0.5 km laterally or more than ± 2.5 km in depth from the reported location of the actual event. In all cases, this difference is only a small fraction of the total propagation length and thus, should not have a great impact on the results.

Figure 4.19 compares the observed and synthetic waveforms for the first arriving energy as recorded at the two stations for each event. For these events, the first arriving energy represents the direct P-wave which has been refracted upward from the deeper layers in the crust. In this figure, the data and synthetics are both plotted relative to the origin time of each particular event. The absolute timing of the synthetics has been normalized to best match the timing of the observed record at USC for each event.

For all three events, the relative timing of the observations at the two stations is matched very well by the synthetics. The poorest match is for the Newport

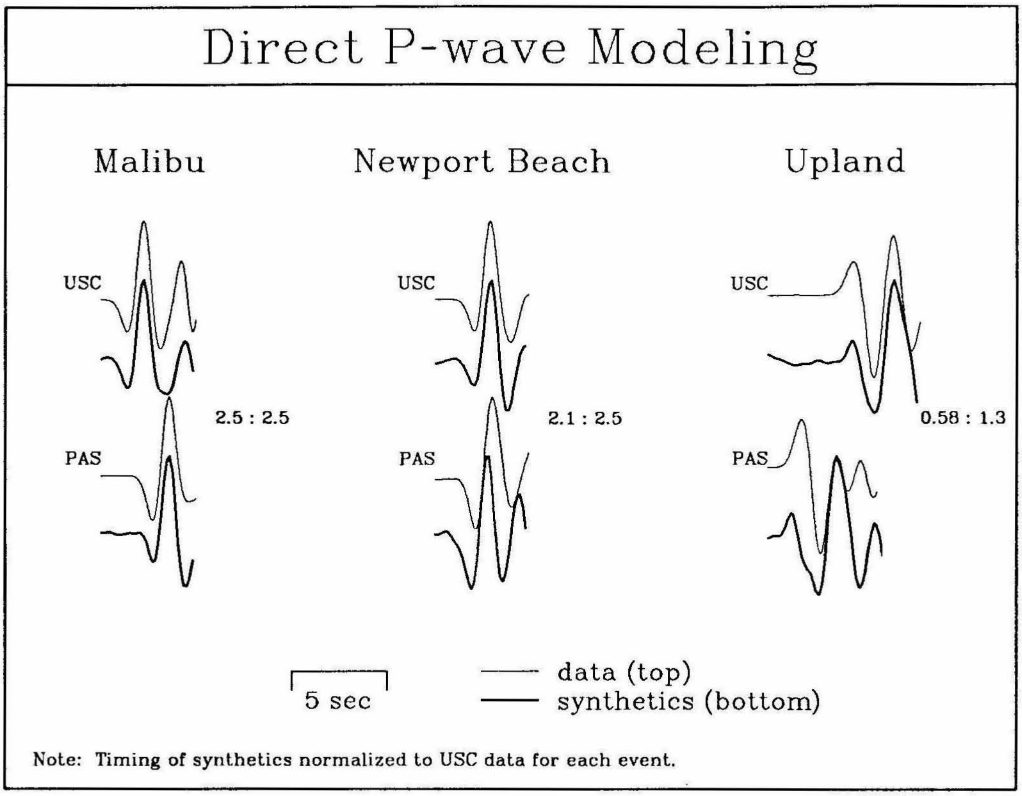

Figure 4.19. Direct P-wave modeling using results from the reciprocal source calculations. Absolute timing of the synthetics is normalized to align the records observed at USC, thus a mismatch in timing will show up as a misalignment of the waveforms observed at PAS. Shown to the right of each set of traces is a pair of numbers in the form $R_d : R_s$. These numbers represent the ratio of the peak recorded amplitudes (USC relative to PAS) for the data, given by R_d, compared to the predicted value obtained from the synthetics, given by R_s. If the two numbers are the same, the predicted amplitude ratio matches the observed value.

Beach event which shows a misalignment in time of only about 0.25 sec for the observation at PAS.

Also shown in this figure are the observed and predicted amplitude ratios for the first arrivals from each event. As discussed previously, differences in amplitude due to radiation pattern should not be significant, since the two stations are located fairly close to one another with respect to the epicentral distance for each event. In addition, this also means that the angle of incidence of the direct P-wave will be similar for the two stations. Thus, the ratio of the amplitudes for the vertical component recordings should give an accurate indication of the relative scaling of the direct P-wave amplitude between the two stations for each event.

Comparing the observed and predicted values, we see a good match for the Malibu and Newport Beach events, but a rather poor fit for the Upland event. The poor match to the Upland data can be explained to a certain extent by the complicated source function of this event. As determined by Dreger and Helmberger (1990), the Upland event is best fit by a double source model with a time lag of 0.75 sec between the two spatially distributed sources. For a complex source such as this, effects such as directivity and pulse interference can have significant influence on the amplitudes of the first arrivals. In order to properly simulate this behavior, we could use the results of the reciprocal source experiment as Green's functions to represent the rupture process of various segments across a finite fault plane. In light of the preliminary nature of the present study, we will defer this type of analysis for future work.

Figure 4.20 displays the full synthetic waveforms for each of the modeled events. Although, the synthetics cannot match the details of the observed waveforms shown in Figure 4.18, they do exhibit the same general characteristics that are seen in the data for each event. For example, the simulated records at USC for each event show a generally longer coda as compared to the simulations for PAS. Furthermore, the ratio of the peak amplitudes as predicted by the synthetics for the two stations agrees fairly well with the values measured from the observations for each of the events (see Table 4.5).

In summary, the results of the direct P-wave modeling are very good, particularly for small events with simple sources. This indicates that our generalized structural model of southern California is appropriate and, in addition, it also illustrates the effectiveness of using the reciprocal source models to simulate the expected response for arbitrary source locations. Comparing the results shown in Table 4.5 with the results shown in Table 4.4, we see that the peak amplitude ratios obtained from the numerical simulations are, in general, closer to the data than the empirical values given in Table 4.4. Although we have not obtained a perfect fit to the observed amplitude ratios, the results of this comparison are encouraging and indicate the importance of incorporating path effects when modeling these types of data.

4.5 Conclusions

In this chapter, we have presented a technique to analyze path effects for seismic wave propagation in 3-D structures. Although the technique is based on an

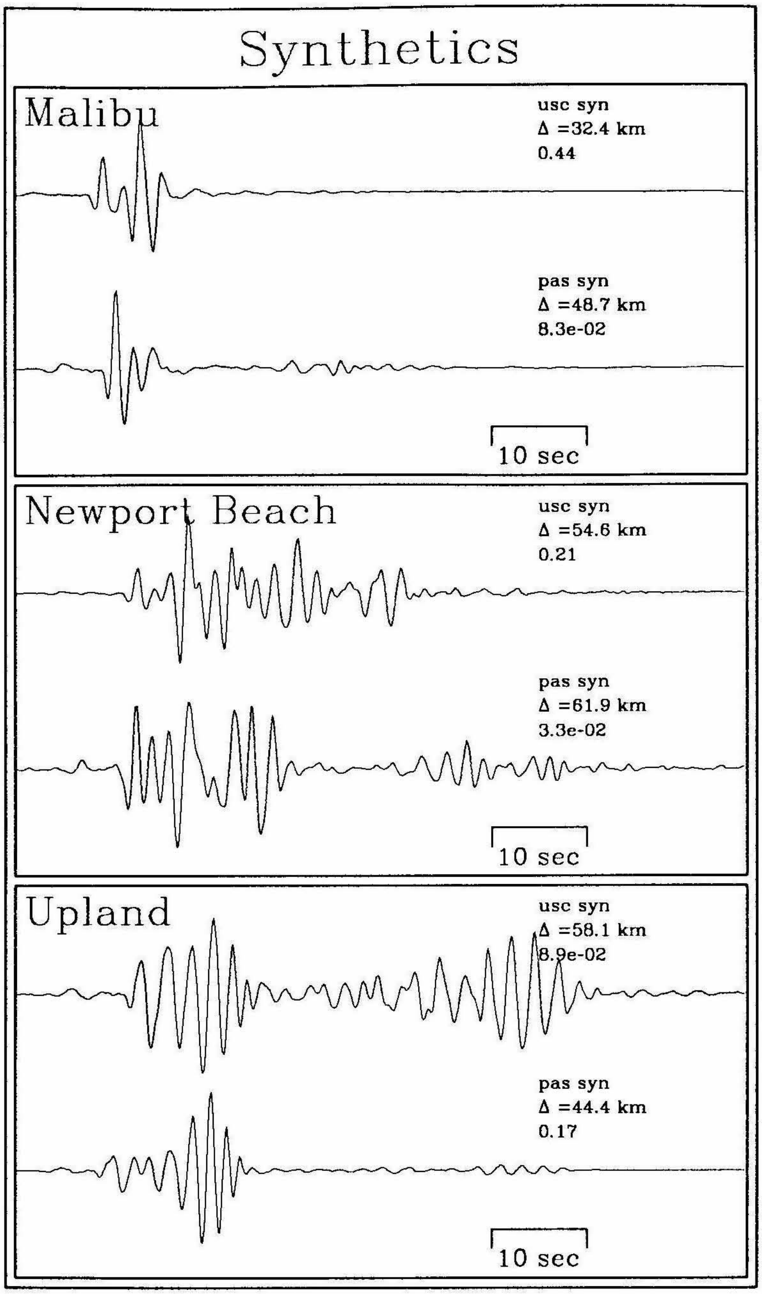

Figure 4.20. Complete synthetic waveforms obtained from the reciprocal source calculations for each of the three events. Traces are plotted relative to origin time for each event. Peak acoustic amplitude is listed above each trace.

Table 4.5. Comparison of peak amplitude ratios for data and synthetics.

earthquake	(USC/PAS) data	(USC/PAS) synthetics
Malibu	4.3	5.3
Newport Beach	4.0	6.4
Upland	0.68	0.52

acoustic formulation of the problem, the preliminary results presented here indicate the viability of the method to model these effects for realistic earth structures.

We have applied this technique to investigate the path effects for local earthquakes recorded at two southern California stations. The modeling results indicate that the presence of the large sediment filled basins in this region have a great impact on wave fields propagating through these structures. In particular, the low velocity material within the basins tends to channel and focus seismic energy, thus amplifying the strength of the waves observed in these areas. In addition, depending on the relative geometry of the source with respect to the basins, a complex pattern of shadow zones and bright spots is created in areas both inside and outside of the basins. These effects cannot be modeled with simple site response functions.

The results of the reciprocal source experiment are very encouraging. Using this technique allows us to model all possible source locations for a given observation site and within a given 3-D volume using only one simulation. This approach offers a powerful tool for use in the investigation of path effects for seismic wave propagation through heterogeneous 3-D structures. Eventually, we would like to couple this approach with a more accurate model of seismic wave propagation, such as the full elastic system. In doing this, we can then include effects due to realistic earthquake sources as well as address the problems associated with coupling between P and S energy.

One of the difficulties in performing this type of analysis deals with the parameterization of a realistic 3-D model to describe the region of interest. For the present study, we have used a relatively simple model to describe a region which contains some very complicated geologic structures. It would be useful to conduct a sensitivity study to investigate the impact that various changes to the current model would have on the nature of the modeling results. For example, one approach might be to develop a more appropriate model by applying small perturbations to the smooth ellipsoidal basins of the present model. Another approach could be to parameterize the basin outlines using a detailed map of the depth to basement rock. It may well be that the ellipsoidal basins used for the present model are too smooth to accurately represent the actual basin structures. This may over-accentuate the intensity of focusing and defocusing predicted from the model results (Figures 4.12 and 4.13).

Another area of concern which has not been addressed in detail in the present study is the incorporation of anelastic attenuation within the modeling process. This can be done with a simplistic model of attenuation (i.e., constant Q) and applied to the existing results or could involve more elaborate schemes which include a spatially variable Q operator into the numerical modeling technique. The effects of attenuation can be quite important, particularly in the low velocity layers within the basins where Q values can be rather small (see, for example, Duke et al., 1971). By neglecting these effects, our results may predict amplitudes which are too large for energy that has traveled predominately in the near surface layers within the basins. This may account for some of the mismatch in the peak amplitude ratios shown in Table 4.5. For example, in the modeling of the Newport Beach event, the record at USC is dominated by surface waves generated within the Los Angeles basin, while at PAS the surface waves are of comparable magnitude to the direct P-wave (Figure 4.20). Therefore, we would speculate that accounting for the effects of attenuation will have a greater impact on the USC results for this event than it will for the PAS results. The net effect would be to reduce the peak amplitude of the USC record by a greater amount than would be observed at PAS. This would bring the predicted peak amplitude ratio into better agreement with the observed value. A similar argument can be applied to the other events as well.

References

Abrahamson, N. A., and Litchiser, J. J., 1989, Attenuation of vertical peak acceleration: Bull. Seis. Soc. Am., **79**, 549-580.

Aki, K., and Richards, P. G., 1980, Quantitative seismology: W. H. Freeman and Co., San Francisco.

Bard, P.-Y., Campillo, M., Nicollin, F., and Sanchez-Sesma, F. J., 1988, A theoretical investigation of large and small scale amplification effects in the Mexico City valley: Earthquake Spectra, **4**, 609-634.

Berkhout, A. J., 1979, Steep dip finite-difference migration: Geophys. Prosp., **27**, 196-213.

Campbell, K. W., 1981, Near-source attenuation of peak horizontal acceleration: Bull. Seis. Soc. Am., **71**, 2039-2070.

Campillo, M., Gariel, J. C., Aki, K., and Sanchez-Sesma, F. J., 1989, Destructive strong ground motion in Mexico City: source, path, and site effects during the great 1985 Michoacan earthquake: Bull. Seis. Soc. Am., **79**, 1718-1735.

Claerbout, J. F., 1970, Coarse grid calculations of waves in inhomogeneous media with application to delineation of complicated seismic structure: Geophysics, **35**, 407-418.

Claerbout, J. F., 1985a, Imaging the earth's interior: Blackwell Scientific Publications.

Claerbout, J. F., 1985b, Fundamentals of geophysical data processing: Blackwell Scientific Publications.

Clayton, R. W., and Engquist, B., 1977, Absorbing boundary conditions for acoustic and elastic wave equations: Bull. Seis. Soc. Am., **67**, 1529-1540.

Clayton, R. W., and Engquist, B., 1980, Absorbing side boundary conditions for wave-equation migration: Geophysics, **45**, 895-904.

Clayton, R. W., 1981, Wavefield inversion methods for refraction and reflection data: Ph. D. thesis, Stanford University.

Davis, T. L., Namson, J., and Yerkes, R. F., 1989, A cross section of the Los Angeles area: seismically active fold and thrust belt, the 1987 Whittier Narrows earthquake, and earthquake hazard: J. Geophys. Res., **94**, 9644-9664.

Drake, L. A., and Mal, A. K., 1972, Love and Rayleigh waves in the San Fernando Valley: Bull. Seis. Soc. Am., **62**, 1673-1690.

Dreger, D. S., and Helmberger, D. V., 1990, Complex faulting deduced from broadband modeling of the February 28, 1990 Upland earthquake ($M_L = 5.5$): Bull. Seis. Soc. Am., *submitted.*

Duke, C. M., Johnson, J. A., Kharraz, Y., Campbell, K. W., and Malpiede, N. A., 1971, Subsurface site conditions and geology in the San Fernando earthquake area: UCLA-ENG-7206, School of Engineering, UCLA, Los Angeles, CA.

Flores, J., Novaro, O., and Seligman, T. H., 1987, Possible resonance effect in the distribution of earthquake damage in Mexico City: Nature, **326**, 783-785.

Fricke, J. R., 1988, Reverse-time migration in parallel: A tutorial: Geophysics, **53**, 1143-1150.

Hadley, D. M., and Combs, J., 1974, Microearthquake distribution and mechanisms of faulting in the Fontana-San Bernardino area of Southern California: Bull. Seis. Soc. Am., **64**, 1477-1499.

Hadley, D. M., and Kanamori, H. 1977, Seismic structure of the Transverse Ranges, California: Geol. Soc. Am. Bull., **88**, 1469-1478.

Hadley, D. M., Helmberger, D. V., and Orcutt, J. A., 1982, Peak acceleration scaling studies: Bull. Seis. Soc. Am., **72**, 959-979.

Hale, D., and Claerbout, J. F., 1983, Butterworth dip filters: Geophysics, **48**, 1033-1038.

Halpern, L., and Trefethen, L. N., 1988, Wide-angle one-way wave equations: J. Acoust. Soc. Am., **84**, 1397-1404.

Hauksson, E., 1990, Earthquakes, faulting, and stress in the Los Angeles Basin: J. Geophys. Res., **95**, 15365-15394.

Heaton, T. H., 1982, The 1971 San Fernando earthquake: a double event?: Bull. Seis. Soc. Am., **72**, 2037-2062.

Hill, J., Benz, H., and Schuster, G., 1990, Propagation and resonance of SH waves in the Salt Lake Valley, Utah: Bull. Seis. Soc. Am., **80**, 23-42.

Jennings, C. W., Strang, R. G., and Rogers, R. A., 1977, Geologic map of California, scale 1:750,000: Calif. Div. of Mines and Geol., Sacramento, CA.

Joyner, W. B., and Boore, D. M., 1981, Peak horizontal acceleration and velocity from strong motion records including records from the 1979 Imperial Valley, California earthquake: Bull. Seis. Soc. Am., **71**, 2011-2038.

Kagami, H., Okada, S., Shiono, K., Oner, M., Dravinski, M., and Mal, A. K., 1986, Observation of 1 to 5-second microtremors and their application to earthquake engineering. Part III. A two-dimensional study of the site effects in the San Fernando Valley: Bull. Seis. Soc. Am., **76**, 1801-1812.

Kanamori, H., and Satake, K., 1990, Broadband study of the 1989 Loma Prieta earthquake: Geophys. Res. Lett., **17**, 1179-1182.

Kelly, K. R., Ward, R. W., Treitel, S., and Alford, R. M., 1976, Synthetic seismograms - A finite-difference approach: Geophysics, **41**, 2-27.

Kennett, B. L. N., 1972, Seismic waves in laterally inhomogeneous media: Geophys. J. Roy. Astr. Soc., **27**, 301-325.

Kosloff, D. D., and Baysal, E., 1982, Forward modeling by a Fourier method: Geophysics, **47**, 1402-1412.

Kosloff, D. D., Reshef, M., and Loewenthal, D., 1984, Elastic wave calculation by the Fourier method: Bull. Seis. Soc. Am., **74**, 875-891.

Lee, M. W., and Suh, S. Y., 1985, Optimization of one-way wave equations: Geophysics, **50**, 1634-1637.

Liu, H. L., and Heaton, T. H., 1984, Array analysis of the ground velocities and accelerations from the 1971 San Fernando, California earthquake: Bull. Seis. Soc. Am., **74**, 1951-1968.

Ma, Z., 1981, Finite-difference migration with higher-order approximation: Presented at the Joint Technical Meeting, Beijing Comm. Geophys. Expl. CPS and Soc. Explor. Geophys.

Marfurt, K. J., 1984, Accuracy of finite-difference and finite-element modeling of the scalar and elastic wave-equations: Geophysics, **49**, 533-549.

Magistrale, H. W., 1990, I. The Superstition Hills, California, earthquakes of 24 November 1987 II. Three-dimensional velocity structure of Southern California: Ph. D. thesis, California Institute of Technology, Pasadena, CA.

Reshef, M., Kosloff, D., Edwards, M., and Hsiung, C., 1988a, Three-dimensional acoustic modeling by the Fourier method: Geophysics, **53**, 1175-1183.

Reshef, M., Kosloff, D., Edwards, M., and Hsiung, C., 1988b, Three-dimensional elastic modeling by the Fourier method: Geophysics, **53**, 1184-1193.

Sanchez-Sesma, F. J., Chavez-Perez, S., Suarez, M., Bravo, M. A., and Perez-Rocha, L. E., 1988, On the seismic response of the Valley of Mexico: Earthquake Spectra, **4**, 569-590.

Seale, S. H., and Archuleta, R. J., 1989, Site amplification and attenuation of strong ground motion: Bull. Seis. Soc. Am., **79**, 1673-1696.

Somerville, P., and Yoshimura, J., 1990, The influence of critical Moho reflections on strong ground motions recorded in San Francisco and Oakland during the 1989 Loma Prieta earthquake: Geophys. Res. Lett., **17**, 1203-1206.

Stead, R. J., 1989, Finite differences and a coupled analytic technique with application to explosions and earthquakes: Ph. D. thesis, California Institute of Technology, Pasadena, CA.

Vidale, J. E., and Clayton, R. W., 1986, A stable free-surface boundary condition for two-dimensional elastic finite-difference wave simulation: Geophysics, **51**, 2247-2249.

Vidale, J. E., and Helmberger, D. V., 1988, Elastic finite-difference modeling of the the 1971 San Fernando, California earthquake: Bull. Seis. Soc. Am., **78**, 122-141.

Vireux, J., 1986, *P-SV* wave propagation in heterogeneous media: Velocity-stress finite-difference method: Geophysics, **51**, 889-901.

Wapenaar, C. P. A., 1990, Representation of seismic sources in the one-way wave equations: Geophysics, **55**, 786-790.

Yerkes, R. F., McCulloh, T. H., Schoellhamer, J. E., and Vedder, J. G., 1965, Geology of the Los Angeles basin, California - an introduction: U.S. Geol. Surv. Prof. Paper 420-A, 1-57.

Zhang, G-Q., Zhang, S-L., Wang, Y-X., and Liu, C-Y., 1988, A new algorithm for finite-difference migration of steep dips: Geophysics, **53**, 167-175.

Appendix A

Wavenumber Domain Representation of the Extrapolation Equations

We begin with the split operator system as defined by equation (21)

$$(1-i\zeta)\big[1+\gamma_-(D_x^2+D_y^2)v+i\delta_-(D_x^2+D_y^2)\big]P_f^{n+1}$$

$$=(1+i\zeta)\big[1+\gamma_+(D_x^2+D_y^2)v+i\delta_+(D_x^2+D_y^2)\big]P_f^n. \qquad \text{(A.1)}$$

Assuming a homogeneous medium, we can Fourier transform this equation into the wavenumber domain to obtain

$$\hat{P}_f^{n+1}=\frac{(1+i\zeta)\big[1+(\gamma+i\delta)({K_x}^2+{K_y}^2)\big]}{(1-i\zeta)\big[1+(\gamma-i\delta)({K_x}^2+{K_y}^2)\big]}\hat{P}_f^n \qquad \text{(A.2)}$$

where $\gamma\pm i\delta=-(B\pm i\zeta A)/(1\pm i\zeta)$, $\hat{P}_f^n=\hat{P}_f(k_x,k_y,z=z_n,\omega)$ and we have the Fourier transform pairs

$$D_x^2=\frac{v^2}{\omega^2}\partial_{xx}\leftrightarrow-\frac{v^2}{\omega^2}k_x^2=-{K_x}^2$$

and

$$D_y^2=\frac{v^2}{\omega^2}\partial_{yy}\leftrightarrow-\frac{v^2}{\omega^2}k_y^2=-{K_y}^2.$$

Equation (A.2) is the wavenumber domain representation of the unsplit operator system. Now using the following approximation

$$
\begin{aligned}
&[1+(\gamma+i\delta)({K_x}^2+{K_y}^2)] \\
&\qquad\approx [1+(\gamma+i\delta)({K_x}^2+{K_y}^2)]+(\gamma+i\delta)^2{K_x}^2{K_y}^2 \qquad \text{(A.3)} \\
&\qquad= [1+(\gamma-i\delta){K_x}^2][1+(\gamma-i\delta){K_y}^2]
\end{aligned}
$$

we can derive the wavenumber domain representation of the split operator system from (A.2). This is given by

$$
\hat{P}_f^{n+1} = \frac{(1+i\zeta)[1+(\gamma+i\delta){K_x}^2][1+(\gamma+i\delta){K_y}^2]}{(1-i\zeta)[1+(\gamma-i\delta){K_x}^2][1+(\gamma-i\delta){K_y}^2]}\hat{P}_f^{n}. \qquad \text{(A.4)}
$$

Appendix B

Spatial Domain Implementation of the Phase Correction Filter

We begin with the phase correction operation defined in the wavenumber-frequency domain by

$$\hat{Q} = D_1\big[1 - i4\epsilon_0 D_2 \gamma\delta {K_x}^2 {K_y}^2\big]\hat{P} \qquad \begin{aligned} D_1 &= (1+\epsilon_1 K_x^4)^{-1}(1+\epsilon_1 K_y^4)^{-1} \\ D_2 &= (1+\epsilon_2 K_x^4)^{-1}(1+\epsilon_2 K_y^4)^{-1} \end{aligned} \tag{B.1}$$

where $\hat{P}(k_x, k_y, z, \omega)$ is the input wave field and $\hat{Q}(k_x, k_y, z, \omega)$ is the filtered output. Letting $\hat{P}' = -i4\epsilon_0\gamma\delta {K_x}^2 {K_y}^2 \hat{P}$ we can rewrite (B.1) as

$$\hat{Q} = D_1[\hat{P} + D_2\hat{P}'] \tag{B.2}$$

Now, the solution to this system can be built up by considering equations which have the following general form

$$\hat{Q}_{out} = D\hat{Q}_{in} \qquad \begin{aligned} D &= (1+\epsilon K_x^{2n})^{-1}(1+\epsilon K_y^{2n})^{-1} \\ n &= 1, 2, \cdots \end{aligned} \tag{B.3}$$

where $n = 2$ for the operators D_1 and D_2 in (B.2).

Following the method outlined by Hale and Claerbout (1983), we can write (B.3) as a cascade of second-order filters given by

$$\hat{Q}_{out} = \left(\prod_{j=0}^{n-1} \frac{\eta_j}{\eta_j - {K_x}^2} \prod_{k=0}^{n-1} \frac{\nu_k}{\nu_k - {K_y}^2} \right) \hat{Q}_{in} \tag{B.4}$$

where

$$\eta_j = \epsilon^{-1/n} \exp\left[i(2j+1)\frac{\pi}{n} \right]$$

and

$$\nu_k = \epsilon^{-1/n} \exp\left[i(2k+1)\frac{\pi}{n} \right].$$

Applying each term of the products in (B.4) in a recursive fashion we obtain the following sequence of second-order systems

$$\begin{aligned}
\hat{Q}_{\nu_0} &= \left[\frac{\nu_0}{\nu_0 - {K_y}^2} \right] \hat{Q}_{in} \\
\hat{Q}_{\nu_1} &= \left[\frac{\nu_1}{\nu_1 - {K_y}^2} \right] \hat{Q}_{\nu_0} \\
&\cdot \\
&\cdot \\
&\cdot \\
\hat{Q}_{\nu_{n-1}} &= \left[\frac{\nu_{n-1}}{\nu_{n-1} - {K_y}^2} \right] \hat{Q}_{\nu_{n-2}} \\
\hat{Q}_{\eta_0} &= \left[\frac{\eta_0}{\eta_0 - {K_x}^2} \right] \hat{Q}_{\nu_{n-1}} \\
\hat{Q}_{\eta_1} &= \left[\frac{\eta_1}{\eta_1 - {K_x}^2} \right] \hat{Q}_{\eta_0} \\
&\cdot \\
&\cdot \\
&\cdot \\
\hat{Q}_{out} &= \left[\frac{\eta_{n-1}}{\eta_{n-1} - {K_x}^2} \right] \hat{Q}_{\eta_{n-2}}.
\end{aligned} \tag{B.5}$$

Clearing the denominators and transforming each of these to the spatial domain we obtain the following series of equations

$$\begin{aligned}
[1+\nu_0^{-1}\frac{v^2}{\omega^2}\partial_{yy}]Q_{\nu_0} &= Q_{in}\\
[1+\nu_1^{-1}\frac{v^2}{\omega^2}\partial_{yy}]Q_{\nu_1} &= Q_{\nu_0}\\
&\cdot\\
&\cdot\\
&\cdot\\
[1+\nu_{n-1}^{-1}\frac{v^2}{\omega^2}\partial_{yy}]Q_{\nu_{n-1}} &= Q_{\nu_{n-2}}\\
[1+\eta_0^{-1}\frac{v^2}{\omega^2}\partial_{xx}]Q_{\eta_0} &= Q_{\nu_{n-1}}\\
[1+\eta_1^{-1}\frac{v^2}{\omega^2}\partial_{xx}]Q_{\eta_1} &= Q_{\eta_0}\\
&\cdot\\
&\cdot\\
&\cdot\\
[1+\eta_{n-1}^{-1}\frac{v^2}{\omega^2}\partial_{xx}]Q_{out} &= Q_{\eta_{n-2}}.
\end{aligned} \tag{B.6}$$

Upon discretization of the x- and y- axes these equations can be implemented as a sequence of tridiagonal matrix systems.

This sequence of equations can be written symbolically in the following manner

$$Q_{out} = \mathbf{D}Q_{in} \tag{B.7}$$

where $\mathbf{D}$ is the matrix operator which represents the operations performed in equations (B.7). Using this notation, the phase correction filter can then be represented in the spatial domain as

$$Q = \mathbf{D}_1[P + \mathbf{D}_2 P'] \tag{B.8}$$

where $P(x, y, z, \omega)$ is the input wave field, $P' = -i4\epsilon_0 \gamma \delta \frac{v^2}{\omega^2} \partial_{xx} \frac{v^2}{\omega^2} \partial_{yy} P$ and $Q(x, y, z, \omega)$ is the filtered output.

Appendix C

Derivation of a Pseudo Dispersion Relation from a Difference Equation

We begin with a difference equation of the form of equations (2.15a) and (2.15b), i.e.,

$$(D_x^2 - x_j)P^{k+1} = (D_x^2 - x_j^*)P^k \tag{C.1}$$

where $D_x^2 = \frac{v^2}{\omega^2}\partial_{xx}$, x_j is a constant, P^k is a known wave field and P^{k+1} is the field to be determined. Letting $x_j = \gamma_j + i\delta_j$, we can rewrite equation (C.1) as

$$(D_x^2 - \gamma_j - i\delta_j)P^{k+1} = (D_x^2 - \gamma_j + i\delta_j)P^k \tag{C.2}$$

or rearranging terms

$$(D_x^2 - \gamma_j)(P^{k+1} - P^k) = i\delta_j(P^{k+1} + P^k). \tag{C.3}$$

The differential equation corresponding to the difference equation (C.3) is given by

$$(\gamma_j - D_x^2)\partial_{\tau_j} P = -\frac{2i\delta_j}{\Delta\tau_j} P \tag{C.4}$$

where τ_j is a dummy variable which we have introduced to represent a pseudo-depth axis. Now we Fourier transform over the spatial variables, thus $\partial_x \rightarrow ik_x$ and $\partial_{\tau_j} \rightarrow ik_{\tau_j}$ to obtain

$$(\gamma_j + {K_x}^2)ik_{\tau_j}\hat{P} = -\frac{2i\delta_j}{\Delta\tau_j}\hat{P} \tag{C.5}$$

where $K_x = \dfrac{v}{\omega}k_x$ and $\hat{P} = \hat{P}(k_x, k_{\tau_j}, \omega)$. Factoring out $\hat{P}$ from equation (C.4) and solving for k_{τ_j}, we obtain

$$k_{\tau_j} = -\frac{2\delta_j}{\Delta\tau_j}(\gamma_j + {K_x}^2)^{-1}. \tag{C.6}$$

Equation (C.6) can now be thought of as a dispersion relation which governs the relationship between the variables k_x, k_{τ_j} and ω. This equation serves as the wavenumber-frequency domain representation of the operations performed in equation (C.1).

Appendix D

Incorporation of First-Order Scattering Terms within the Elastic Propagation Operator

In section 3.(scattering matrix), we presented elastic propagation operators appropriate for media with slight lateral heterogeneities [equations (3.24)]. The following discussion will show that these operators are accurate to first-order with respect to media variations as a function of x.

The general form of the elastic propagation operators from equations (3.24) is given by

$$\phi_p(x) = \left(\frac{\omega^2}{v^2} + \rho\, \partial_x \frac{1}{\rho} \partial_x \right)^{1/2} \tag{D.1}$$

where $v = v(x)$ is the appropriate media velocity (compressional or shear) and $\rho = \rho(x)$ is the density.

By parameterizing the media in the following manner

$$\rho(x) = \rho_0 + \delta\rho(x)$$

and

$$v(x) = v_0 + \delta v(x)$$

where we will assume that $|\rho_0| \gg |\delta\rho|$ and $|v_0| \gg |\delta v|$, we can write the following first-order approximations

$$\frac{1}{\rho(x)} \approx \frac{1}{\rho_0}\left(1 - \frac{\delta\rho}{\rho_0}\right) \tag{D.2a}$$

and

$$\frac{1}{v^2(x)} \approx \frac{1}{v_0^2}\left(1 - 2\frac{\delta v}{v_0}\right) . \tag{D.2b}$$

Using these expressions in equation (D.1), we obtain

$$\phi_p(x) \approx \left(\frac{\omega^2}{v_0^2}(1 - 2\frac{\delta v}{v_0}) + \partial_{xx} - \frac{\rho_x}{\rho_0}\partial_x \right)^{1/2} \tag{D.3}$$

where we have made use of the following identity

$$\frac{\partial}{\partial x}\delta\rho = \frac{\partial}{\partial x}\rho \equiv \rho_x .$$

Rewriting equation (D.3), we have

$$\phi_p(x) \approx \left(\phi_0^2 + \frac{\omega}{v_0} l \right)^{1/2} \tag{D.4}$$

where

$$\phi_0^2 = \frac{\omega^2}{v_0^2} + \partial_{xx}$$

is the homogeneous propagation operator and

$$l = -\frac{v_0}{\omega}\frac{\rho_x}{\rho_0}\partial_x - 2\frac{\omega}{v_0}\frac{\delta v}{v_0}$$

represents the first-order scattering contribution. Approximating equation (D.4) with a first-order Taylor series expansion, we get

$$\phi_p(x) \approx \phi_0 + \frac{1}{2\phi_0}\frac{\omega}{v_0}l. \tag{D.5}$$

Now using the plane wave approximation $\phi_0 \approx \dfrac{\omega}{v_0}$ for the scattering term in equation (D.5), this expression can be written as

$$\phi_p(x) \approx \phi_0 + \frac{1}{2}l. \tag{D.6}$$

Equation (D.6) represents the first-order approximation to equation (D.1) when the media varies weakly as a function of x.

Returning to equations (3.24), we note that the expression on the left hand side of each of these equations is of the same form as equation (D.6). Thus, we conclude that the heterogeneous propagation operators given by the expressions on the right hand side of each of the equations (3.24) are accurate to first-order with respect to media variations as a function of x.